Analysis of dissolution trapping mechanisms on CO_2 plume: Carbon Capture and storage.

Mathapelo Kholotsa

Student number: 2016328045

Submitted in the fulfillment of the requirements for the degree

Master of Science in Geohydrology

In the

Faculty of Natural and Agricultural Sciences

(Institute for Groundwater Studies)

At the

University of the Free State

Supervisor: Prof. Abdon Atangana

Bloemfontein, South Africa

November 2022

DECLARATION

I, Mathapelo Emely Kholotsa, hereby declare that the dissertation hereby submitted by me to the Institute for Groundwater Studies in the Faculty of Natural and Agricultural Sciences at the University of the Free State, in fulfillment of the degree of Master of Science, is my independent work. I have not previously submitted it to any other institution of higher education. In addition, I declare that all sources cited have been acknowledged using a list of references.

I furthermore cede the copyright of the dissertation and its contents in favor of the University of the Free State.

Furthermore, the following papers have also been submitted and are being evaluated:

- **Kholotsa, M. E. and Atangana, A., 2022. Modeling convective dissolution of Carbon dioxide and finger development with exponential decay and power laws**
- **Kholotsa, M. E. and Atangana, A., 2022. Modeling convective dissolution of Carbon dioxide and finger development with Mittag-Leffer law**

Mathapelo E. Kholotsa

November 2022

ACKNOWLEDGEMENTS

I want to begin by expressing my gratitude to the Almighty God for providing me with the means to attend the Institute for Groundwater Studies and for providing me with the necessary fortitude, wisdom, and guidance to complete this endeavor.

My Supervisor, Professor Abdon Atangana of the Institute for Groundwater Studies at the University of the Free State, deserves my thanks and utmost gratitude and appreciation. I want to take this opportunity to express all of these sentiments to him. This work would never have been completed if it were not for his invaluable contribution.

I would also like to thank the University of the Free State for seriously considering my application and providing me with the chance to earn my Master of Science degree from one of their faculties. I appreciate the Institute for Groundwater Studies investing in my professional development.

To my parents, Nthabiseng Ntloana and Tshidiso Ntloana, I appreciate the love, support, and encouragement you have shown me. To my sister Nkopelo Ntloana and my best friend, Tlhokomelo Isdora, thank you so much for being my cheerleader; your immense support carried me through this crucial period of my life, and I will forever be grateful for that.

ABSTRACT

The practice of carbon capture and storage effectively lowers greenhouse gas emissions and mitigates climate change and global warming. To determine whether long-term geological CO_2 sequestration is safe and practical, scientists have increasingly relied on model-based predictions of CO_2 behavior beneath the earth's surface in recent years. This investigation aims to get a firm grasp of the CO_2 dissolution trapping process and mathematical models depicting the behavior of the CO_2 convective dissolution process (Fingering) in saline aquifers. This comprehension will eventually help to ensure that the CO_2 plume stays inside the designated locations of CO_2 storage. The approach involved employing the concept of fractional differentiation by replacing the classical time derivative with the Caputo, Caputo Fabrizio, and Atangana Baleanu fractional derivative. To analyze the finger development process using three non-local operators: Power law, exponential law, and Mittag-Leffler function. Equally important, through performing linear stability analysis, we considered the stability evolution equation for the perturbation, which incorporated the exponential law and thus resulted in a memoryless function. We then replaced the exponential kernel with the Mittag-Leffler kernel to the perturbation equation to modify it into a process that has memory. By incorporating the Mittag-Leffler kernel into the perturbation equation, we suggest a new approach that provides a more accurate, robust, and efficient solution algorithm to capture finger development. In conclusion, we demonstrated some numerical simulations obtained using MATLAB.

Keywords: Carbon Capture Storage, Greenhouse gases, fractional differentiation, linear stability analysis

LIST OF NOTATIONS

α	*Alpha*
β	*Beta*
Δ	*Delta*
ε	*Epsilon*
γ	*Gamma*
Γ	*Gamma*
μ	*Mu*
∂	*Partial differential*
ϕ	*Phi*
φ	*Phi*
ψ	*Psi*
ρ	*Rho*
ξ	*Xi*
ζ	*Zeta*
η	*Eta*
τ	*Tau*
θ	*Theta*
Σ	*Sigma*
Λ	*Lambda*

ABBREVIATION'S TITTLE

CCS	*Carbon Capture Storage*
CO_2	*Carbon Dioxide*
GHG	*Green House Gases*
C	*Concentration*
S	*Saturation*
IPCC	*Intergovernmental Panel on Climate Change*
J	*dimensionless mass flux*
g	*gravity acceleration*
K	*Absolute permeability*
k_r	*relative permeability*
Ra	*Rayleigh number*
S_n	*Non-wetting phase saturation*
S_w	*Wetting phase saturation*
D_0	*Diffusion coefficient*
H	*The thickness of the saturated brine domain*
h_0	*The thickness of the capillary transition area*

Table of Contents

LIST OF FIGURES

CHAPTER 1: INTRODUCTION

This dissertation uses simulation and numerical approximation techniques to examine the CO_2 dissolution trapping mechanism involved in carbon capture and storage (CCS) operations. Furthermore, this chapter explains the rationale that prompted us to begin this study. It then outlines the goals and broad scope of the dissertation. In the last part of this chapter, there is a summary of each of the other chapters in this dissertation.

1.1Problem description

The progressive rise in global average temperature, termed "global warming" is widely documented and recognized by most scientists. Global warming is primarily due to human activities and their dependence on fossil fuels for energy generation. According to the IPCC (2014) report, Global CO_2 emissions are over 35 Gt/year.

CCS or carbon sequestration technologies can reduce Fossil fuel emissions. One carbon capture and storage method (CCS) injects CO_2 gas into depleted oil and gas reserves, often used in enhanced coal bed methane recovery. According to the CCS Global status report (2018), CCS must account for at least 14% of total emission reductions to attain the Paris climate aim of a 2°C temperature rise by 2060.

Though CCS projects have been implemented successfully, leakage from storage sites remains a source of worry (CCS global status report, 2018). To accurately estimate storage capability and associated dangers, it is required to have a firm grasp on the underlying physics and dynamics of the primary trapping mechanisms, to come up with the best-expected behavior of the system. This particular study looks at injecting CO_2 deep into saline aquifers. In this study, the dissolution trapping mechanism is essential to correctly evaluate the storage performance and its dangers.

However, modeling solute transport or water flow in a porous media can be challenging because faults and fractures operate as preferential channels for fluid flow. As a result of these channels, solutes are transported through the media more quickly (Beven & Germann, 1982; Starr *et al*., 1986).

These preferential channels can be categorized into three modes: funneled, macro-pore, and fingered. When layers or pieces of soil or rock have different hydraulic properties than the materials around them, funneled flow happens. In macro-pore flow, the solutes move through elongated and unevenly distributed pore spaces. Lastly, fingered flow is caused by conductive heterogeneities. Contrary to funneled flow, fingered flow is caused by heterogeneities in the moisture state, density gradients, and flux distribution within the medium rather than the heterogeneity in the medium itself which might be caused by the grain size distribution. Meaning, the media can be homogeneous, but fingered preferential flow can still occur (Nimmo, 2021).

Studies show that most of the research has been focused on the different dissolution regimes involved during convective dissolution, from the onset of instability, followed by the formation of CO_2-rich fingers, all the way to the shutdown regime where the dissolution slows as fingers encounter the bottom border and become hazy. However, it remains unclear why the CO_2-rich brine moves unevenly in a fingered preferential flow. Due to the non-local behavior exhibited by the convective fingers in terms of time and space, the resultant governing equation will need to be analyzed numerically using suitable numerical approximation schemes. The Caputo fractional derivative will be used in this dissertation to find solutions to include the long-range or long-tailed behavior depicted by fingering in the mathematical formulation. Caputo-Fabrizio and Atangana-Baleanu non-local fractional time operators will also have fading fingering behaviors or crossover.

1.2 Research aims and objectives

The primary aims of this investigation is to grasp the mechanism underlying the CO_2 dissolution trapping process in terms of finger development. To develop mathematical models depicting the process of fingering in saline aquifers. This comprehension will eventually help to ensure that the CO_2 plume stays inside the designated locations of CO_2 storage. Numerical analysis will be used to obtain the exact solutions to achieve this goal. The key objectives are as follows:

- To conduct an extensive literature review on the fingering process and factors affecting finger development during convective dissolution.

- Evaluate the plume evolution, from the start of finger development to the shutdown regime
- To analyze the finger development process using three non-local operators: Power law, exponential law, and Mittag-Leffler function
- To modify the stability evolution equation for the perturbations by incorporating the Mittag-Leffler kernel for the development of accurate, robust, and efficient solution algorithms

1.3 Research Framework

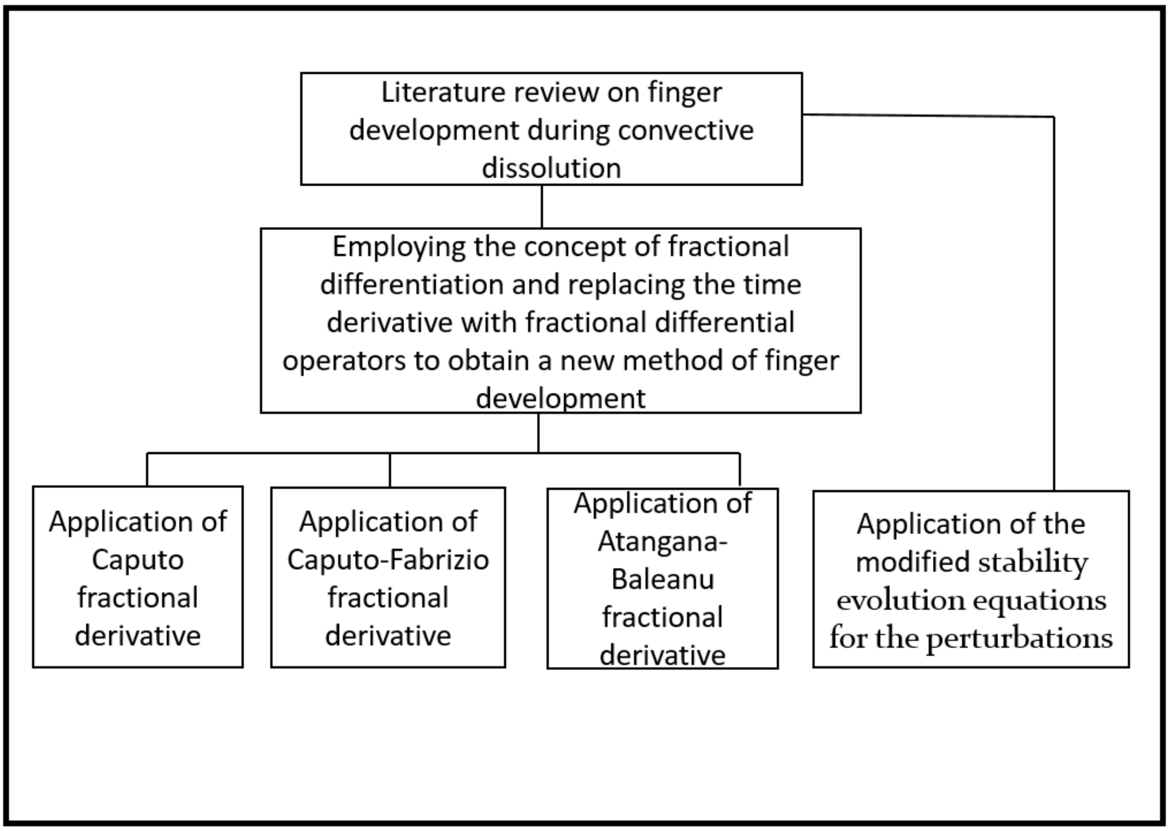

Figure 1 *Research framework*

1.4 Dissertation outline

Chapter 1 motivates the dissertation by outlining the research objectives and aims. ***Chapter 2*** gives some background information and logic on the impacts that CO_2 has on the environment, as well as how carbon capture and storage (CCS) plays an essential part in helping to reduce CO_2 emissions. This chapter also includes the various storage options for CCS, with particular emphasis on CO_2 storage in saline aquifers. Moreover, this chapter also provides an overview of different trapping mechanisms. Equally important, in this study, we talk about fractional differentiation because it will be used to model problems associated with groundwater flow. ***Chapter 3*** is devoted to a specific trapping mechanism, the dissolution trapping mechanism, as it forms the basis of this dissertation. First, this chapter will review the prior research on the trapping mechanism, the associated concepts, and the fingering process. Then, we explain the application of fractionation to solve the non-local behavior of the convective fingers.

Furthermore, in ***Chapter 4***, the Caputo, Caputo-Fabrizio, and Atangana-Baleanu fractional derivatives are used to solve the numerical problem of fingering transport in a porous medium during dissolution trapping. Moreover, linear stability analysis obtains a stability evolution equation for the perturbation. A new perturbation equation is introduced by replacing the exponential kernel with the Mittag-Leffler kernel with the perturbation equation. Lastly, ***Chapter 5*** concludes the study by summarising the findings and offering suggestions for further research.

CHAPTER 2: BACKGROUND AND LITERATURE REVIEW

This chapter presents some context on how increased CO_2 emissions affect the surrounding ecosystem. Discussion of geological carbon capture and storage as a potential resolution to lessen this effect will be outlined. This section will also describe the mechanism of sequestering carbon dioxide in deep salty aquifers. In addition, a review of various CO_2 trapping mechanisms and fractional differentiation operators will also be outlined.

2.1 Effects of CO_2 emissions on the environment

The world relies on fossil fuels for its growing energy demand. About 84% of energy consumption in the world comes from fossil-based fuels (Petroleum, 2020). The bulk of the climate change mitigation initiatives that 28 nations had announced by 2019, concerned switching to less energy-intensive energy sources. According to Secretariat (2020), the transition to renewable energy has gained global support. However, the transition to renewables is not smooth; socio-economical, technological, and political impediments hinder the transition (Ghosh *et al*., 2020). Climate change is a significant concern, especially amongst environmentalists and economists, as coal is the primary source of Carbon dioxide (CO_2) production. A snowball event of about 600-800 Mya resulted in a slow release of CO_2 gas (Crowley *et al*., 2001). The gas warmed up the climate and consequently trapped the heat and blocked outward radiation (Crowley *et al*., 2000). Despite the adverse effects of CO_2 in the atmosphere, it is also essential for photosynthesis process to take place.

Before industrialization and urbanization, CO_2 production was balanced with natural CO_2 intake processes such as photosynthesis (Shaw & Mukherjee, 2022). However, due to the industrial revolution after the 1780s, CO_2 production has since increased and continues to increase drastically. According to Harde (2017), it will take over a thousand years to remove the excess CO_2 in the atmosphere by solely natural processes.

Based on Bhui (2020), the current CO_2 levels in the atmosphere contribute to about 26% of global climate change. Additionally, it is anticipated that by 2030, the world's energy consumption will have doubled, with the bulk of that need still being satisfied by fossil fuels. Moreover, Lau *et al*. (2021) predicted a 2^0C increase in global mean temperatures by 2065. This prediction does not agree with the Intergovernmental Panel on Climate change (IPCC) objective of capping worldwide temperatures to 1.5^0C (Agreement, 2015). Reaching the set target by the IPCC means that the CO_2 emissions need to be reduced by 50-90% by the year 2050 (Agreement, 2015). China's current-day CO_2 emissions account for 26% of global emissions, while the United States of America, India, and Russia account for 13.7 %, 74 %, and 8%, respectively (Shaw & Mukherjee, 2022).

The dilemma of climate change is not a novelty in the world and remains one of the greatest threats faced by humankind. According to NASA (2020), Climate change is when temperatures and weather patterns change over a long period. The burning of fossil fuels and cement and chemical manufacturing industries that release greenhouse gases into the Earth's atmosphere causes these changes. Amongst all greenhouse gases, CO_2 is the primary greenhouse gas responsible for the current state of the climate (Regufe *et al*., 2021). The consequences of increasing atmospheric CO_2 levels have led to climate change, one of the biggest and most severe challenges to the environment and humanity.

This gas has contributed tremendously to trapping heat and blocking external radiation (Yoro & Sekoai, 2016). The most dominating of these gases is CO_2 which escalates the issue of climate change and global warming and poses an environmental threat (Regufe *et al*., 2021). Climate change causes sea level rise, melting of the polar ice, flooding, extreme weather conditions, deforestation, and damage to the ecosystem (Figueroa *et al*., 2008) The continued increase from present-day levels will inevitably lead to catastrophic outcomes in the not-too-distant future.

As the Word's population continues to rise, so is the fossil energy demand. Fossil energy production will, unfortunately, contribute to the ever-increasing CO_2 levels in the atmosphere. Figueroa *et al*. (2008) suggest three possible mitigation measures: switching to clean energies such as solar or wind, low-carbon alternatives, and carbon capture and storage (CCS) technologies.

India and South Africa continue to be highly dependent on coal for energy. The use of coal in these countries accounts for 53% and 60% of energy production, respectively

(Román, 2011). Moreover, both countries have the largest coal reserves in the world. Thus, CCS is a viable solution for both countries.

2.2Geological sequestration of carbon dioxide

The three components of carbon capture and storage (CCS) are capturing, transporting, and storing carbon dioxide see ***Figure 2***. The CCS process entails capturing CO_2 produced by industrial activities and transporting it to an appropriate storage facility, where most of it will be removed from the atmosphere (IPCC, 2005). This process is more viable in significant centralized sources such as power plants, energy industries, and factories producing iron, steel, cement, and bulk chemicals than in distributed emission sources.

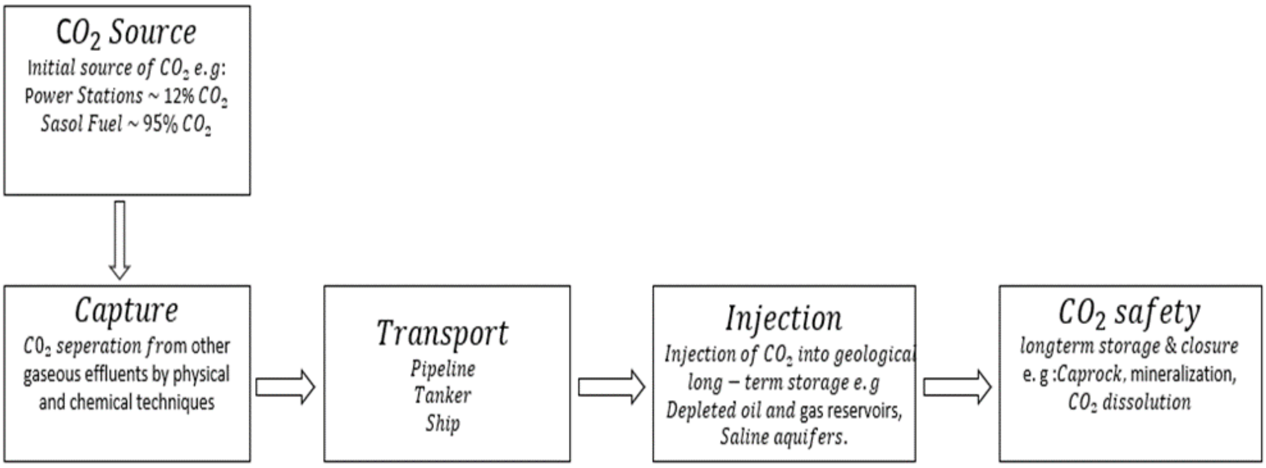

Figure 2 *Carbon capture and storage modified after Surridge (2004)*

2.2.1 Carbon Dioxide capture

CO_2 can be captured and separated from other gases in ammonium production and natural gas processes. The capturing of CO_2 depends on the type of combustion method utilized. There are three combustion technologies used to separate CO_2 from other gases and capture it ***Figure 3*** , namely:

•Oxy-fuel combustion: The hydrocarbon or fossil fuel is combusted within an oxygen-rich environment, with either pure oxygen or a mixture of oxygen and other noble gases (Yu *et al*., 2022). The resulting combustion causes the gas to be enriched in vapor and CO_2. The latter is then separated by reducing the temperature, so vapor condenses as water. Thus, there is no absolute carbon absorption, and the process requires no membranes, lowering the cost of the process for new plants. Also, the method enables almost 90% of CO_2 to be immediately pressed and sequestered without having to be cleaned first (Shaw &Mukherjee,2022)

•Pre-combustion capture: Involves the separation of hydrocarbon before any fuel combustion occurs. Hydrocarbons can be separated into hydrogen and CO_2 under extremely high temperatures (Shaw & Mukherjee, 2022).

•Post-combustion capture: the carbon is separated from the flue gas generated when fossil fuels are burned after the combustion of the fuel. This process is primarily used for industries and involves membrane separation and mineralization technologies. (Shaw & Mukherjee, 2022). It is a viable process for power generation plants, as these are significant contributors to CO_2 pollution in energy production. (Shaw & Mukherjee, 2022).

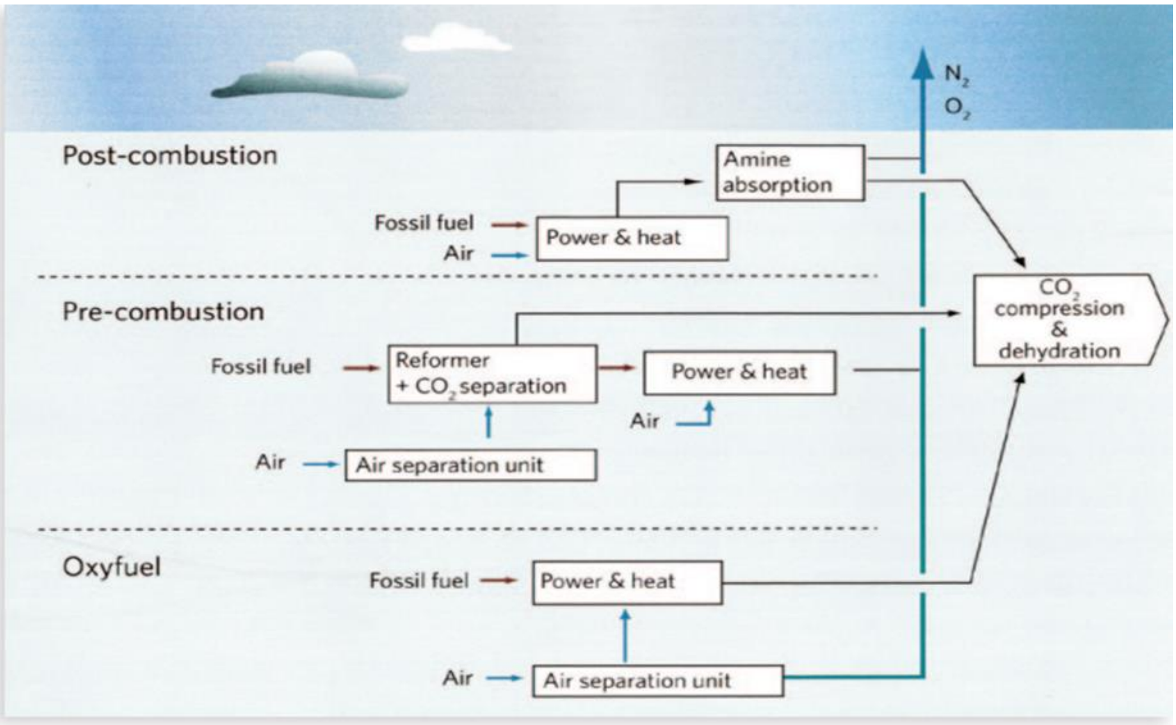

Figure 3 Three types of combustion techniques used for carbon capture (Freund & Kårstad, 2007)

2.2.2 Carbon Dioxide transport

After the carbon is captured and compressed, it is transported from the point source to a storage site. Firstly, the carbon is pressed together to turn into a liquid and move more quickly. (Shaw & Mukherjee, 2022). Once the carbon has been liquefied, transportation can commence through either road tankers, railways, ships, or pipelines. According to Shaw & Mukherjee (2022), pipeline transportation is the most convenient for volumes involved in CCS and has been in business since the 1970s.

This is because there is less friction along the pipeline per mass unit of CO_2 than when it is moved as a gas or as a two-phase mixture (liquid and gas). Along the pipeline's length, friction and heat transfer reduce pressure and temperature, respectively. (Skagestad *et al*., 2011). The CO_2 will stay in one phase while transitioning from supercritical fluid to liquid. CO_2 gas must be retained in a liquid-dense state at the end of the pipeline by maintaining a pressure above the critical pressure of 74 bar (Haugen *et al*., 2011). Because the gas is transported in a supercritical state and under high pressures, it is susceptible to contamination and gradient changes. Thus, to account for that, the transportation process can sometimes be costly (Shaw & Mukherjee, 2022).

2.2.3 Carbon storage

Carbon storage is the final stage of CCS. Once the CO_2 has been captured, it is transported and injected into storage sites at depths between 800-1000 m, where the supercritical CO_2 density is 600-800 kg/m^3 when compared to its density at atmospheric pressure, which is 2 kg/m^3 (Salinas, 2018). This process is called carbon sequestration (Shaw & Mukherjee, 2022). Carbon sequestration can be further categorized into biotic and abiotic sequestration depending on the process or method of CO_2 formation. Shaw & Mukherjee, 2022).

Biotic sequestration

Carbon dioxide capture occurs through abiotic media. Biological sequestration like this has been happening for years (Shaw & Mukherjee, 2022). The most well-known biotic carbon sequestration process is photosynthesis, where plants consume CO_2. The carbon capture through photosynthesis is termed phytoremediation (Shaw & Mukherjee, 2022). Photosynthesis can also occur in oceans because the oceans are fertilized with iron. Iron triggers the growth of phytoplankton, consequently increasing the rate of photosynthesis, which stimulates more CO_2 intake (Shaw & Mukherjee, 2022). However, with the current increased levels of CO_2 in the atmosphere, this type of sequestration proves to be inadequate, resulting in the continuous increase in the average global temperature now seen on Earth.

Abiotic sequestration

This type of sequestration occurs without any biotic mechanisms. It is more feasible than biotic sequestration as its efficiency can be improved by altering the rate and frequency of the process (Shaw & Mukherjee, 2022). Abiotic sequestration can be categorized into three types: mineral carbonation, Ocean injection, and geological sequestration.

- Mineral carbonation

Carbon is turned into stable carbonate minerals like Siderite ($FeCO_3$) and aragonite ($CaCO_3$) in the form of rocks by using the carbonation process (eq. 1) repeatedly on a large scale. (Shaw & Mukherjee, 2022)

$$CO_2 + MO \rightarrow Heat + MCO_3 \qquad [1]$$

Iron, calcium, and magnesium, are divalent metals(M). Following the chemical reaction in eq1 above, carbonate formation produces heat. (Olajire, 2013).

Mineral carbonation, as opposed to geological sequestration, is a feasible alternative since carbon is immobilized in stable carbonate rocks. It takes an inordinate amount of time to complete this, and the emission rates much outpace that (Shaw & Mukherjee, 2022). Equally important, this process can take place in deep saline aquifers (in situ) and on the surface (ex situ), where storage occurs in extensive continental basalts consisting of impermeable layers within interflow (Mukherjee *et al*., 2017).

- Ocean injection

Ocean sequestration is a viable alternative because its total sequestration capacity exceeds the world's total fossil fuel production of 5000 -1000 Gt (Herzog et al., 2001). The liquefied CO_2 is injected into the ocean water at depths equal to or greater than 1000 m for storage. However, aquatic life is subjected to overturning, which occurs between 300-1000 years. According to Shaw & Mukherjee, 2022, this means that about 20% of CO_2 is bound to leak into the atmosphere at some point. (Benson *et al*., 2008; Shaw & Mukherjee, 2022).

- Geological sequestration

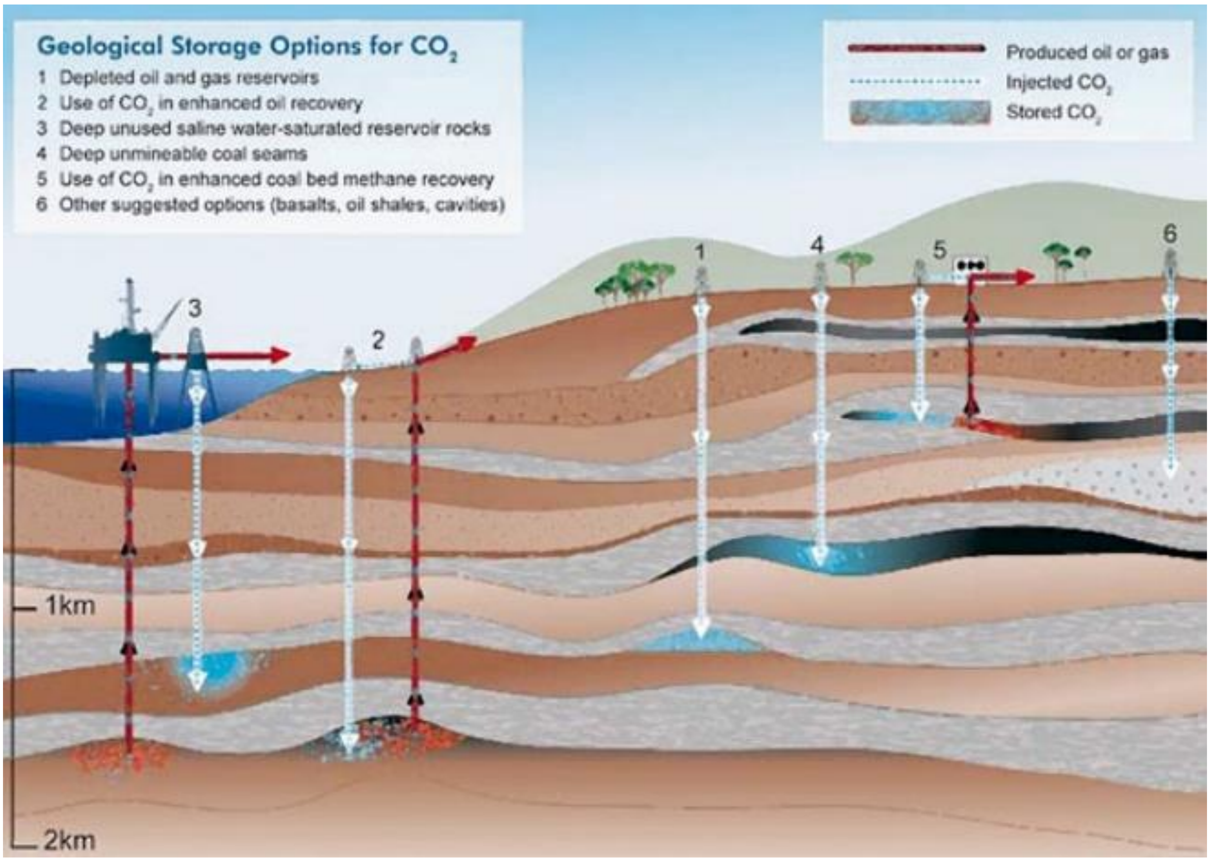

Figure 4 *Geological storage options for CO_2 (IPCC, 2007)*

Marchetti (1977) was the first to suggest geological storage of CO_2 as a counteractive measure to combat climate change. There were no published studies until the Norway government decided to reduce CO_2 production by introducing a carbon tax. In light of this, in 1989, Statoil began CO_2 storage tests (Kårstad, 1992). Because of a 1992 conference held in Amsterdam on the extraction of CO_2, geological storage alternatives received much attention and were extensively examined for the first time. These geological sites (***Figure 4***) include depleted oil and gas reservoirs (Ahmadi *et al*., 2016; van der Burgt et al., 1992), CO_2 used to enhance oil recovery as well as coal methane recovery (Bondor, 1992; Legg, 1992) ;) and saline aquifers (Kårstad, 1992).

Currently, the most economically feasible approach is to exploit already exhausted oil and gas reserves, which have already undergone extensive scientific investigation and exploration and possess the essential framework needed to extract hydrocarbons. (Jia *et al*., 2020). Two goals must be accomplished by injecting carbon dioxide into depleted oil and gas reserves. The first goal is for carbon sequestration, and the second goal is to maximize the amount of oil extracted from the reservoirs (Shaw & Mukherjee, 2022). According to Rubin (2006), the amount of CO_2 that can be stored in old oil and gas fields around the world is thought to be approximately 675 and 900 $GtCO_2$. Nonetheless, seismicity can be induced by injecting CO_2 in depleted oil and gas reservoirs, especially when working with fractured and faulted basins (Shaw & Mukherjee, 2022). The reservoirs need to be monitored frequently to avoid complications induced by seismicity.

The CO_2 can be injected into an oil well. Once there, it lowers the oil viscosity, enabling oil production (Şen & Babalı, 2007). Moreover, due to CO_2 being heavier than the resident brine, it can be used to relocate natural gas, consequently enhancing the productivity of the depleted gas fields (Şen & Babalı, 2007). Furthermore, increasing the amount of carbon stored in coal deposits may improve methane recovery. These coal deposits can accommodate approximately 300 to 200 $GtCO_2$ (Rubin, 2006). (Shaw & Mukherjee, 2022).

According to Mc Grail *et al*. (2006), the CO_2 can be retained in basaltic rocks, especially in areas such as the Indian subcontinent, where vast sedimentary basins are rare. Nevertheless, concerns remain regarding the possibility of leaking through fissures, which are typical in basalts.

The most potential large-scale geological storage solution in this current time is saline aquifer storage with a capacity of at least 1000 $GtCO_2$ and might be as high as 10000 $GtCO_2$ (Rubin,2006). As a result, this dissertation focuses on precise mathematical modeling of the complicated flow dynamics related to CO_2 storage in saline aquifers.

2.3 Saline aquifer CO_2 storage

Saline aquifers are underground sedimentary formations saturated with fluids and brine containing significant amounts of dissolved salts (Hesse, 2008). This brine cannot be utilized for irrigation or as a source of drinking water due to its excessive salinity (Hesse, 2008). Unmaintainable use of shallow groundwater resources, on the other hand, may result in the upward movement of subsurface brines and consequent degradation of water quality (Zhou et al., 2003).

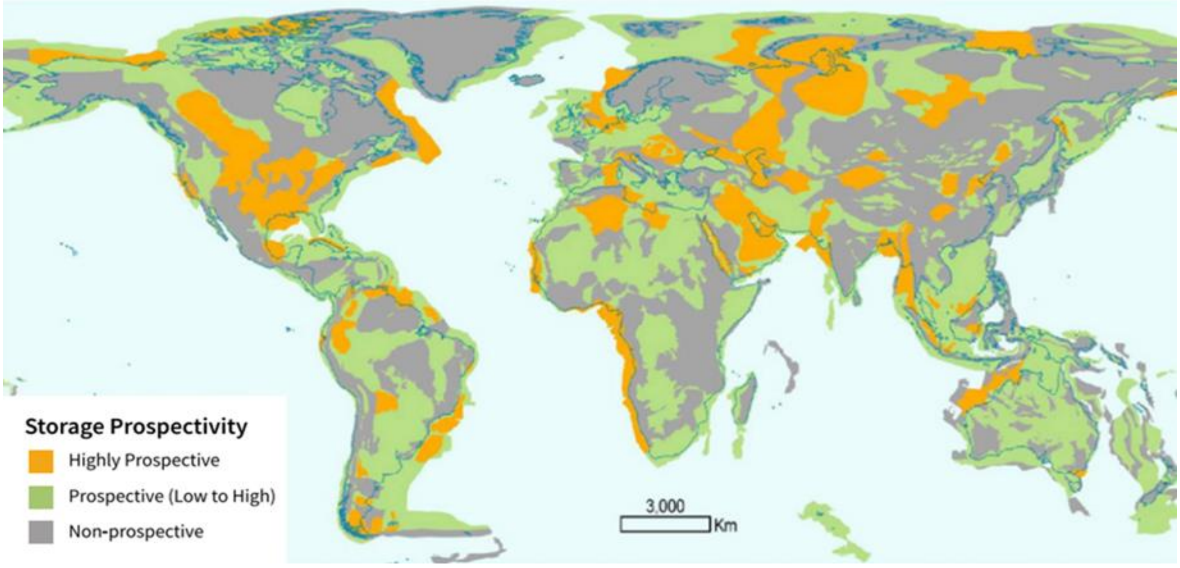

Figure 5 *Global sedimentary storage prospectively (Bradshaw et al., 2007).*

Saline aquifers are found in sedimentary basins worldwide and are not limited to coal, oil, or gas countryside (***Figure 5***)**.** Countries within the United Nations Economic Commission for Europe (UNECE), such as the Netherlands and the United Kingdom, have sedimentary basins with high carbon storage potential (Bradshaw *et al*.,2007). Moreover, North America, Western Europe, part of Australia, and North Africa show carbon storage prospects. Because geology knows no geopolitical boundaries, cooperation between the states involved is crucial to allow safe subsurface storage and sequestration of CO_2 (Bradshaw *et al*.,2007).

From the above ***Figure 5***, it can be seen that South Africa (SA) has a moderate CO_2 storage perspective. This implies that storage sites must be investigated thoroughly and significantly because SA depends on coal for energy production. Furthermore, this dependency on coal has led South Africa to be amongst the leading countries in CO_2 emissions in Africa, making it the 12thlargest producer of Carbon dioxide in the world (IPCC,2014). This shows that there is a growing need to get rid of CO_2 and potentially store it underground

Many nations, including Norway, Germany, the United States, Canada, Australia, the United Kingdom, Japan, Italy, Poland, and France, are considering CCS projects for saline aquifers (Rubin, 2006). The Statoil's Sleipner project in Norway is one excellent example of how CO_2 can be stored in a saline aquifer. This project began in October 1996 **(*Figure 6*)**and is intended to keep 20 million tons of CO_2 in the Utsira formation during its lifetime. (Torp & Gale, 2004). Seismic surveys have been used to track down the Sleipner CO_2 distribution in the subsurface, and thus far, the survey shows that the caprock restricts leakage of CO_2 out of the Utsira formation (Torp & Gale, 2004). ***Figure 6*** below shows worldwide CCS projects that have already started and commercial projects

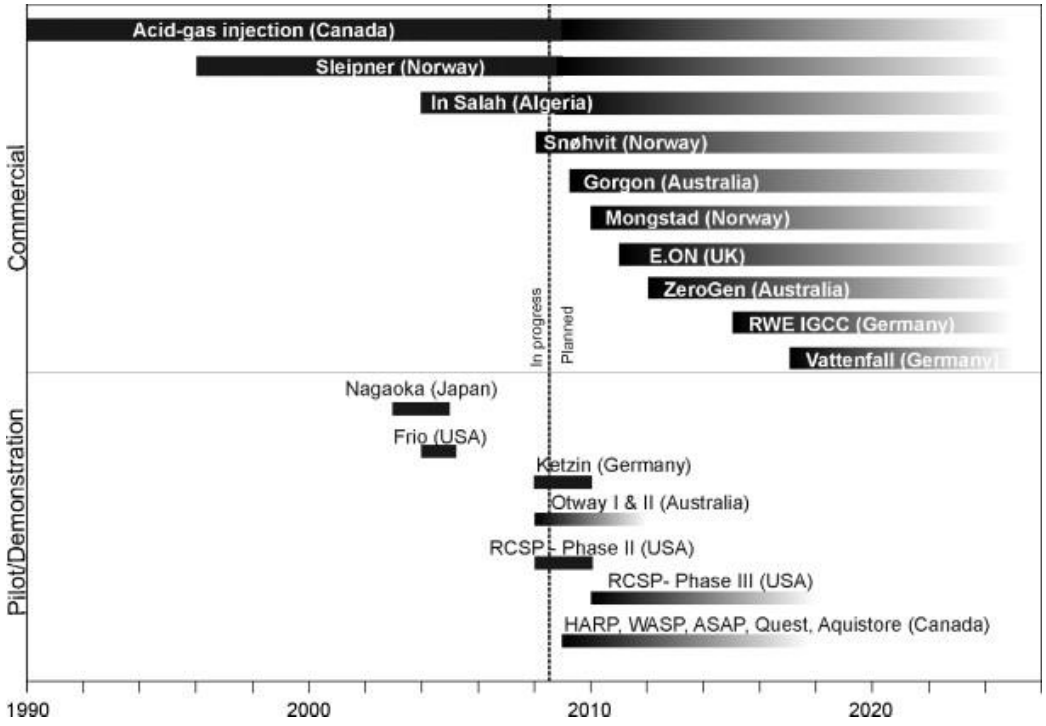

Figure 6 *Worldwide Carbon dioxide sequestration at pilot and commercial scale (Michael et al., 2010)*

2.4 Storage Safety

Despite the world's interest in carbon capture and the successful implementation of carbon capture and storage projects, there is an undying concern about the safety of the storage sites and the potential leakage of CO_2 to the atmosphere or groundwater resources. Ideally, a portion of the injected CO_2 will stay movable and buoyant for hundreds or perhaps thousands of years below the Earth's surface (Hesse, 2008). As a result, storage safety is heavily reliant on the strength of the caprock that prohibits the escape of the stored CO_2.

CO_2 stored in already exhausted oil and gas fields is unlikely to flow to the shallow surface because buoyant fluids have been preserved in oil and gas fields for long periods, and the seal has remained undamaged (Hesse, 2008). Saline aquifer storage, on the other hand, has no equivalent tests to check the reliability of the caprock. Thus, they are more susceptible to leakage into the shallow subsurface and back to the atmosphere (Hesse, 2008). Equally important, there are chemical and physical activities in the subsurface that boost storage safety by making CO_2 either negatively buoyant or immovable (Hesse, 2008)

According to Rubin (2006), over time, such a trapping mechanism progressively reduces the quantity of CO_2 accessible for leakage and, consequently, boosts storage safety. The injected CO_2 is shown to be moved between distinct physical and chemical states, as depicted in ***Figure 7*** below.

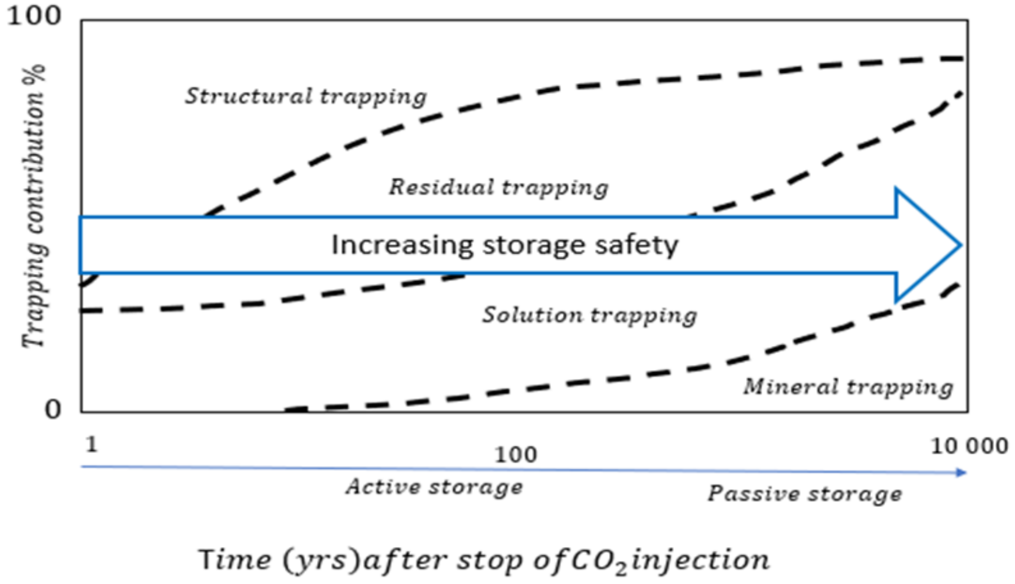

Figure 7 *shows various trapping mechanisms and associated periods (Trevor, 2015).*

The relationship between leakage and trapping mechanism affects the proportion of CO_2 that remains permanently in the subsurface (Hesse, 2008)

2.4.1Leakage possibilities.

Leakage in saline aquifers is a likely possibility and has received much attention over the years. Metz et al. (2005) outlined three leakage pathways: leakage via faults, fractures, cracks, and joints within a geological seal, and secondly through poorly constructed wells and abandoned pre-existing wells. Leakage can also occur through the low permeability rock systems in cases where the CO_2 entry pressure is surpassed.

2.4.2Trapping processes.

Because CO_2 is mobile and positively buoyant compared to brine, it can seep back into the atmosphere from the geological storage sites (Hesse, 2008). One of the objectives of this study is to analyze how trapping process affects the CO_2. A trapping mechanism is defined as a process that either immobilizes CO_2 or renders it negatively buoyant or both. Trapping processes in deep saline aquifers can occur in four different ways outlined below (Shaw & Mukherjee, 2022).

1. Structural trapping; at the top of the aquifer, CO_2 can be trapped as a plume and be stopped from moving upwards by structural cap rocks.
2. Residual trapping; CO_2 can be injected inside pore spaces of the aquifer rock and remain in the pore spaces. In this case, CO_2 is trapped by capillary forces in the pore spaces of the rock.
3. Solution trapping; CO_2 can dissolve inside the aquifer water. The resulting CO_2-rich water will become denser and sink to the aquifer's lowest part, where CO_2 will be trapped more effectively.
4. Mineralization trapping; CO_2-rich water can form carbonate minerals after reacting with the constituent rock minerals. CO_2 creates a weak carbonic acid when it dissolves in water. This weak acid can generate solid carbonate minerals when it reacts with the minerals in the surrounding rock. This process can take thousands of years depending on the constituent rock type. However, this mechanism is the most long-lasting and reliable trapping mechanism among all the others.

The processes, as mentioned earlier, are fundamental CO_2 sequestration processes; however, they require up to 10 000 years before they can happen (Tsang et al., 2017).

On geological timeframes, mineralization promises permanent storage, although dissolution and residual trapping (Hesse, 2008) trap CO_2 much sooner. As a result, the direct dissolving of the moving CO_2 plume and residual trapping is the principal trapping process, and residual CO_2 dissolution and dissolved CO_2 mineralization are secondary trapping processes (Hesse, 2008). **Figure 8** below depicts the link between various CO_2 trapping mechanisms.

Throughout the injection time, the CO_2 encounters brine water as it moves within the aquifer resulting in CO_2 dissolution (Kumar *et al.*, 2005). Towards the injection termination, as the CO_2 drifts towards the top of the aquifer, the residual trapping is likely to be particularly effective (Kumar *et al.*, 2005).

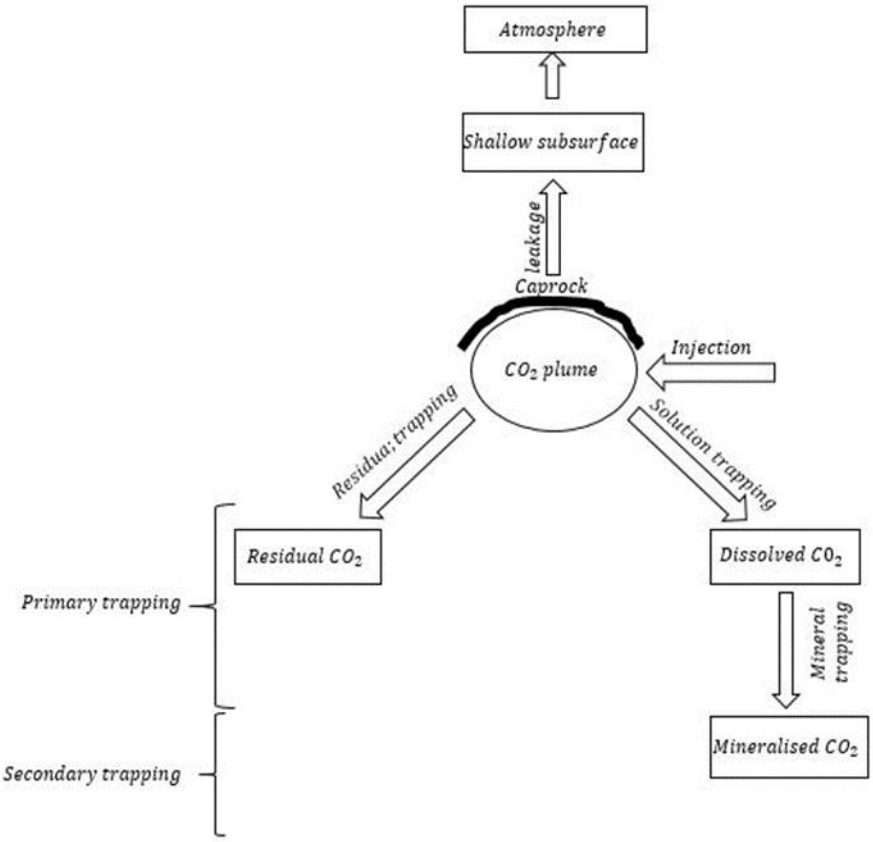

***Figure 8** shows a schematic diagram of the trapping mechanism, modified after Hesse (2008)*

2.5 Structural trapping

The success of CCS technology depends on keeping CO_2 locked underground, where it cannot get out back into the air or leak into other underground spaces important to particular ecosystems. One of the most important things to look for when choosing a place to store CO_2 is that the storage formation should be covered by an impermeable layer of rock that will keep CO_2 from leaking out until other ways to trap it are put in place. Such an impermeable layer of rock is called a structural or stratigraphic trap.

This section will overview structural and stratigraphic traps and their associated examples.

The term "trap" refers to a location where oil or gas can no longer travel further (Levorsen & Berry, 1967). Traps are formed when low-permeability cap rocks cover permeable reservoir rocks (carbonates, sandstones), impeding the upward flow of hydrocarbons. It is typical for cap rocks to include firmly compacted sandstones, compressed shales, and carbonate rocks. During structural trapping in CCS, the low permeability rock keeps the CO_2 intact. Due to carbon dioxide being less dense than the resident brine, it will migrate upwards to the point where it meets a seal rock with a capillary entry pressure higher than the force exerted by buoyancy (Zhang & Song, 2014). As a result, the CO_2 will build up and be trapped underneath the seal- rock. This seal rock could be either a structural seal rock or a stratigraphic seal rock. Chemical interactions between CO_2 and seal rock may cause fractures in cap rocks to either open or close. This can affect structural trapping. For any storage site, this mechanism is a requirement, and it is vital because it inhibits CO_2 leakage through the cap-rock while other trapping mechanisms are activated (Zhang & Song, 2014). There are two significant classifications of traps, structural and stratigraphic traps. These traps are characterized based on how the CO_2 accumulates

2.5.1 Structural traps

Structural traps are formed because of tectonic activity, such as faulting and folding of geological formations. These traps are the consequence of some structural deformation of rock, such as a bend or dip. It is common for this deformation to occur over millions of years after the sediment that forms the seals and rocks is deposited. Various sorts of deformation lead to multiple shapes and forms for these traps. Numerous structural traps can be used to store and keep CO_2 underground *(Donev et al., 2016)*. These structural traps consist of, but are not limited to: anticlinal folds, faults, and salt domes.

Anticlinal folds:

Anticlinal folds (***Figure 9***) are the most well-known structural traps formed because of the folding of the rocks. They are concave downwards and appear as overturned V-shaped zones on horizontal geological formations. In most cases, anticlines result from lateral pressure forces exerted on a horizontal stratigraphic formation. However, some others have been formed by the compression of accumulated sediments across topographical highs *(Donev et al., 2016)*. In such a trap, the CO_2 is trapped in the peak of the fold.

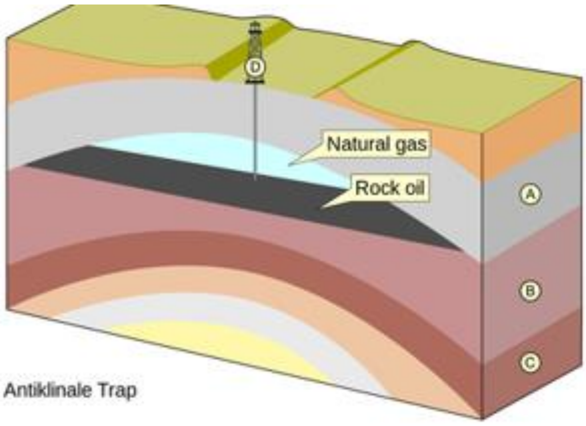

Figure 9 *Structural trap Anticlinal fold where A is an impermeable layer, B is a permeable reservoir rock, C is resident rock, and D is an oil borehole (Dunkle & Winniford, 2020).*

Fault traps

When the reservoir rock is faulted or fractured, fault traps are produced. Clay fills the space between the reservoir's two halves, preventing the gas from leaking. Fluid migration is impeded if a pressure difference occurs between the fault's two sides. While faulting is frequent in many oil and gas fields, traps that form solely because of faulting are rarer. Faulting often creates a new structure, the basis for setting the primary trap *(Donev et al., 2016)*.

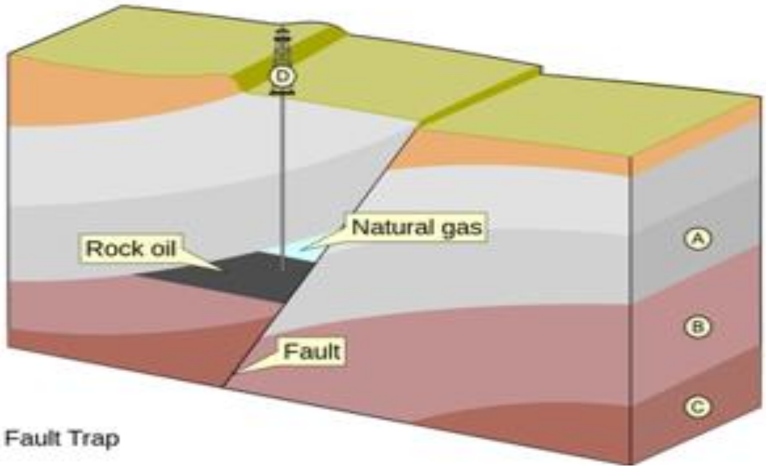

Figure 10 *Structural trap fault type where A is an impermeable layer, B is a permeable reservoir rock, C is resident rock, and D is an oil borehole (Dunkle & Winniford, 2020)*

2.5.1.3 Sault domes:

The salt dome formation traps (***Figure 11***) is caused by the upward migration of salt from beneath the surface of the Earth, and the salt migrates upwards because it is much lighter than the rock above it. This upward movement of the salt may distort and break apart rock as it moves up the mountainside. Salt tectonics is the name given to the process by which this salt deforms rock throughout millions of years. Flowing oil and gas will come to a halt at the salt dome, where it will be trapped *(Donev et al., 2016)*

.

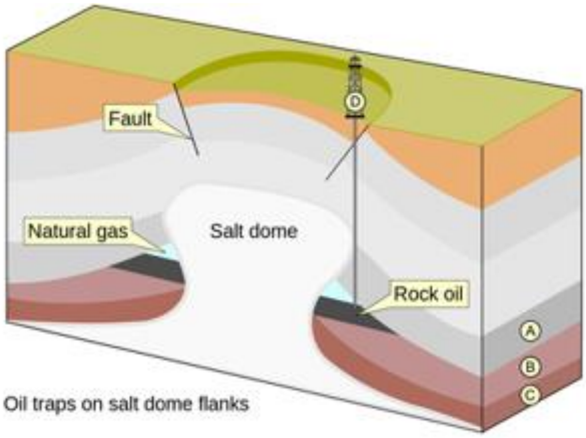

Figure 11 *A Structural trap salt domes where A is an impermeable layer, B is a permeable reservoir rock, C is resident rock, and D is an oil borehole (Dunkle & Winniford, 2020)*

2.5.2 Stratigraphic traps

These traps are formed because of the way sedimentary rocks are deposited. When the sediments that make up the reservoir rock are deposited discontinuously, barriers are created on both sides and the top of the reservoir. In some instances, shale that is impermeable or has low permeability may be used to form these barriers preventing the oil and gas from getting out of the reservoir, see ***Figure 12*** (Donev *et al*., 2016)

Regarding stratigraphic traps, two primary categories may be distinguished based on changes in the sedimentation process. Primary stratigraphic traps are formed because of changes that occur throughout the sedimentation process (Donev *et al*., 2016). These mainly structural alterations occur because of sediment deposition that is not continuous. Secondary stratigraphic traps are formed because of changes that happen after sedimentation has taken place. These modifications may include alterations in the rock's porosity, such as when limestone is altered into dolomite or when the rocks formerly positioned on the surface of the Earth deteriorate and disintegrate. Both of these alterations can lead to the creation of a cap-like rock (Donev *et al*., 2016)

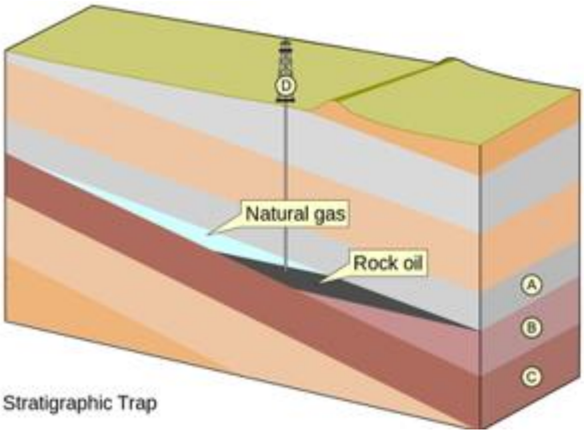

Figure 12 *Stratigraphic trap where A is an impermeable layer, B is permeable reservoir rock, C is resident rock, and D is an oil borehole (Dunkle & Winniford, 2020)*

2.6 Capillary/ Residual trapping

The Residual trapping mechanism reduces the volume of mobile CO_2 by trapping the gas into the void spaces of a storage aquifer in the form of isolated clusters enclosed by brine (Trevor *et al*., 2015). This mechanism comprises a variety of connected processes, such as capillary and trapping. Residual trapping because of the dependence of the system on its saturation history as well as relative permeability and capillary pressure hysteresis (Gershenzon *et al.,* 2014). Comprehending these processes is the key to understanding the trapping mechanism in a porous media. Basic hydrological processes such as buoyancy flow and capillary effects help to understand the dynamic spreading of the CO_2 plume post-injection (Gershenzon *et al.,* 2014)

2.6.1 Basic hydrological processes in a porous media

A porous media refers to a volume consisting of a solid matrix with linked spaces (pores) filled with liquid or gas phases (Pinder & Gray, 2008). Deep sedimentary porous media filled with brine is a common target for CO_2 sequestration. The pressure and temperature of the storage determine whether the injected CO_2 is in the form of a gas, a supercritical fluid, or a liquid. The injected CO_2 replaces the resident brine in a porous media through drainage. This results in phase interaction where the distinct phases compete for pore space (Joodaki, 2021). The volume percentage of each phase in the pores is called saturation. This parameter, together with phase interaction at the contact, determines how quickly the phase moves and where the injected and resident fluid go. Hydrological, chemical, thermal, and mechanical activities regulate how the two phases interact at the interface boundary. Large-scale processes like positive flow and small-scale processes like viscose fingering and capillary effects are hydrological processes that aid in spreading CO_2 (Joodaki, 2021).

Buoyant flow

During the injection, the CO_2 plume distribution is pressure-induced. Ending the injection, there is no longer any external force or pressure. The differential in density between the considerably less dense injected CO_2 and the much denser resident brine is now what regulates the flow of CO_2 and brine. Consequently, the density difference will result in the upward migration of the lighter CO_2 (positive buoyancy) and the downward migration of the heavier resident brine (negative buoyancy) (Joodaki, 2021).

Capillary pressure and capillary effects

An interface between the fluids is created in a system with two or more fluids that do not mix. In the case of a system with two phases, such as the CO_2 and brine phase system, it is difficult to define the pressure at the interface because of the varying pressure that each fluid carries on either side of the interface. Capillary pressure is the pressure differential between two phases at the contact (Joodaki, 2021). The capillary pressure in microscopic scales is defined by the Young-Laplace equation (Eq 2.6.1). It considers two factors: interfacial tension (σ) and contact angle(θ), with R representing the pore radius in which the CO_2-brine interface resides. For example, tiny pores in cap rocks may resist the capillary entrance of supercritical CO_2 migration in addition to their poor permeability since R has an inverse relationship with the capillary pressure (Tokunaga *et al*., 2013).

$$P_C = \frac{2\sigma cos\theta}{R} \qquad [2.1]$$

Between two different types of liquids, there is a force called "intermolecular force resulting in interfacial tension. Moreover, when two different types of phases come into contact, two different types of forces attract the molecules at their interface. There are two types of forces at work in the fluid namely the internal force and the adhesion force (Bear & Braester, 1972). The internal force maintains the cohesiveness of fluid molecules and creates a phase surface. The adhesion force is generated between the molecules of two distinct fluids at contact. Interfacial tension is the amount of work required per square inch to overcome the net attraction forces and make one phase bigger in space (Joodaki, 2021) (Bear& Braester,1972).

The forces of attraction between fluids and solids can be employed to describe wettability. There are distinct forces at work when two fluids meet a solid phase. The angle that the fluid makes with a solid phase refers to wettability. Less than 90°angle is a wetting phase, and greater than 90^0 angles are a non-wetting phase (Joodaki, 2021). Compared to a non-wetting fluid, the wetting fluid has a more significant surface attraction to the solid phase. Thus, wettability links the contact angle and the attraction forces. The difference in pressure between the wetting phase pressure(P_w) and non-wetting phase pressure(P_{nw}) is termed Capillary pressure (P_C) (Eq $[2.2]$) (Bear & Braester, 1972)

$$P_C = P_{nw} - P_w \qquad [2.2]$$

Non-wetting and wetting are the terms for the CO_2-rich phase and the brine fluid, respectively. As the CO_2 is injected into a brine-filled porous formation, it occupies most of the pore spaces leaving the wetting phase, which has a high affinity to the rock, to cover the solid phase with a fine coating (Joodaki, 2021). Ending the injection, there is no longer any external force or pressure. Thus, this makes it possible for the wetting phase to redistribute itself throughout the pores and cover the non-wetting phase. As the wetting phase passes through the pore, certain blobs of the non-wetting phase encircled by it break off because the throats of the porous medium have varying widths and diameters. The non-wetting phase that the plume leaves behind in these discrete, tiny patches is kept in place by capillary forces in the pores and is referred to as residually trapped gas (Joodaki, 2021)

Relative permeability

Darcy's law (eq 2.3) describes single-phase flow in porous media, where (u) is the flow velocity, $(k)$is the rock permeability, $(\mu)$is the viscosity, $\rho, and\ g$ is the density and gravity, respectively.

$$u = -\frac{k}{\mu}(\nabla P - \rho g) \quad [2.3]$$

In the above case, permeability is a parameter which explains how likely the formation will let the fluid pass through it. There will, however, be a lot more to say about the flow when there is more than one fluid in the medium (Joodaki, 2021). The complexity comes from the different speeds of the different phases and the fact that each phase has less space because of the other phase. Therefore, to characterize the flow, it is necessary to estimate the effective permeability of each phase (Abaci *et al*., 1992). The relative permeability of a multi-phase system is used to describe how the flow is going to be. It is defined as the phase effective permeability divided by the medium intrinsic permeability. Relative permeability defines how easy it is for a particular phase to pass through the porous medium (Abaci *et al*., 1992). In this way, the two-phase extension of Darcy's law can be written in the form of the following:

$$u = -\frac{k_{ri}k}{\mu_i}\rho_i(\nabla P_i - \rho_i g) \quad [2.4]$$

The relationship between saturation, relative permeability, and capillary pressure assumes that all pores within a porous media undergo the same magnitude of imbibition and drainage. However, in reality, the plume's tip and tail experience different processes (Joodaki, 2021).

2.6.2 Wetting phase displacement

During the drainage process (water replacement), the injected CO_2 displaces the resident brine as it moves into the pore space filling in the more considerable portion of the pore space, leaving the smaller and tighter parts of the pore space to the resident brine (*Figure 13*) (Trevor *et al*.,2015). This process results in gas saturation. The gas saturation can rise so high that only the thin wetting phase stuck to the rock is left in the pore. Because of capillary forces, the non-wetting phase becomes trapped in the pore as soon as imbibition begins. The trapping makes it difficult for the pore to return to its total saturation state. This trapped non-wetting phase is based on how much gas was already present in the pore and how much of the pore has been drained (Joodaki, 2021).

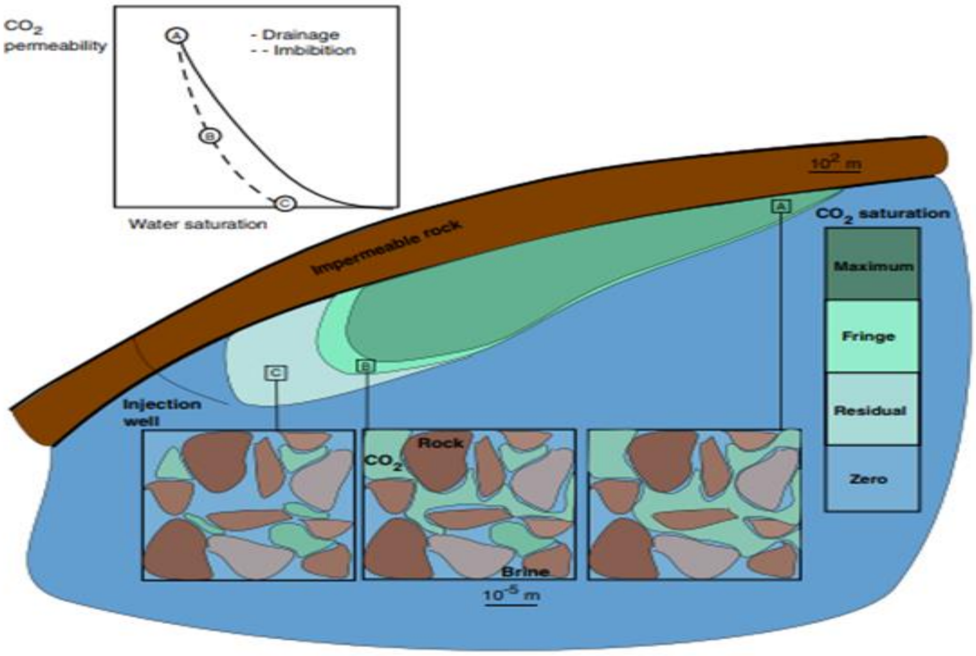

Figure 13 Is an illustration of residual trapping (Trevor et al., 2015)

2.6.3 Non-wetting phase replacement (Imbibition)

The imbibition process (gas replacement) depicted in ***Figure 14*** starts after irreducible liquid saturation is reached; this is after the injection period. The buoyant CO_2 migrates upwards, and the brine displaces the CO_2 at the tail of the plume (Iglauer *et al*., 2011). The most significant quantity of non-wetting phase that may be trapped in the pore is attained. However, the formation's pores are not fully emptied (Joodaki, 2021). As the liquid saturation drops, some pores start to suck. This is called "turning-point saturation," or. The system moves from drainage to imbibition (Joodaki, 2021). Imbibition leads to disconnected, essentially immobile bubbles of residual CO_2, which occur amid the migrating CO_2 plume (Iglauer et al., 2011). Residual trapping continues as long as the CO_2 migrates. The imbibition process includes other processes, such as snap-off and capillary pinning, depending on the nature of the heterogeneity of the storage reservoir (Valvatne et al., 2004).

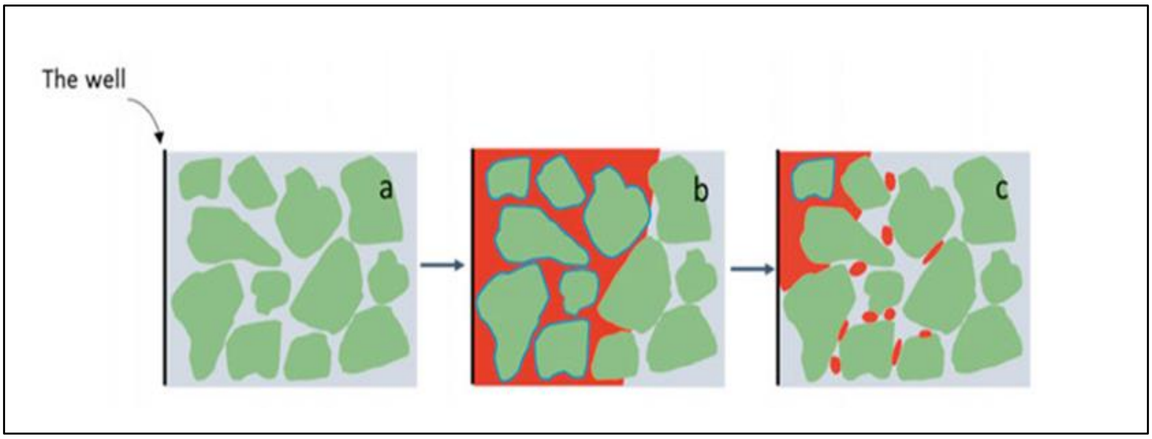

Figure 14 *shows the development of the CO_2 brine-filled porous medium that was injected at the beginning stage (fully saturated with brine), b depicts the replacement of water (drainage), and c represents the replacement of gas (imbibition) (Joodaki, 2021).*

Snap off

During imbibition, the brine behind the advancing CO_2 plume occupies the tiny pores and corner layers in a throat, which is the space between two adjoining pore spaces. As the brine fills up the tiny pores and pore throats, the pores and the throats become bigger and bigger. This causes the throat to fill up and the non-wetting phase (CO_2) to separate from the wetting phase (Brine) and be trapped as disconnected bubbles between the pores. The process is called snap-off, and it is depicted in ***Figure 15*** below (Gershenzon *et al*., 2017)

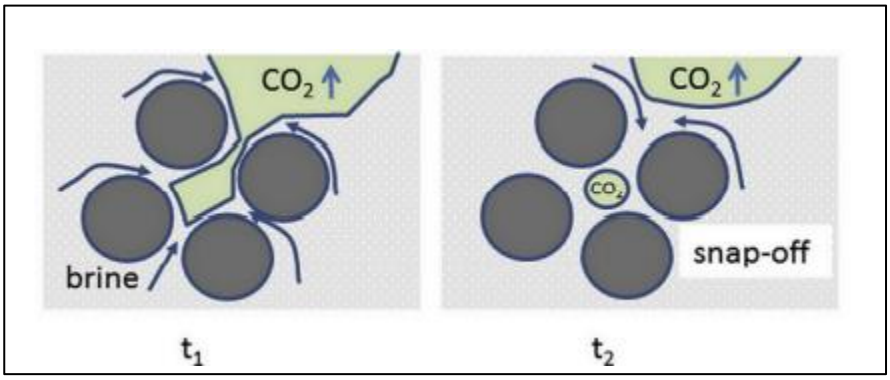

Figure 15 *is an Illustration of the snap-off process (Gershenzon et al., 2017)*

Capillary pinning

Capillary pinning in ***Figure 16*** occurs in heterogeneous storage reservoirs, and these reservoirs usually consist of coarse-grained and fine-grained sediments experiencing different capillary pressure. Capillary pinning is caused by the difference in capillary pressure between these sediments. As the CO_2 rises through rocks of different stratigraphy experiencing varying capillary pressure, it induces CO_2 pinning within coarse-grained sediments (Bryant *et al*., 2008; Gershenzon *et al*., 2014).

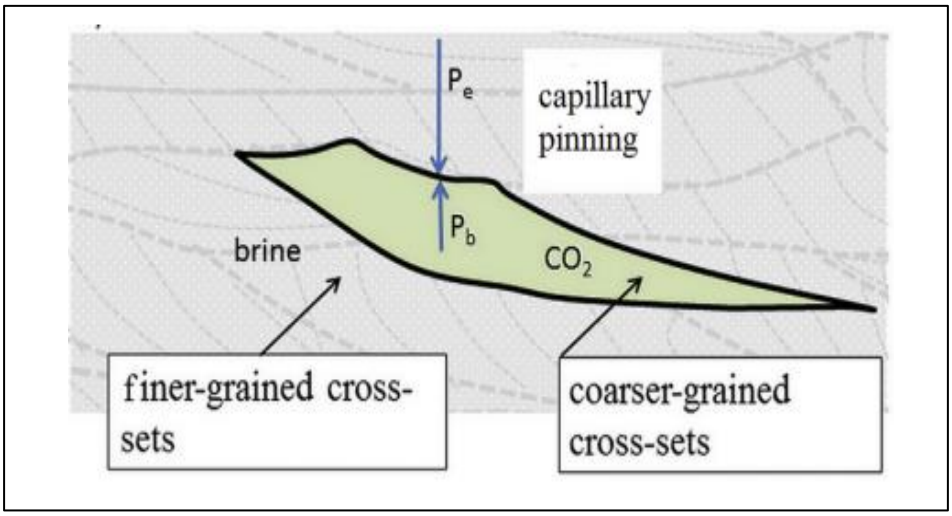

Figure 16 *an Illustration of capillary pinning (Gershenzon et al., 2017)*

The drainage and imbibition processes describe how carbon dioxide moves through storage aquifers. In rare situations, there may be recurrent patterns of drainage followed by periods of imbibition, which may induce CO_2 bubbles to re-flow (Ruprecht, 2014). In this case, fluid saturation does not just depend on how much is being drained or taken in at the moment. It also depends on what has happened in the past. This is called hysteric behavior. The hysteresis effect may lead to a significant amount of the non-wetting phase being trapped during imbibition, even if its relative permeability has been reduced. (Ruprecht, 2014)

Adding hysteresis to numerical models can fundamentally change the predicted CO_2 distribution. This is called "capillary/ residual trapping," which is thought to be another way that injected CO_2 gets trapped (Ruprecht, 2014). This trapping mechanism is essential because it determines how CO_2 spreads (Ruprecht, 2014). Non-hysteretic characteristic curves in numerical models may overestimate the total trapped CO_2 saturation in the CO_2 plume's trailing edge while underestimating the movement of the CO_2 plume's leading edge (Ruprecht, 2014).

The most widely known hysteresis models used to estimate the trapped CO_2 after imbibition as a function of pressure and relative permeability are Killough (1976), Carlson (1981), and Land's 1968 model. Another objective of this study will focus on

Land's model since almost every model for describing hysteresis has been based on his ideas.

3.6.1 Land (1968) model

Land came up with the concept of hysteresis by explaining what happens when the non-wetting phase gets trapped and how that affects the relative permeability. Land found that it initially invaded larger pores when CO_2 started to flow into the medium. When the CO_2 saturation level continues to rise, it begins to occupy smaller pores. During this procedure, the relative permeability of the non-wetting phase (kn) will continue to follow the principal drainage curve until the process reverses itself (Niasar *et al*., 2013).

When this occurs, the wetting phase enters the system by forcing the primary component of the gas phase to the front of the process and entrapping some of the non-wetting phases in the smaller pores. Because saturation mainly determines the behavior of the variables of interest, this trapped volume will impact how those variables behave.

Land discovered that the difference between the maximum non-wetting phase saturation (S_n^{max}) and the residual non-wetting phase saturation (S_{un}) is about constant for the system in question. Therefore, it is enough to measure one pair, like the extreme value, s, = 1, and the residual non-wetting phase saturation S_{un} is enough to figure out the relationship as shown in the equation below (Niasar *et al*., 2013).

$$S_{nr}(S_n^{max}) = \frac{S_n^{max}}{1 + (\frac{1}{S_{nr}} - 1)S_n^{max}} \qquad [2.5]$$

The actual process's residual saturation depends on both the residual saturation of its main loop and its maximal attainment. In addition, Land hypothesized that equation (2.5) would be true for any connected non-wetting saturation (S_n^c); hence, the disconnected non-wetting saturation, (S_n^d) would be equal to the difference between the two residual saturations,(S_{nr});(S_n^t), and(S_{nr});(S_n^c). This results in a direct formation of the following connection in terms of the non-wetting saturation Sn (Niasar et al., 2013):

2.7 Dissolution trapping

CO_2 can dissolve inside the aquifer water. The resulting CO_2-rich water will become denser and sink to the lowest part of the aquifer, where CO_2 will be trapped more effectively (Salinas, 2018).

2.8 Mineralization trapping

Some injected carbon dioxides react with the minerals in the host rock to generate solid carbonate minerals. This process is a subset of geologic sequestration and is known as mineral entrapment (Romanov *et al*., 2015). This is the final stage of CO_2 sequestration. Gunter et al. (1997) have shown that the mineralization trapping reactions are expected to take hundreds of years to complete depending on the chemical makeup of the host rock. Mineralization offers the hope for permanent storage on geological timescales, but CO_2 is effectively trapped by dissolution and residual trapping much earlier. This section will provide a review of mineralization trapping.

Mineral CO_2 sequestration can occur in two ways: the first route is direct, mineralization occurs through a single step. This route involves the carbonation of Ca /Mg silicates at increased temperature and pressure (Huijgen, 2007). Secondly, carbonate mineralization might occur as a result of the reactive chemicals being removed from the mineral matrix before being mineralized in a subsequent stage. (Huijgen, 2007).

Suitable elements for CO_2 sequestration

Alkali metals (e.g., Na, K) and alkali earth metals (e.g., Ca, Mg) hold the best prospects for carbonation. On the contrary, for long-term CO_2 sequestration, alkali metals are inappropriate because alkali bicarbonates dissolve excessively quickly. Equally important, of the alkali earth metals, calcium and magnesium are the most common and produce stable carbonate minerals; thus, they are the most suitable elements to carbonate for CO_2 sequestration purposes. (Huijgen, 2007).

Suitable minerals for CO_2 sequestration

Calcium and magnesium-rich minerals are the most suitable minerals for CO_2 sequestration. However, not all calcium and magnesium minerals provide the good alkalinity needed for the reaction of the acidic CO_2 (Huijgen, 2007). The needed alkalinity is usually derived from hydroxides and minerals such as pyroxenes and amphiboles (Huijgen, 2007). Carbonate minerals also provide a weaker source of alkalinity.

When it comes to Ca/Mg silicates, Mg-silicates are more advantageous because they are accessible in high purity and large amounts compared to Ca silicates. Ca-silicates, however, are more reactive toward carbonation than Mg-silicates (Lackner, 2002)

It is easier to convert carbonates into bicarbonates than silicates into carbonate minerals (Lackner, 2002). However, because bicarbonates are more soluble compared to Ca/Mg carbonates, they are deemed not suitable for mineral carbonation because if they encounter water, by any chance, they might dissolve (Huijgen, 2007).

Mineral carbonation in sedimentary reservoirs

- Silicate-rich saline formations

Most sedimentary saline aquifers consist of minerals such as quartz, usually making up to 90% of the constituent minerals. The remaining 10% comes from feldspars, clays, and carbonate cement (Romanov *et al.*, 2015). An example is the Mt. Simon sandstone in Canada, which has high-purity quartz-rich sandstone with a silica content of ~95% (Bowersox *et al*., 2013).

The most superficial carbonation reactions, for example, Ca and Mg minerals, are:

$$CaO + CO_2 \leftrightharpoons CaCO_3 \qquad [a]$$

$$MgO + CO_2 \leftrightharpoons CaCO_3 \qquad [b]$$

However, the direct reaction in the above reactions is rare because Ca and Mg do not occur in their purest form in nature. Instead, they appear as calcium and magnesium silicates. According to Romanov *et al*. (2015), mineralization within silicate-rich sandstone-hosted saline formations will most likely result from the dissolution of alkali feldspar ($NaAlSi_3O_8$) and the precipitation of dawsonite ($NaAlCO_3\ (OH)\ _2$). As an example, the theoretical reaction for the carbon mineralization of alkali Feldspar is shown below, together with the carbonation mineralization of wollastonite $(CaSiO_3)$ and olivine(SiO_4), respectively.

$$NaAlSi_3O_8(s) + CO_2\,(g) \leftrightharpoons NaAlCO_3(OH)_2(s) + 3SiO_2(s) \qquad [c]$$

$$CaSiO_3(s) + CO_2 \leftrightharpoons CaCO_3 + SiO_2 \qquad [d]$$

$$SiO_4(s) + 2CO_2 \leftrightharpoons 2MgCO_3 + SiO_2\,(s) \qquad [e]$$

The likelihood of mineral trapping in such host rocks will be low for sandstone formations with a lower concentration of silicate minerals. Consequently, the CO_2 stored in such formations will be a single-phase supercritical fluid or gas dissolved into the brine solution (Romanov *et al*., 2015).

- Calcite and dolomitic cemented sandstones

Calcite and dolomite cemented sandstone reacts differently from quarts-rich sandstones. The carbonate cement may dissolve near the injection site as injected CO_2 lowers the solution pH (Izgec et al., 2008). This dissolution may initially increase porosity, permeability, and injectivity near the injection site, followed by a decrease in all three as the dissolved carbonates re-precipitate further from the injection well (Izgec *et al*., 2008).

- Mafic or basalt-derived sandstone

The mineralogy of basaltic sandstones has a high fraction of alkali earth cations ($Ca^{2+.}$ Mg^{2+} and Ferrous Fe^{2+}). This makes them suitable candidates for mineral carbonation (Romanov *et al.,* 2015). However, a thorough investigation must be conducted to determine whether this formation has the appropriate storage depth and capacity to accommodate the carbon dioxide before it can be deemed a safe target for geological sequestration (Romanov *et al*., 2015).

- Greywacke sandstone

Greywacke is sand-sized, poorly sorted angular sand-sized grains of quartz, feldspars, amphiboles, and pyroxenes in a fine-grained clay matrix. The clay matrix makes up to 15% of the rock and tends to bind all the grains together, resulting in hard rock (Romanov et al., 2015). The greywacke composition makes it suitable for mineral trapping of the injected CO_2; however, the clay matrix reduces permeability and porosity thus, and the extent of storage in such formation is not well-characterized (Romanov et al., 2015).

- Ferric Iron sandstones

These sandstones consist of hematite (Fe_2O_3), and sediments made up of iron-rich micas, which can act as a source of ferrous Iron (Fe^{2+}) under reducing environments induced by the addition of partly oxidized sulfur (SO_2) to the CO_2 injecting stream. The reduction of ferric Iron (Fe^{3+}) to ferrous Iron (Fe^{2+}) during hematite dissolution can yield siderite ($FeCO_3$) (Romanov *et al*., 2015).

Carbonate reservoirs

Mineralization within carbonate-hosted saline formations is expected to occur because of the acidification of the brine by the injected CO_2 (Romanov *et al*., 2015). The acidified brine will dissolve the existing carbonates, thereby liberating Ca^{2+} and Mg^{2+} cations that will eventually recombine with the injected CO_2 to form carbonates and bicarbonates (White *et al*., 2011). The overall bicarbonate reaction is as follows:

$$H_2O + CO_{2(g)} + CaCO_{3(s)} \leftrightharpoons Ca\ (HCO_3)_{2(s)} \qquad [f]$$

The analysis of the reaction above, firstly, the CO_2 dissolves in water to form weak carbonic acid (H_2CO_3), dissociating to form HCO_3^- (eq 8) and CO_3^{2-} ions.

$$CO_2(aq) \leftrightharpoons CO_2(aq) \qquad [g]$$

$$CO_2(aq) + H_2O \leftrightharpoons H_2CO_3(aq) \qquad [h]$$

$$H_2CO_3(aq) \leftrightharpoons H^+(aq) + HCO_3{}^-(aq) \qquad [i]$$

$$HCO_3{}^-(aq) \leftrightharpoons H^+(aq) + CO_3{}^{2-}(aq) \qquad [j]$$

Carbonate species are then able to react with the divalent cations of Fe, Ca and Mg, forming siderite ($FeCO_3$), calcite or Aragonite ($CaCO_3$), magnesite ($MgCO_3$), as follows:

$$HCO_3{}^-(aq) + Fe^{2+} \leftrightharpoons FeCO_3 + H^+ \qquad [k]$$

$$HCO_3{}^-(aq) + Ca^{2+} \leftrightharpoons CaCO_3 + H^+ \qquad [l]$$

$$HCO_3{}^-(aq) + Mg^{2+} \leftrightharpoons MgCO_3 + H^+ \qquad [m]$$

The above carbonate minerals are the principal means by which CO_2 is sequestered (Gunter *et al*., 1997). The dissolving and re-precipitation of CO_2 can result in fluctuating porosity and permeability within the host rock (Kvamme et al., 2009). As a result, this changes the rock properties of the host rock (Kvamme et al., 2009)

Igneous-hosted saline formations

- Basalt

Basalt-hosted saline aquifers are made up of mafic minerals such as olivine (Mg, Fe_2SiO_4) and pyroxenes; enstatite ($MgSiO_3$), which have needed cations for mineral carbonation (Romanov *et al*., 2015). Thus, the formation can trap a significant amount of CO_2 in the form of stable carbonates (Romanov et al., 2015). Reactions are the same as carbonate-hosted saline aquifers as they both yield FeO_3 (Siderite), $MgCO_3$ (magnesite), and $CaCO_3$ (calcite or aragonite) (Romanov et al., 2015). Equally important, basalts constitute plagioclase feldspars minerals, Na-rich feldspars to Ca-rich feldspars. Each of these feldspars consists of cations needed to precipitate dawsonite or calcite (Romanov et al., 2015).

Unlike other trapping processes, the mineral trapping process offers permanent storage safety of CO_2 as the formed solid carbonate minerals are stable over a geological time scale and are also thermodynamically stable (Huijgen, 2007). Moreover, the carbonation reaction is exothermic, which releases energy utilized effectively (Huijgen, 2007).

2.9 Timelines of the trapping mechanisms

The timeframes corresponding with each of the sequestration processes are vastly different. Structural or stratigraphic trapping happens throughout the injection process and would serve as a precondition for the operation of other trapping mechanisms. The cap-rock integrity and high capillary pressure are the most critical aspects of the operation of this trapping mechanism. Residual trapping occurs during and after a brief period after injection and is triggered when the displacement occurs. CO_2 dissolves in brine during a short to mid-term period, resulting in solubility entrapment. CO_2 would be trapped by mineralization during the geological time (Zhang *et al*., 2014). The following are the timelines for each of the four trapping mechanisms:

$$t_{structural} < t_{residual} \ll t_{dissolution} \ll t_{mineralization}$$

When various trapping processes prevail in spatial distribution, the CO_2 plume's distribution varies over time. Structural trapping occurs when CO_2 builds beneath the seal and moves laterally. When the pore or pore throat of the flow route is very narrow, residual trapping may occur anywhere along the passage. At the CO_2 –brine interface, dissolution trapping may be detected throughout the flow route and under the cap rock. A cap rock mineral distribution varies, and so does mineral trapping. Both the calculation of storage capacity and the risk assessment depends heavily on the identification of dominant trapping mechanisms and the spreading of CO_2 plumes across time (Zhang *et al*., 2014)

2.10 Conclusion

In this chapter, a background on geologic carbon storage was provided. Carbon dioxide storage safety in the saline aquifer was explained since it outlines the purpose of the trapping mechanism required to minimize CO_2 leakage. Moreover, various trapping mechanisms and the ambiguity in predicting their evolution over time are explained. Equally important, an overview of the concepts of fractional differentiation and various fractional differentiation operators is outlined. Furthermore, previous work done using these operators is included to highlight their benefits and drawbacks in the last part of the fractional differentiation section.

CHAPTER 3: MODELLING OF CARBON DIOXIDE (CO_2) DISSOLUTION TRAPPING

3.1 Introduction

One of the main ways that CO_2 is trapped for long-term storage is by dissolving into the already existing brines. Since CO_2 does not move very quickly through the brine, convective dissolution, caused by a slight increase in brine density caused by CO_2 saturation, is the primary way dissolution traps happen. This chapter aims to understand the long-term breakdown of sequestered CO_2 by natural convective dissolution.

3.2 Overview and previous work on dissolution trapping

Dissolution trapping is permanent ,and happens during CO_2 storage. It slows down the movement of the plume and increases the storage capacity. This means that once CO_2 is dissolved in the brine formation, it can be stored safely (Lidenberg, 1997). Therefore, knowing about the physics of dissolution trapping and mass transfer between supercritical CO_2 and the resident brine is an essential part of the risk assessment for CO_2 storage.

Unfortunately, the supercritical CO_2 trapped by a structural closure is still mobile. As it spreads below the caprock, there is a chance of leakage through fractures and faults into shallow geological formations (Hamid, 2015). To reduce mobile CO_2 levels, alternative non-structural trapping mechanisms such as dissolution trapping occur. During dissolution trapping, the supercritical CO_2 dissolves into brine at the carbon brine contact, forming a diffusive boundary layer (Salinas, 2018; Spycher et al., 2003). This diffusive boundary layer is slightly denser than the resident pure brine depending on the brine's pressure, temperature, and salinity (Emami-Meybodi, 2015; Ennis-King & Paterson, 2003). The rate at which the dissolved CO_2 moves away from the carbon-brine contact determines the dissolution rate. The quick transportation of dissolved CO_2 away from the contact allows more fresh brine to encounter free-phase CO_2, consequently enabling more CO_2 to dissolve. (Emami-Meybodi, 2015).

The transportation of dissolved CO_2 is governed by advection, diffusion, and convection (***Figure 17***)**,** depending on how CO_2 is stored and the geological properties of the aquifer (Emami-Meybodi, 2015; Bakhshian, 2021). According to Garg et al.

(2017), advection refers to the bulk movement of solutes in the direction of groundwater flow. In the presence of pressure gradients, solute transport is dominated by advection and dispersion. The latter depends on velocity variation from the average flow velocity caused by geological heterogeneity in a porous media (Garg *et al*., 2017). The advective mass transport depends on the solute concentration in the aqueous phase, and the Darcy velocity of the aqueous phase is given by vector.

$$q = \frac{-k}{u} (\Delta P - \rho q) \qquad [3.1]$$

In Eq.3.1, k is the absolute permeability vector, u is the dynamic viscosity, P is the pressure, ρ is the density, and q is the vector of gravitational acceleration directed downwards.

In the presence of concentration gradients, solute transport is affected by molecular diffusion, meaning solutes move from a high-concentration area to a low-concentration area. The diffusive mass flux F_{diff} depends on the effective diffusivity and the concentration gradient (∇C), according to Fick's law, Eq. 3.2 (Domenico & Schwartz, 1997):

$$F_{diff} = D_e \nabla C \qquad [3.2]$$

Due to diffusion being a relatively slow transport process, a slight increase in the density of water occurring in the layer of water next to the free-phase CO_2 plume could cause gravitational instability. The gravitational instability will then trigger natural convection (Emami-Meybodi, 2015). During the convection process, gravity-driven currents move the CO_2-rich brine away from the CO_2-brine interface and downwards to the bottom of the aquifer, trapping the CO_2 more permanently (Emami-Meybodi,2015; Lindeberg & Wessel-Berg, 1997). The convection process could speed up CO_2 dissolution by bringing the CO_2-free phase into contact with more aquifer brine (Gilfillan *et al*., 2009). Weir et al. (1996) noted that the CO_2-rich brine moves down to the bottom of the aquifer due to the slight density increase induced by dissolution.

The dissolving of CO_2 will be sluggish at a border where both the supercritical CO_2 and the brine are at rest because, in such an instance, dissolution is governed by molecular diffusion of CO_2 in brine water (Hesse, 2008). Rapid dissolution, however, can be encountered across the CO_2 and fresh brine border owing to advection on either CO_2 or fresh brine water (Hesse, 2008). Moreover, convection motion in the brine and buoyancy of supercritical CO_2 can cause rapid dissolution.

In addition, when CO_2 is dissolved in brine, it can change the mineralogy of the aquifer. This happens because CO_2 reacts with host minerals within the aquifer over time resulting in mineral trapping, which was previously discussed in section 2.8. This can change the pH, chemical makeup, and brine concentration (Zerai *et al*., 2006).

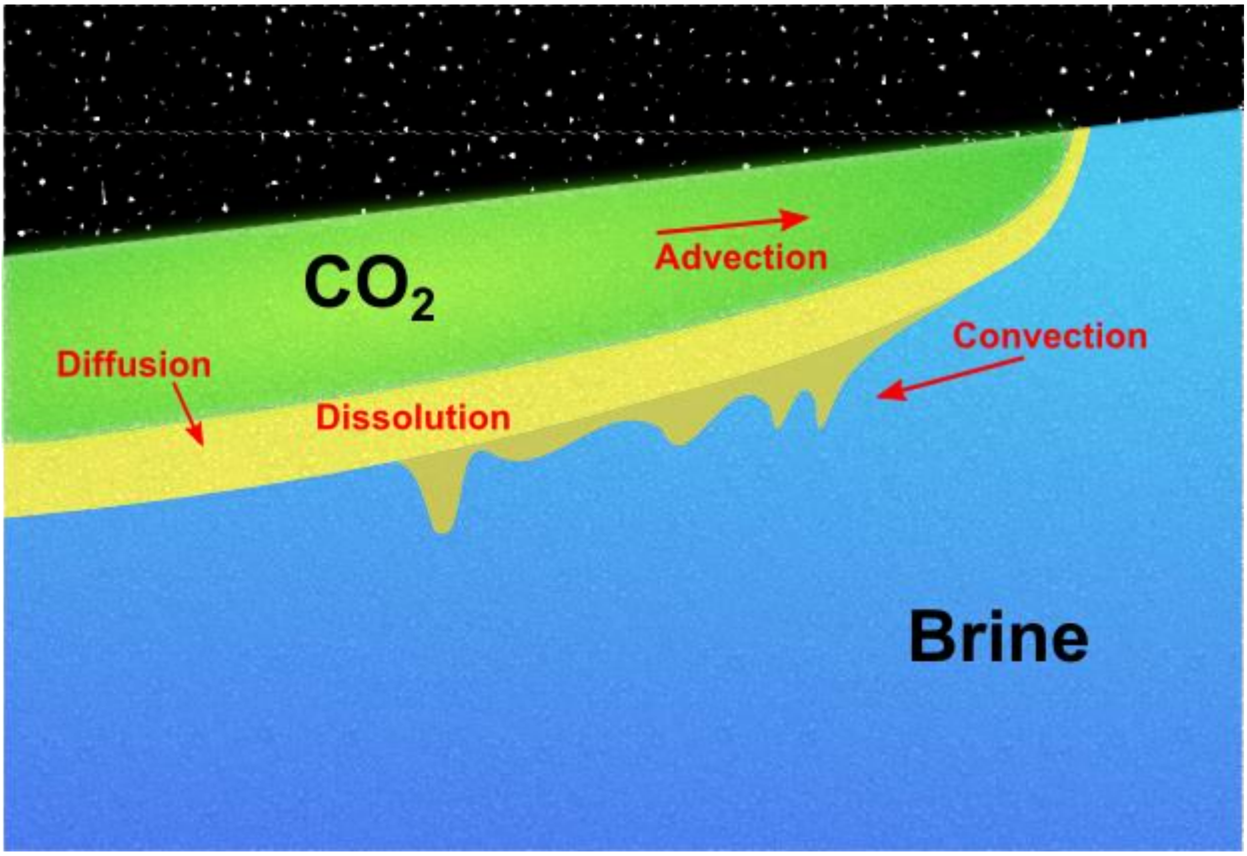

Figure 17 *A diagram illustrating different processes governing dissolution trapping (MRST, 2016).*

3.2.1 Convective dissolution process

According to Emami-Meybodi (2015), convection makes dissolution trapping more effective, which grows over time through events at different points in the dissolution process. These events in order are:

- Onset instability: the time when instability initiates due to the thickening of the diffusive boundary layer
- The onset of convection: where large structures look like fingers, the balance of the diffusive boundary layer changes, the flow increases, and the flow of

solutes starts to grow. The period at which the diffusive boundary layer first begins to distort is the onset of the event.

- Unsteady flux peak: the unsteady-flux peak is where long convective fingers interact with their neighbors. The convective fingers do not move much from side to side and overgrow until the maximum dissolution flux is reached. The flow quickly increases, reaches a maximum, and changes from pure diffusion to convection as the mass moves.
- The start of the constant-flux regime at a high Raleigh number: during the flux-growth regime, convective fingers grow, and the dissolution flux increases until reaching a maximum value. After the time of maximum flux, the convective fingers interact with their neighbors, and the freshly formed fingers produce dense CO2-rich plumes, which results in changes in dissolution flux. Where convective fingers combine and become coarser, the outcome is the formation of complex down-welling plumes, while the rate of dissolution flow remains the same.
- Convective shutdown. As convective fingers approach the bottom of the system, concentration differences diminish within the system, and convective cessation initiates. When the plumes affect the bottom border of the domain and saturation sets in everywhere, the system shifts into a convective shutdown regime, in which the density gradients become nearly uniform and the flux progressively changes.

3.2.2 Finger development

Mixing by convection has three steps: diffusion, convection, and shutdown (Jiang *et al.,* 2022). Most of the CO_2 that is injected dissolves into the brine by diffusion, and over time, a thin layer of solution forms at the boundary between the two phases. As more CO_2 is dissolved, the difference in density between the CO_2-rich brine and the resident brine gradually grows. As the difference in density gets big enough, the CO_2-rich brine will seep through the solution layer at the boundary between the two phases and form tiny fingers. The start of a convective stage occurs when a finger appears (Jiang *et al*., 2022)

During the first convection stage, many fingers form on the two-phase interface until the whole area is covered. Moreover, the finger grows in a downward direction, with the tip being spherical and thick, whereas the tail becomes tiny and thin, giving the finger a streamlined shape. As the finger grows, the small finger merges into the giant finger resulting in even larger convective fingers. Because the finger is going down, the pure saline moves up. This causes a new finger to form when it reaches the two-phase interface. At the end of the process, the finger hits the bottom of the cell, and the system enters a shutdown regime (Jiang *et al*., 2022).

3.2.3 Factors controlling convective dissolution

Various factors that control the convective dissolution processes include: (Emami-Meybodi, 2015);

- Anisotropy and heterogeneity: The gravitational instability becomes somewhat stabilized by the anisotropy, which occurs when the vertical permeability is lower than the horizontal permeability (as is frequently the case in natural reservoirs), delaying (or even delaying) the onset of density-driven solute convection and reducing the rate of dissolution.
- Geochemistry: Most of the time, geochemical reactions stabilize the system and simultaneously delay the start of convection. Fast-acting reactions lower the difference in density between the CO_2-rich fluid and the resident brine. This slows down convection and slows the rate at which CO_2 dissolves. Local mineralization can be balanced out, which may trap CO_2 faster than the reduction in dissolution; hence, overall sequestration can be more significant when considering geochemical factors.
- Advection and dispersion: The dissolving process may be aided by the advective flow of brine in some aquifers due to the strength of the background flow, which carries CO_2 further. The diffusion of CO_2 into the underlying resident brine initiates the dissolution process in these aquifers. Then the subsequent diffusion, dispersion, and advection processes carry the dissolved CO_2 throughout the aquifer. In the meantime, the CO_2 dissolved in the brine may make the brine somewhat denser, which would cause natural convection.
- Geothermal gradient: Aquifer systems experience density shifts because of the inherent vertical geothermal gradient. As a result, instability on the CO_2 layer may be induced, resulting in double-diffusive naturally occurring convection.
- Capillarity: Linea stability analysis conducted by Elenius *et al*. (2014) has shown that the capillary transition zone may speed up dissolution by up to four times and decrease the beginning time of instability by double

- Gravity currents: When there is a gravity current that moves laterally, Convective dissolution occurs. Convective dissolution and a moving CO_2 current could affect how long and buoyant CO_2 stays in the subsurface and how quickly it dissolves. Both experimental and theoretical studies by MacMinn et al. (2012) and Hidalgo et al. (2012), respectively, support the idea that the capillary transition zone indeed speeds up the dissolution rate.

According to Lidenberg (1997), the CO_2- brine mixture density is directly proportional to the CO_2 saturation, meaning, as CO_2 saturation increases, the CO_2- brine mixture density will also increase. The opposite is true. Due to the high density of the CO_2-rich brine, it will migrate downwards to the bottom of the aquifer. The accompanying drop in the system's overall volume permits the pressure in the aquifer to subside (Salinas, 2018). Therefore, leakage is unlikely to occur (Salinas, 2018).

The dissolution of CO_2 is dependent on various factors, namely, pressure, temperature, salinity, ionic strength, and injection depth (Salinas, 2018). The aqueous solubility of CO_2 decreases with increasing temperature but rapidly increases with increasing pressure. In addition, the salinity of the brine affects the solubility of CO_2; a higher salinity reduces solubility. The dissolving rate is also inversely related to ionic strength, meaning that higher dissolution rates occur at lower ionic strengths. A high dissolution rate is required to reduce the risk of CO_2 leakage. This means that convection is vital because if increased, the dissolution rate also increases, so the time to worry about leaks decreases. (Salinas, 2018)

3.3 Model setting

Unlike most studies on dissolution trapping mechanisms, such as studies by Lindeberg & Bergmo (2003), which assume a sharp contact between the supercritical CO_2 and water. In this study, we investigate the two-phase buoyancy-driven flow in the occurrence of the capillary transition zone (***Figure 18***) Since the dissolution rate is governed by convective mass transport in the brine, we use linear stability analysis to study the onset of convection to investigate the beginning of finger development, which permits a thorough depiction of the start of convection and, thus, finger development. A homogenous and isotropic medium is used to mimic the porous layer.

The underlying region is completely saturated with the wetting phase (sw = 1), while the gas cap is saturated with the non-wetting and residual wetting phase (sw = swr). The saturation of the wetting phase gradually decreases until it reaches a residual value in a transitional zone located above the wetting phase zone (swr).

To determine the function of the transition zone in the initiation of convection, researchers have focused on the region between the capillary transition zone and the wetting phase region. Because CO_2 dissolves in brine, a diffusive boundary layer forms, slightly increasing the density of the water in the layer adjacent to the buoyant free phase CO_2. The result is the onset of gravitational instability and free convection.

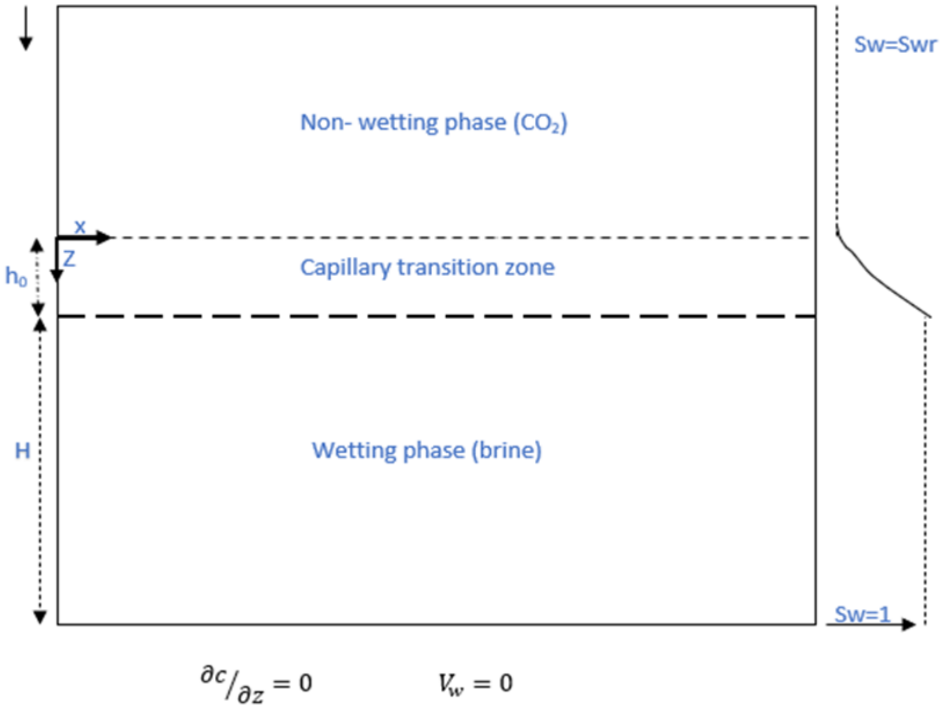

Figure 18 *Bottom wetting phase saturates the porous layer. A capillary transition zone, where the saturation of the wetting phase decreases toward residual saturation, lies above the saturated zone. The gas moving from the unsaturated zone into the wetting phase may cause a downward flow. Modified after (Hamid, 2015)*

3.3.1 Mathematical formations

For the considered two-phase system model, we adopt the dynamics of Boussinesq flow, which is given by the extension of Darcey's law. Since the mass transfer occurs in a closed system, the sink and source terms are ignored. The porous medium is two-dimensional, homogeneous, and isotropic. The (Aziz & Settari, 1979; Bear, 1988):

$$V_w = -\frac{Kk_{rw}}{\mu_w}(\nabla P_w - \rho_w g \nabla \mathrm{z}) \qquad [3.1]$$

$$V_n = -\frac{Kk_{rn}}{\mu_n}(\nabla P_n - \rho_n g \nabla \mathrm{z}) \qquad [3.2]$$

$$\emptyset \frac{\partial S_w}{\partial t} = -\nabla . V_w \qquad [3.3]$$

$$\emptyset \frac{\partial S_n}{\partial t} = -\nabla . V_n \qquad [3.4]$$

Equation 3.4.1 on 3.4.3 results in:

$$\emptyset \frac{\partial S_w}{\partial t} = \nabla . \left(\frac{Kk_{rw}}{\mu_w}(\nabla P_w - \rho_w g \nabla z) \right) \qquad [3.5]$$

[3.6]

Equation 3.4.2 on 3.4.4 results in:

$$\emptyset \frac{\partial S_n}{\partial t} = \nabla . \left(\frac{Kk_{rn}}{\mu_n}(\nabla P_n - \rho_n g \nabla z) \right)$$

$$V = V_w + V_n$$

[3.7]

$$\nabla . V = 0$$

[3.8]

$$P_{c=} P_n - P_w$$

[3.9]

$$S_w + S_n = 1$$

[3.10]

Where K represents the absolute permeability, kr represents the relative permeability, μ represents the viscosity, ρ represents the density, g represents the acceleration of gravity, $\emptyset$ represents the porosity, and $v = [u, v]$ represents the velocity vector. In this equation, u represents the horizontal component of velocity, and v represents the vertical component. S represents the saturation, defined as the typical volume fraction of a single phase in an elementary volume that is then normalized based on the volume's porosity. The mass source, denoted by Q, may represent an external source or the result of interphase mass transfer between fluid phases. The wetting phase, denoted by w, and the non-wetting phase, denoted by n, are indicated by the subscripts.

Marle (1982) defines a separate mass balance equation governing the dissolution and transport of CO2 dissolved in the brine (wetting) phase:

$$\frac{\partial}{\partial t}\emptyset(S_w C) + \nabla.(V_w C + J_w^{CO2}) = Q_w^{co2} \quad [3.11]$$

Here written in terms of mass concentration$C = \rho_w X_{CO2}$, with X_{CO2} denoting the mass fraction of dissolved CO2 in the brine phase. The diffusion term, modeled as Fickian, is as follows,

$$J_w^{CO2} = -\emptyset S_w \tau D \nabla C \quad [3.12]$$

Where τD is the product of the tortuosity and the diffusion coefficient for CO_2 in the brine phase, the term "source" refers to the rate at which mass is transferred from the CO2gas phase into the brine phase by dissolution.

The amount of dissolved carbon dioxide in the brine determines the density of the brine, which is denoted by:

$$\rho_w = \rho_{w,ref}\left(1 + \frac{\Delta\rho_w C}{\rho_{w.ref} C_{eq}}\right), C < C_{eq} \quad [3.13]$$

Where the density of the clean (non-carbonated) brine is$,\Delta\rho_w$ is the highest brine density level that can occur at the solubility limit, and $C_{eq}$is aqueous CO_2 concentration at the solubility limit.

By putting equations (3.3), (3.4), and (3.7) - (3.9) together, you can get the saturation equation for the wetting phase, which accounts for capillary and gravitational forces:

$$\nabla.\left(V_w\left(1 + \frac{k_{rn}}{k_{rw}}\frac{\mu_w}{\mu_n}\right) - \frac{kk_{rn}}{\mu_n}\left[\frac{dP_c}{dS_w}\nabla S_w + (\rho_w - \rho_n)g\,\nabla z\right]\right) = 0 \quad [3.14]$$

The two-phase convection-diffusion equation in eq 3.15 (yield & Bejan, 2006), Controls the dissolution of the diffusive species (C_d^w) into the wetting fluids (phase)

$$\emptyset\frac{\partial}{\partial t}(S_w C_d^w) = -\nabla.(V_w C_d^w) + D_0\emptyset\nabla.(S_w \nabla C_d^w) \quad [3.15]$$

Where D_0 is the effective diffusion coefficient. The wetting phase density,ρ_w is given as a linear function of concentration C_d^w

$$\rho_w = \rho_{w0}(1 + \beta C_d^w) \qquad [3.16]$$

Where $\beta = \frac{\partial \rho_w}{\rho_w \partial C_d^w}$ and it is considered constant, andρ_{w0} is the density of the wetting phase at $C_d^w = 0$. Using the stream function definition, the pressure can be removed. For the system at hand, by combining $\mu_w = \frac{\partial \psi}{\partial z}$ and $V_w = \frac{\partial \psi}{\partial x}$ with equations 3.3 and 3.13, the following equation is obtained:

$$\nabla^2 \psi = \frac{k k_{rw} g \rho_{w0} \beta}{\mu_w} \frac{\partial C_d^w}{\partial x} \qquad [3.17]$$

Where ψ is the stream function.

3.3.2 Fractional differentiation

The idea of fractional differentiation is becoming more helpful in groundwater science, especially when dealing with real-world phenomena such as convection and diffusion processes in complex systems. There are many fractional differential operators, but only a handful have been used in scientific studies to tackle real-world issues. The two fractional derivatives that are used most often are the Riemann-Liouville and Caputo derivatives. Atangana-Baleanu and the Caputo-Fabrizio derivatives are two new fractional operators introduced recently. These fractional operators are non-local, so they do not depend only on the input. Thus, they can be used for analyzing functions that are not only dependent on time. Traditional differential equations have a hard time modeling complex real-world systems. However, with fractional operators, the task is a lot easier.

Below is the explanation of each of the above-mentioned fractional derivatives:

The definition for the Riemann-Liouville derivative of fractional order α *of a function* (t) *is given as:*

$$ {}_0^{RL}D_t^{\alpha} f(t) = \frac{d^n}{dt^n} D^{-(n-\alpha)} f(t) = \frac{1}{\Gamma(n-\alpha)} \frac{d^n}{dt^n} \int_0^t (t-\tau)^{n-\alpha-1} f(\tau)\, d\tau \qquad [3.18]$$

The Riemann-Liouville fractional integral of order α for a function $(t) \in C1$ ([0, b], $\mathbb{R}n$): b>0 is given as:

$$ {}^{RL}_{0}I^{\alpha}_{t} f(t) = \frac{1}{\Gamma(\alpha)} \int_{0}^{t} (t-\tau)^{\alpha-1} f(\tau)\, d\tau, \qquad 0 < \alpha < \infty \tag{3.19}$$

Where $\Gamma\ (.)$ is the Euler's gamma function.

Definition for the Caputo fractional derivative:

Let $b\ >\ 0, \in\ H1\ (a,b)$ and$0 < \alpha\ > 1$, then the Caputo fractional derivative of a function of $f\ (t)$ of order $\alpha$is given as:

$$ {}^{C}_{0}D^{\alpha}_{t} f(t) = \frac{1}{\Gamma(1-\alpha)} \int_{0}^{t} (t-\tau)^{-\alpha} f'(\tau)\, d\tau \tag{3.20}$$

The definition of fractional Caputo-Fabrizio derivative:

Let $f\ \in\ H1\ (a,b)\ b > a, \alpha \in\ [0,1]$, then the definition of the Caputo-Fabrizio fractional derivative is given as follows:

$$ {}^{CF}_{0}D^{\alpha}_{t} f(t) = \frac{M(\alpha)}{1-\alpha} \int_{0}^{t} f'(\tau) \exp\left[-\alpha \frac{t-\tau}{1-\alpha}\right] d\tau \tag{3.21}$$

$$ {}^{CF}_{0}D^{\alpha}_{t} f(t) = \frac{\alpha M(\alpha)}{1-\alpha} \int_{0}^{t} \big(f(t) - f(\tau)\big)\, exp\left[-\alpha \frac{t-\tau}{1-\alpha}\right] d\tau \tag{3.22}$$

Nevertheless, if the function is not within H^1 (a, b), then the derivative is redefined as follows:

$$ {}^{CF}_{\ 0}D_t^{\alpha} f(t) = \frac{\alpha M(\alpha)}{1-\alpha}\int_0^t \big(f(t)-f(\tau)\big)\, exp\left[-\alpha\frac{t-\tau}{1-\alpha}\right] d\tau \qquad [3.22] $$

The following is the definition of the Atangana-Baleanu fractional derivative in the sense of Riemann-Liouville:

Let $f \in H^1\ (a,b)\ b > a, \alpha \in [0,1]$

$$ {}^{ABR}_{\ \ a}D_t^{\alpha} f(t) = \frac{B(\alpha)}{1-\alpha}\frac{d}{dt}\int_a^t f(\tau)E_\alpha\left[-\alpha\frac{(t-\tau)^\alpha}{1-\alpha}\right]d\tau; \quad 0<\alpha<1 \qquad [3.23] $$

The following is the definition of the Atangana-Baleanu fractional derivative in the sense of Caputo:

Let $f \in H^1$ (a, b)), $b>a$, $\alpha \in [0, 1]$

$$ {}^{ABR}_{\ \ a}D_t^{\alpha} f(t) = \frac{B(\alpha)}{1-\alpha}\int_a^t f'\,(\tau)E_\alpha\left[-\alpha\frac{(t-\tau)^\alpha}{1-\alpha}\right]d\tau; \quad 0<\alpha<1 \qquad [3.24] $$

The Atangana-Baleanu fractional integral of order α of a function f (t) is given as:

$$ {}^{AB}_{\ a}I_t^{\alpha}\big(f(t)\big) = \frac{1-\alpha}{B(\alpha)}\, f(t) + \frac{\alpha}{B(\alpha)\Gamma(\alpha)}\int_a^t f(\tau)\,(t-\tau)^{\alpha-1}dt \qquad [3.25] $$

The Mittag-Leffler function definition $E_{\alpha,\ \beta}$ is given as:

$$ E_{\alpha,\beta}(z) = \sum_{k=0}^{\infty}\frac{Z^k}{\Gamma(\alpha k+\beta)}\ , \alpha > 0\,, \beta > 0 \qquad [3.26] $$

Before using fractional-order derivatives to solve problems discussed in this research, it is imperative to have a better understanding of these operators by considering previous work done by Tateishi *et al*. (2017), which captures the modifications brought on by the fractional operators on the fractional diffusion equation. This will enable us to understand some of their benefits and drawbacks.

Tateishi *et al*. (2017) conducted an in-depth analysis of the diffusion equation changes because of replacing the well-known Riemann-Liouville operator with the newly suggested operators of Caputo-Fabrizio and Atangana-Baleanu. Their research demonstrates, within the framework of the continuous-time random walk, that the recently discovered fractional operators influence the behavior of waiting time distribution. Their findings show that in the case of Caputo-Fabrizio, an exponential distribution best describes the waiting time distribution. The Atangana-Baleanu operator generates a crossover behavior in which the distribution decays first as an elongated exponential for brief periods and then as a power law for lengthy periods. The Riemann-Liouville operator's exponent describes both of these distributions.

Moreover, by considering all of these distinct fractional operators, Tateishi *et al*. (2017) derived the correct solutions to the fractional diffusion equation and the change in the mean square displacement as a function of time. They discovered that using these novel operators results in non-Gaussian distributions and a range of diffusive states per time duration. Regarding the Caputo-Fabrizio operator, the probability distribution shows a stationary state and saturation diffusion over extended periods. The study further revealed a transition between two different diffusion states for the Atangana-Baleanu operator: a typical, ordinary diffusive state for short durations and a low-diffusive state for an extended period. This characteristic is seen in numerous real-world systems.

Equally important, Tateishi *et al*. (2017) concluded that the correct manipulation of the fractional diffusion with the Caputo-Fabrizio operator restores a diffusive process with random resetting, leading one to conclude that the new fractional operators may be coupled with other diffusive models. Moreover, a fractional diffusion equation with derivatives of dispersed order may be linked with the equation that contains the Atangana-Baleanu operator. These novel fractional operators may therefore be an easy and effective way to incorporate a variety of memory effects, opening up new avenues of investigation into modeling and researching irregular diffusive processes.

3.2.3 Probability Distributions Related to Groundwater Flow and Solute Transport Parameters

Groundwater flow models come with some uncertainty in the real world, so statistical analysis can also be used to deal with these uncertainties. However, the main problem with using these approaches is that they cannot be used until the statistical properties of the random variables of interest (such as the mean, variance, and covariance) have been estimated. Still, it is hard to figure out these statistical characteristics when there is insufficient data.

When performing statistical analysis, any uncertainty in hydrology is addressed by employing probability distribution. The most widely used probability distributions are the Pareto distribution, the Mittag-Leffler distribution, and the Poisson distribution. The Pareto distribution is a power-law distribution used to characterize various real-world occurrences in fields as diverse as quality assurance, science, geography, and even insurance. The idea is that only 20% of the actions are responsible for 80% of the results. This indicates that a relatively limited number of factors are responsible for most of our effects.

If X represents a random variable that represents Pareto distribution, then the likelihood of $X > x$ is given by:

$$\overline{F}(x) = Pr(X > x) = \begin{cases} \left(\frac{x_m}{x}\right)^{\alpha} & x \geq x_{m,}, \\ 1 & x < x_m, \end{cases} \qquad [3.27]$$

Where x_m represents the scale parameter and is the minimum positive value of X while α is the positive shape parameter

The Poisson distribution is a discrete distribution that shows how many events happen in a certain amount of time or area of chance. In the context of this paper, this will help determine how many fingers develop per specific period. This distribution needs one parameter, called lambda (λ), representing the expected number of occurrences throughout each time interval. It is bounded between $(0; \infty)$.Poisson distribution is based on the assumption that the event's rate is constant. Secondly. The occurrence of one event does not affect the occurrence of the subsequent event (events are independent of each other)

If X represents a discrete random variable in a Poisson distribution with$\lambda > 0$, then the probability distribution is given by;

$$P(X = x) = \frac{e^{-\lambda}\lambda^{x}}{x!} \qquad [3.28]$$

Where x represents the number of occurrences, e is the Euler number (2.71828), and (!) is the factorial function.

The $E_{\alpha}(z)$ can represent the Mittag-Leffler, and it can be defined as;

$$E_{\alpha}(z) = \sum_{k=0}^{\infty} \frac{Z^{k}}{\Gamma(\alpha k + 1)}\ , \alpha > 0 \qquad [3.29]$$

Therefore, the Mittag-Leffler is the generalization of exponential. When the fractional parameter is 1, we get:

$$E_{1}(z) = \sum_{k=0}^{\infty} \frac{Z^{k}}{\Gamma(k + 1)} = \sum_{k=0}^{\infty} \frac{Z^{k}}{\mathrm{k!}} = \exp\,(Z) \qquad [3.30]$$

We present some graphical representation of the generalized Mittag-Leffler function for different values of fractional order.

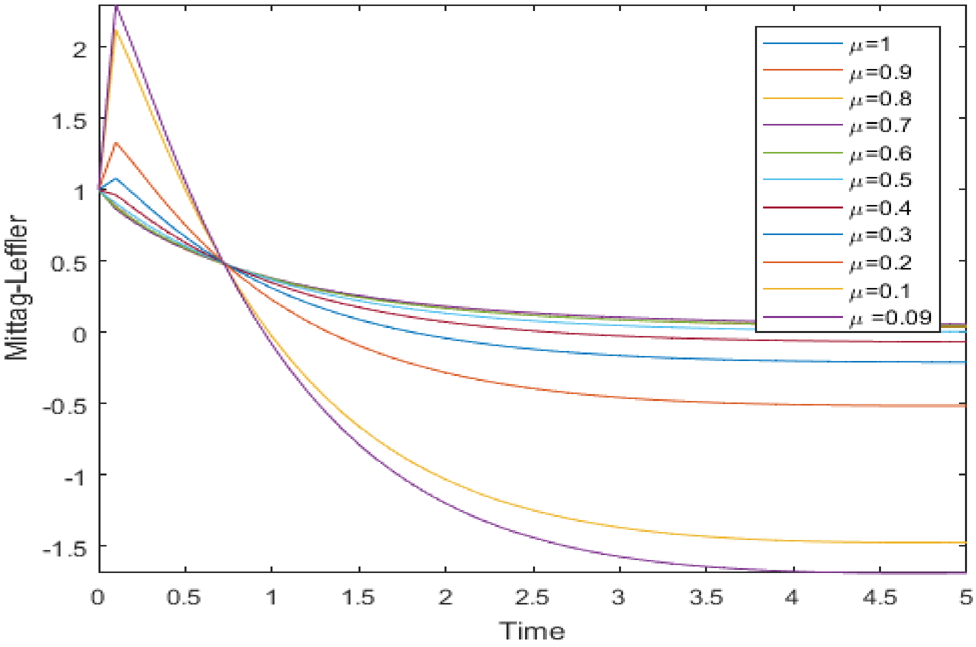

Figure 19 *A graphical representation of the generalized Mittag-Leffler function for different values of fractional order.*

One can see from the above figure that all graphs pass through a fixed point; this point is called the crossover point. Before this point, one can see fading memory effect. After this point, one can see the power law behavior. The distribution associated with this function is known as the Mittag-Leffler distribution and is given below:

$$1 - E_{\alpha}(z) = F(\alpha, z) \qquad [3.31]$$

We present below the graphical representation of this distribution, which depends on the fractional order.

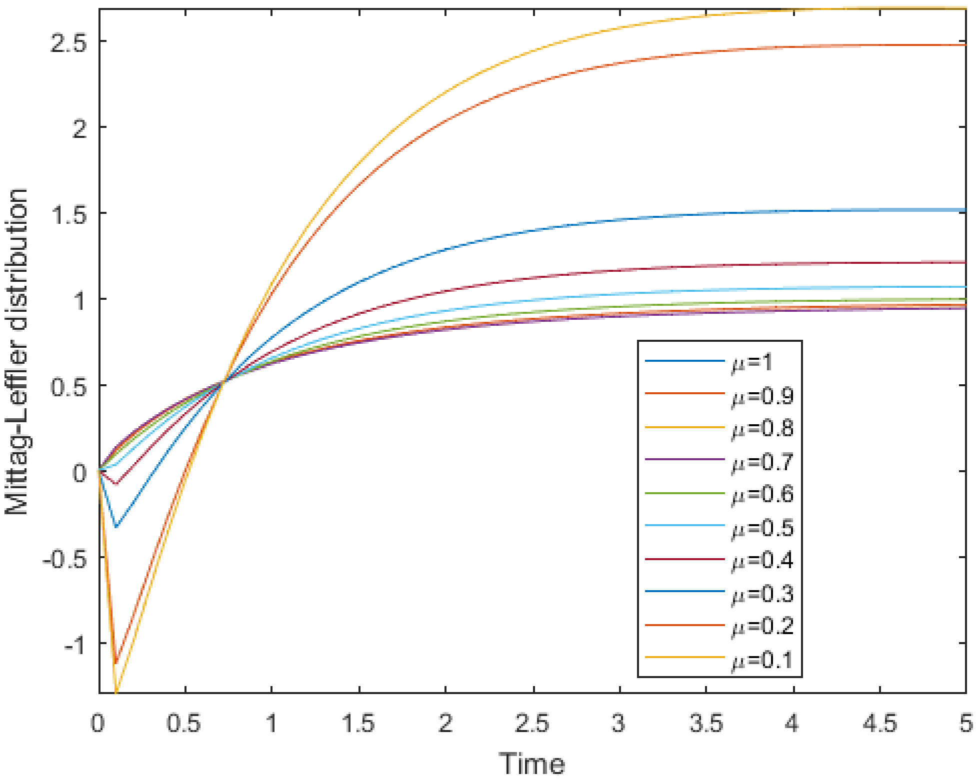

Figure 20 *A graphical representation of the Mittag-Leffler distribution, which depends on the fractional order.*

A crossover behavior is also observed in the distribution. We, however, note that the function misbehaves when the fractional order is less than 0.5, as it gives a negative distribution around zero.

3.4 Conclusion

This chapter provides valuable insight into the dissolution trapping mechanism since it forms the basis of this dissertation. We explain the development of fingers during the convective dissolution process. Moreover, factors controlling the convective dissolution are outlined. Equally important, the mathematical formulations governing the movement of the convective fingers during the dissolution process are defined. We also considered how the capillary transition zone would affect the two-phase buoyancy-driven flow (***Figure 18***).

Moreover, a quick overview of the concepts of fractional differentiation and various fractional differentiation operators is given. Equally important, the previous work done using these operators is included to highlight their benefits and drawbacks in the last part of the fractional differentiation section. Lastly, the various probability distributions linked to groundwater flow are highlighted.

CHAPTER 4 CAPTURING OF FINGERING WITH POWER LAW FUNCTIONS

4.1Introduction

Generally, a mathematical model for groundwater problems is represented by equations expressing relations between variables and parameters. It is usually associated with the specification of system geometry and boundary conditions. The mathematical model can be solved either analytically or numerically, depending on the problem. Analytical solutions require many simplifying assumptions and are usually limited to relatively simple, linear, and strongly schematized problems resulting in exact solutions. Numerical solutions, unlike analytical solutions, are less burdened by restrictive assumptions and can be used to address non-linear, more complicated problems. Numerical solutions account for complicated real-world systems and provide an approximated solution. In this study, numerical solutions will be used, given the non-local behavior exhibited by the convective fingers in terms of time and space.

Numerous numerical solution methods can be utilized to solve the governing dissolution equation. Therefore, as was said earlier, this investigation aims to develop a new way to model convective fingering of CO_2-rich brine by using the idea of fractional differentiation to yield a new transport equation.

After that, this chapter shows some fractional derivatives and how they can be used to model complex transport problems, such as the process of CO_2 fingering. Then, each approximated solution will be given the numerical solutions and stability analysis.

4.2Modelling with power law processes

This section will discuss the numerical approximations of fractional derivatives utilized most frequently, and it will do so by providing examples. Among these are the fractional derivatives of the Caputo, the fractional derivative of Caputo-Fabrizio, and lastly, the fractional derivative of the Atangana-Baleanu.

4.2.1 Solving differential equations using Caputo derivative

As mentioned early in this investigation, the power function-based Caputo derivative is an excellent way to model changes during the diffusion process (refer to sub-chapter 3.3.2 fractional differentiation). For numerical analysis, the following is a close approximation of the Caputo fractional derivative:

$$ {}_{0}^{C}\mathrm{D}_{t}^{\alpha}\big(f(t)\big) = \frac{1}{\Gamma(1-\alpha)} \int_{0}^{t} (t-\tau)^{-\alpha} \frac{d}{dt} f(\tau) d\tau \quad [4.1] $$

To include the fingering effect with the power law process in the mathematical model, we substitute the classical time derivative with the Caputo power law fractional derivative. By recalling Eq 3.4.5 and Eq 3.4.6, (see 3.3.1 Mathematical formulation), we obtain the following Caputo fractional operator-based formulation of the equation:

$$ {}_{0}^{C}D_{t}^{\alpha}[\emptyset S_w] = \nabla \frac{Kk_{rw}}{\mu_w}.(\nabla P_w - \rho_w g \nabla z) \quad [4.2] $$

$$ {}_{0}^{C}D_{t}^{\alpha}[\emptyset S_n] = \nabla \frac{Kk_{rn}}{\mu_n}.(\nabla P_n - \rho_n g \nabla z) \quad [4.3] $$

Since; $\frac{Kk_{rw}}{\mu_w}$ and $\frac{Kk_{rn}}{\mu_n}$ are constants, our system can be reformulated as;

$$ \frac{\emptyset}{\Gamma(1-\alpha)} \int_{0}^{t} \frac{\partial S_w}{\partial t} (t-\tau)^{-\alpha} d\tau = \frac{Kk_{rw}}{\mu_w} \nabla^2 P_w - \nabla \rho_w g \quad [4.4] $$

$$ \frac{\emptyset}{\Gamma(1-\alpha)} \int_{0}^{t} \frac{\partial S_n}{\partial t} (t-\tau)^{-\alpha} d\tau = \frac{Kk_{rn}}{\mu_n} \nabla^2 P_n - \nabla \rho_n g \quad [4.5] $$

In terms of partial derivative, the above equations can be written as;

$$ \frac{\emptyset}{\Gamma(1-\alpha)} \int_{0}^{t} \frac{\partial S_w}{\partial t} (t-\tau)^{-\alpha} d\tau = \frac{Kk_{rw}}{\mu_w} \left(\frac{\partial^2 P_w}{\partial x^2} - \frac{\partial \rho_w g}{\partial x} \right) \quad [4.6] $$

$$ \frac{\emptyset}{\Gamma(1-\alpha)} \int_{0}^{t} \frac{\partial S_n}{\partial t} (t-\tau)^{-\alpha} d\tau = \frac{Kk_{rn}}{\mu_n} \left(\frac{\partial^2 P_n}{\partial x^2} - \frac{\partial \rho_n g}{\partial x} \right) \quad [4.7] $$

Therefore, the equations above can be re-written as a non-linear fractional equation as follows

$$ {}_{0}^{C}D_{t}^{\alpha}\, S_w(x,t) = f(x,t,P_w,\rho_w) \quad [4.8] $$

$$ {}_{0}^{C}D_{t}^{\alpha}\, S_n(x,t) = f(x,t,P_n,\rho_n) $$

By considering the wetting phase(S_w), we apply the Riemann-Liouville integral on both sides to obtain the following:

$$S_w(x,t) - S_w(x,0) = \frac{1}{\Gamma(\alpha)} \int_0^t (t-\tau)^{\alpha-1} f(x,\tau,P_w,\rho_w) d\tau \qquad [4.9]$$

We assume that $x \in [0, L,]$ and t belong to t $\in [0, T]$

$$x_1 < x_2 < x_3 \dots x_m \text{ where } x_m = L \qquad [4.10]$$
$$t_1 < t_2 < t_3 \dots t_n \text{ where } t_{n+1} = T$$

By considering the point $(x_i, t_{n+1})\, where\, n = 0{,}1{,}2{,}3$ then, the entire system can be written as:

$$S_w(x_i,t_{n+1}) - S_w(x_i,0) = \frac{1}{\Gamma(\alpha)} \int_0^{t_{n+1}} (t_{n+1}-\tau)^{\alpha-1} f(x_i,\tau,P_{wi},\rho_{wi}) d\tau \qquad [4.11]$$

$$S_w(x_i,t_{n+1}) - S_w(x_i,0) = \frac{1}{\Gamma(\alpha)} \sum_{j=0}^{n} \int_{t_j}^{t_{j+1}} (t_{n+1}-\tau)^{\alpha-1} f(x_i,\tau,P_{wi},\rho_{wi}) d\tau$$

$$S_w(x_i,t_{n+1}) - S_w(x_i,0) = \frac{1}{\Gamma(\alpha)} \sum_{j=0}^{n} \int_{t_j}^{t_{j+1}} (t_{n+1}-\tau)^{\alpha-1} p_i(\tau) d\tau$$

We approximate $P_i(\tau)$ and $h_n = \frac{T-0}{n}$

Therefore;

$$S_w(x_i,t_{n+1}) - S_w(x_i,0) = \frac{h_n^\alpha}{\Gamma(\alpha+1)} \sum_{j=0}^{n} p_i(t_i) \delta_{n,j}^\alpha$$

Where

$$\delta_{n,j}^\alpha = (n-j+1)^\alpha - (n-j)^\alpha \qquad [4.12]$$

Now replacing p_i^j into the equation then;

$$S_w(x_i, t_{n+1}) - S_w(x_i, 0) = \frac{h_n^\alpha}{\Gamma(\alpha+1)} \sum_{j=0}^{n} f\left(x_i, t_j, P_{w,i}^j, \rho_{w,i}^j\right) \delta_{n,j}^\alpha \qquad [4.13]$$

Then;

$$S_{w,i}^{h+1} - S_{w,i}^0 = \frac{h_n^\alpha}{\Gamma(\alpha+1)} \sum_{j=0}^{n} f\left(x_i, t_j, P_{w,i}^j, \rho_{w,i}^j\right) \delta_{n,j}^\alpha$$

Noting that;

$$f\left(x_i, t_{j,i}, P_{w,i}^\alpha, p_{w,i}^\alpha\right) = \frac{Kk_{rw}}{\mu_w} \left(\frac{P_{w,i+1}^j - 2P_{w,i}^j + P_{w,i}^j}{(\Delta x)^2} - g \frac{\rho_{w,i+1}^j - \rho_{w,i-1}^j}{2\Delta x} \right)$$

Therefore,

$$S_{w,i}^{n+1} - S_{w,i}^0 = \frac{h_n^\alpha}{\Gamma(\alpha+1)} \sum_{j=0}^{h} \frac{Kk_{rw}}{\mu_w} \left(\frac{P_{w,i+1}^j - 2P_{w,i}^j + P_{w,i-1}^j}{(\Delta x)^2} - g \frac{\rho_{w,i+1}^j - \rho_{w,i-1}^j}{2\Delta x} \right) \delta_{n,j}^\alpha \qquad [4.14]$$

The same applies to the non-wetting phase resulting in the following equation:

$$S_{n,i}^{n+1} - S_{n,i}^0 = \frac{h_n^\alpha}{\Gamma(\alpha+1)} \sum_{j=0}^{h} \frac{Kk_{rn}}{\mu_n} \left(\frac{P_{n,i+1}^j - 2P_{n,i}^j + P_{n,i-1}^j}{(\Delta x)^2} - g \frac{\rho_{n,i+1}^j - \rho_{n,i-1}^j}{2\Delta x} \right) \delta_{n,j}^\alpha \qquad [4.15]$$

The equations below show proof that the Atangana-Baleanu can be written in the Caputo sense

$$\mathcal{L}[{}^{ABC}_{\ \ 0}D_t^\alpha f(t)] = \frac{AB(\alpha)}{1-\alpha} \int_0^t {}^{C}_{0}D_t^\alpha f(t) (t-\tau)^{\alpha-1} E_\alpha \left[-\frac{\alpha}{1-\alpha} (t-\tau)^\alpha \right] d\tau \qquad [4.16]$$

Proof

$$\mathcal{L}[{}^{ABC}_{\ \ 0}D_t^\alpha f(t)] = \frac{AB(\alpha)}{1-\alpha} \frac{\Delta^\alpha \tilde{f}(t)_\Delta - \Delta^{\alpha-1} f(0)}{\Delta^\alpha + \frac{\alpha}{1-\alpha}} \qquad [4.17]$$

$$\mathcal{L}[{}^{ABC}_{\ 0}D_t^{\alpha} f(t)] = \frac{AB(\alpha)}{1-\alpha}\mathcal{L}_t[{}^{C}_{0}D_t^{\alpha} f(t)]\frac{1}{\Delta^{\alpha} + \frac{\alpha}{1-\alpha}}$$

$$\mathcal{L}[{}^{ABC}_{\ 0}D_t^{\alpha} f(t)] = \mathcal{L}_t[{}^{C}_{0}D_t^{\alpha} f(t)] \cdot \frac{AB(\alpha)}{1-\alpha} \cdot \frac{1}{\Delta^{\alpha} + \frac{\alpha}{1-\alpha}}$$

$$\mathcal{L}[{}^{ABC}_{\ 0}D_t^{\alpha} f(t)] = \mathcal{L}_t[{}^{C}_{0}D_t^{\alpha} f(t)]\mathcal{L}_t\left[\frac{AB(\alpha)}{1-\alpha}t^{\alpha-1}E_{\alpha,\alpha}\left[\frac{\alpha}{1-\alpha}t^{\alpha}\right]\right]$$

Using the convolution theorem and Laplace transform the following equation is obtained:

$$ {}^{ABC}_{\ 0}D_t^{\alpha}\big(f(t)\big) = \frac{AB(\alpha)}{1-\alpha}\int\limits_0^t {}^{C}_{0}D_t^{\alpha} f(t)(t-\tau)^{\alpha-1}E_{\alpha,\alpha}\left[-\frac{\alpha}{1-\alpha}(t-\tau)^{\alpha}\right]d\tau \qquad [4.18]$$

Therefore, the Atangana-Baleanu derivative in the Caputo sense can be written as:

$$ {}^{ABC}_{\ 0}D_t^{\alpha}\big(f(t)\big) = \frac{AB(\alpha)}{1-\alpha}\int\limits_0^t {}^{C}_{0}D_t^{\alpha} f(t)(t-\tau)^{\alpha-1}E_{\alpha,\alpha}\left[-\frac{\alpha}{1-\alpha}(t-\tau)^{\alpha}\right]d\tau \qquad [4.19]$$

Similarly, the relation with Rieman-Lioville is given by:

$$ {}^{ABR}_{\ 0}D_t^{\alpha}\big(f(t)\big) = \frac{AB(\alpha)}{1-\alpha}\int\limits_0^t {}^{RL}_{\ 0}D_t^{\alpha} f(t)(t-\tau)^{\alpha-1}E_{\alpha,\alpha} \cdot \left[-\frac{\alpha}{1-\alpha}(t-\tau)^{\alpha}\right]d\tau \qquad [4.20]$$

Because the results depict that:

$$\begin{aligned} {}^{ABC}_{\ 0}D_t^{\alpha}\big(f(t)\big) &= {}^{C}_{0}D_t^{\alpha} f(t) * t^{\alpha-1}E_{\alpha,\alpha} \cdot \left[-\frac{\alpha}{1-\alpha}(t)^{\alpha}\right] \qquad [4.21] \\ {}^{ABR}_{\ 0}D_t^{\alpha}\big(f(t)\big) &= {}^{RL}_{\ 0}D_t^{\alpha} f(t) * t^{\alpha-1}E_{\alpha,\alpha} \cdot \left[-\frac{\alpha}{1-\alpha}(t)^{\alpha}\right] \end{aligned}$$

Motivation for using Caputo derivative

The Caputo fractional derivative is a convolution of the classical derivative and power law function. The fingering process could follow long-range dependency, where the observed fingering has a long tail. It has been recognized in the last decades that processes with long-tailed behaviors can be replicated appropriately using the power law function. Therefore, to include in the mathematical formulation the effect of the long tail, a differential operator based on the power law should be used. In this case, the classical time partial derivative will be replaced using the derivatives with the power law, which corresponds to the Caputo fractional derivative. It is worth noting that the effect of the Laplace transform on a Caputo fractional derivative of a differentiable function leads to the usual initial condition, unlike the Riemann-Liouville type. To accommodate readers that are not used to the concept of fractional differentiation, we present here the definition of the Caputo fractional derivative of a differentiable function f with fractional order α

The equation below represents the Laplace transform of the Caputo derivative

$$
{}_{0}^{C}\mathrm{D}_{t}^{\alpha}\big(f(t)\big) = \frac{1}{\Gamma(1-\alpha)}\int_{0}^{t}(t-\tau)^{-\alpha}\frac{d}{dt}f(\tau)d\tau \qquad [4.22]
$$

$$
{}_{0}^{C}\mathrm{D}_{t}^{\alpha}\big(f(t)\big) \ = f'(t) * \frac{t^{-\alpha}}{\Gamma(1-\alpha)}
$$

$$
\mathcal{L}[{}_{0}^{C}D_{t}^{\alpha}f(t)] = \mathcal{L}\big(f'^{(t)}\big)\mathcal{L}\left(\frac{t^{-\alpha}}{\Gamma(1-\alpha)}\right) \qquad [4.23]
$$

$$
\mathcal{L}[{}_{0}^{C}D_{t}^{\alpha}f(t)] = \left(\Delta\tilde{f}(\Delta) - f(0)\right)\Delta^{\alpha-1}
$$

$$
\mathcal{L}[{}_{0}^{C}D_{t}^{\alpha}f(t)] = \Delta^{\alpha}\tilde{f}(\Delta) - \Delta^{\alpha-1}f(0)
$$

In this section, we present the effect of the power law when its acts on a given function through the Bode diagram and phase diagram. To achieve this, we consider an exponential function. The Laplace transform of an exponential function $exp(at)$ is given as:

$$
\mathcal{L}(exp(at)\,) = \frac{1}{\Delta - a} \qquad [4.24]
$$

Therefore, using the formula presented above, we have that the Laplace transform of the Caputo derivative of an exponential function is given:

$$
\mathcal{L}[{}_{0}^{C}D_{t}^{\alpha}exp(at)] = \frac{\Delta^{\alpha}}{\Delta - a} - \Delta^{\alpha-1} \qquad [4.25]
$$

To show the effect of this differential operator, we first present the Bode diagram and phase diagram of the derivative of the exponential function when the parameter $a = 2$

$$\mathcal{L}\left[\frac{d}{dt}(exp(at))\right] = \frac{\Delta}{\Delta - 2} - 1 \qquad [4.26]$$

The graphical representation is provided below.

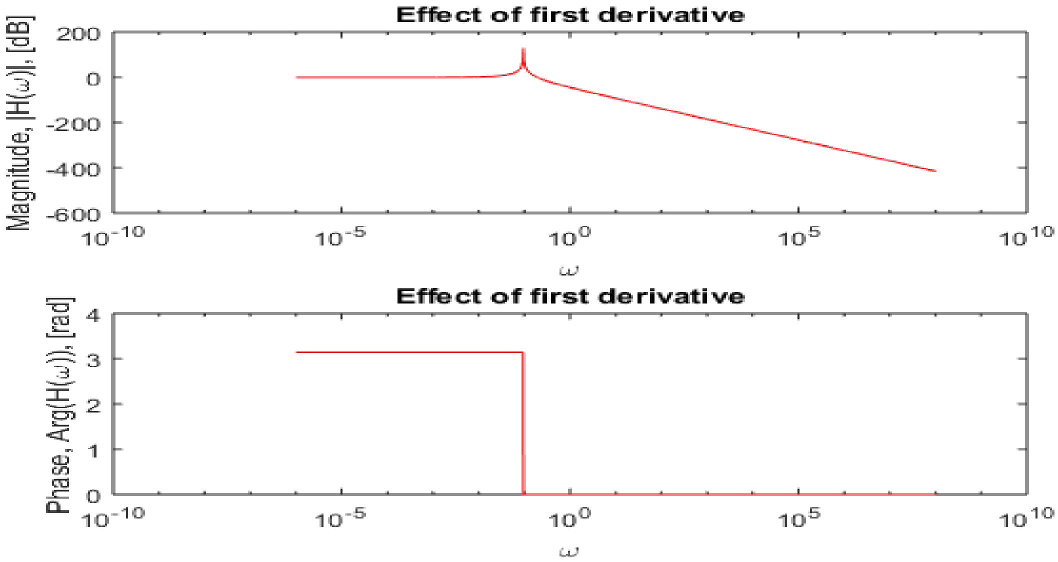

Figure 21 *Bode and phase diagram for the derivative of the exponential function*

We present below the effect of the Caputo derivative on the exponential function. The numerical simulations are presented in the following figures below.

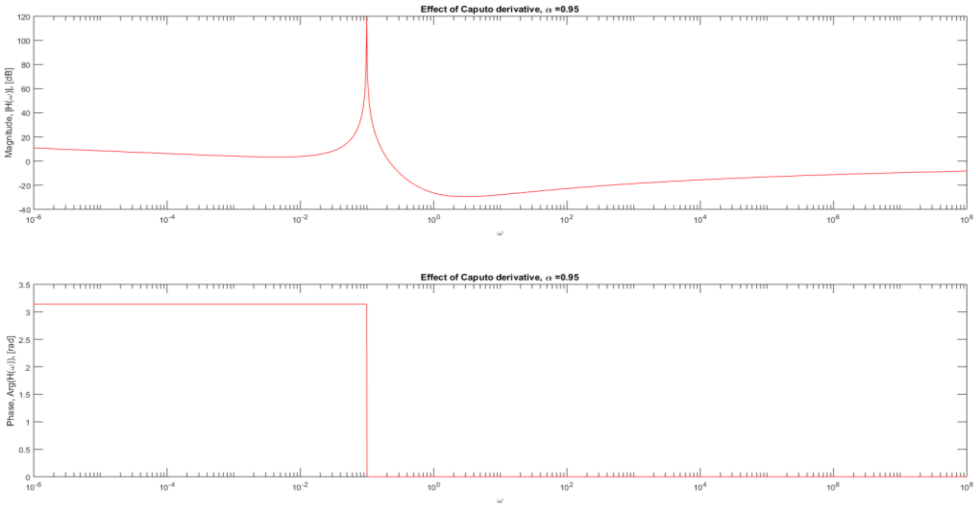

Figure 22 *Bode and phase diagram for the Caputo derivative of the exponential function*

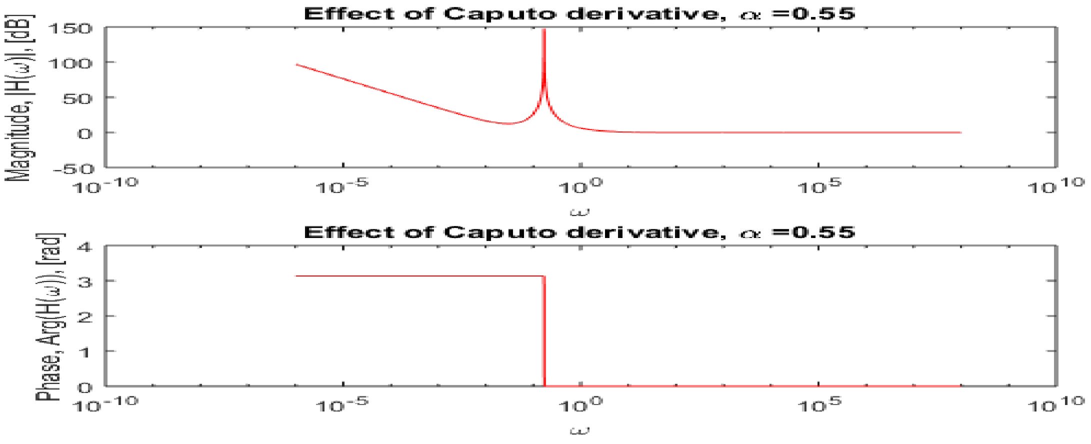

Figure 23 *Bode and phase diagram for the Caputo derivative of the exponential function*

The above-mentioned numerical results clearly distinguish between the effects of the classical derivative and the Caputo power law derivative. A confirmation that the Caputo-fractional derivative can only duplicate systems with long tail tendencies is the fact that the Bode diagram for the Caputo fractional derivative displays no change in size.

4.2.2 Solving differential equations using Caputo Fabrizio (CF) derivative

It was recently discovered that the exponential law could be used to derive a novel derivative, which Caputo and Fabrizio have termed the "Caputo-Fabrizio derivative". This derivative is a non-singular kernel. It has successfully characterized complicated diffusion regimes at various sizes (refer to sub-chapter**3**.3.2 **Fractional** differentiation). The CF derivative includes several different memory effects, which opens up new lines of inquiry into the modeling and analysis of irregular diffusive processes. As a result, the CF derivative will be used in this investigation to solve the convective dissolution issues. It has been determined that the well-known Caputo-Fabrizio operator is:

$$ {}^{CF}_{0}D_t^{\alpha}\big(f(t)\big) = \frac{1}{1-\alpha}\int_0^t \frac{\partial}{\partial t} f'(\tau) exp\left[-\frac{\alpha}{1-\alpha}(t-\tau)\right] d\tau \qquad [4.27] $$

Similarly, to include the fingering effect in Caputo Fabrizio, we substitute the classical time derivative with the Caputo Fabrizio power law function to give the following equation:

$$ {}_{0}^{CF}D_t^{\alpha}[\emptyset S_w] = \nabla \frac{Kk_{rw}}{\mu_w}.(\nabla P_w - \rho_w g \nabla z) \qquad [4.28a]$$

$$ {}_{0}^{CF}D_t^{\alpha}[\emptyset S_n] = \nabla \frac{Kk_{rn}}{\mu_n}.(\nabla P_n - \rho_n g \nabla z) \qquad [4.28b]$$

Since; $\frac{Kk_{rw}}{\mu_w}$ and $\frac{Kk_{rn}}{\mu_n}$ are constants, our system can be reformulated as;

$$\frac{1}{1-\alpha}\int_a^t exp\left[-\frac{\alpha}{1-\alpha}(t-\tau)\right]\emptyset S_w'(x,\tau)d\tau = \frac{Kk_{rw}}{\mu_w}(\nabla^2 P_w - \nabla \rho_w g) \qquad [4.29a]$$

$$\frac{1}{1-\alpha}\int_a^t exp\left[-\frac{\alpha}{1-\alpha}(t-\tau)\right]\emptyset S_n'(x,\tau)d\tau = \frac{Kk_{rn}}{\mu_n}(\nabla^2 P_n - \nabla \rho_n g) \qquad [4.30b]$$

By recalling that the terms on the right-hand side can be written such that:

$$f(x,t,P_w,p_w) = \nabla \frac{Kk_{rw}}{\mu_w}(\nabla P_w - \rho_w g \nabla z) \qquad [4.31]$$

When the following non-linear fractional equation that is written in terms of the Caputo-Fabrizio fractional operator is taken into consideration, then:

$$ {}_{0}^{CF}D_t^{\alpha}(S_w) = f(x,t,P_w,\rho_w) \qquad [4.32]$$

Or

$$f(x,t,P_w,p_w) = \frac{1}{1-\alpha}\int_0^t \emptyset S_w'(x,\tau) exp\left[-\frac{\alpha}{1-\alpha}(t-\tau)\right]dt \qquad [4.33]$$

By using the fundamentals theorem of calculus, the equation above can be re-written as:

$$S_w(x,t) - S_w(x,0) = (1-\alpha)f(x,t,P_w,\rho_w) + \alpha\int_0^t f(x,t,P_w,\rho_w)d\tau \qquad [4.34]$$

By considering a point at (x_i, t_{n+1}) where $n =$ 0.1.2.3 ..., then the above equation is written as:

$$S_w(x_i,t_{n+1}) = S_w(x_i,0) + (1-\alpha)f(x_i,t_n,P_w,\rho_w) + \alpha\int_0^{t_{n+1}} f(x_i\tau,P_w,\rho_w)\,d\tau \qquad [4.35]$$

At a given point (x_i,t_n) then:

$$S_w(x_i,t_n) = S_w(x_i,0) + (1-\alpha)f(x_i,t_{n-1},P_w,\rho_w) + \alpha\int_0^{t_n} f(x_i\tau,P_w,\rho_w)\,d\tau \qquad [4.36]$$

Now by subtracting equation the two equations, the following equation is obtained:

$$\begin{aligned} S_{w,i}^{n+1} - S_{w,i}^{n} &= (1-\alpha)[f(x_i,t_n,P_w^n,\rho_w^n) - f(x_i,t_{n-1},P_w^{n-1},\rho_w^{n-1})] \qquad [4.37] \\ &+ \alpha\int_{t_n}^{t_{n+1}} f\left(x_i,\tau,P_{w,i},\rho_{w,i}\right)d\tau \end{aligned}$$

Therefore:

$$\begin{aligned} S_{w,i}^{n+1} - S_{w,i}^{n} &= (1-\alpha)[f(x_i,t_n,P_w^n,\rho_w^n) - f(x_i,t_{n-1},P_w^{n-1},\rho_w^{n-1})] \qquad [4.38] \\ &+ \alpha\left[\frac{3}{2}\Delta t f(x_i,t_n,P_w^n,\rho_w^n) - \frac{\Delta t}{2} f(x_i,\tau,P_w^{n-1},\rho_w^{n-1})\right] \end{aligned}$$

By remembering that:

$$f(x,t,P_w,\rho_w) = \nabla\frac{Kk_{rw}}{\mu_w}(\nabla P_n - \rho_w g\nabla z)$$

At this point the function $f(x_i,t_n,P_w^n,\rho_w^n)$ and $f(x_i,t_{n-1},P_w^{n-1},\rho_w^{n-1})$ can be represented as:

$$f\left(x_i,t_n,P_{w,i}^n,p_{w,i}^n =\right)\frac{Kk_{rn}}{\mu_n}\left(\frac{P_{w,i+1}^n - 2P_{w,i}^n + P_{w,i-1}^n}{(\Delta x)^2} - g\frac{\rho_{w,i+1}^n - \rho_{w,i-1}^n}{2\Delta x}\right) \qquad [4.39]$$

$$f\left(x_i,t_{n-1},P_w^{n-1},p_{w,i}^{n-1}\right) = \frac{Kk_{rn}}{\mu_n}\left(\frac{P_{w,i+1}^{n-1} - 2P_{w,i}^{n-1} + P_{w,i-1}^{n-1}}{(\Delta x)^2} - g\frac{\rho_{w,i+1}^{n-1} - \rho_{w,i-1}^{n-1}}{2\Delta x}\right) \qquad [4.40]$$

The equation based on the Caputo-Fabrizio integral operator after discretization is as follows:

$$\begin{aligned} S_w^{n+1} - S_w^n = (1-\alpha)\Bigg[&\frac{Kk_{rw}}{\mu_w}\left(\frac{P_{w,i+1}^n - 2P_{w,i}^n + P_{w,i-1}^n}{(\Delta x)^2} - g\frac{\rho_{w,i+1}^n - \rho_{w,i-1}^n}{2\Delta x}\right) \\ &- \frac{Kk_{rw}}{\mu_w}\left(\frac{P_{w,i+1}^{n-1} - 2P_{w,i}^{n-1} + P_{w,i-1}^{n-1}}{(\Delta x)^2} - g\frac{\rho_{w,i+1}^{n-1} - \rho_{w,i-1}^{n-1}}{2\Delta x}\right)\Bigg] \\ &+ \alpha\left[\frac{3}{2}\Delta t\frac{Kk_{rw}}{\mu_w}\left(\frac{P_{w,i+1}^n - 2P_{w,i}^n + P_{w,i-1}^n}{(\Delta x)^2} - g\frac{\rho_{w,i+1}^n - \rho_{w,i-1}^n}{2\Delta x}\right)\right. \\ &\left.- \frac{\Delta t}{2}\frac{Kk_{rw}}{\mu_w}\left(\frac{P_{w,i+1}^{n-1} - 2P_{w,i}^{n-1} + P_{w,i-1}^{n-1}}{(\Delta x)^2} - g\frac{\rho_{w,i+1}^{n-1} - \rho_{w,i-1}^{n-1}}{2\Delta x}\right)\right] \end{aligned} \qquad [4.41]$$

The same applies to the non-wetting phase in the system resulting in the following:

$$\begin{aligned} S_n^{n+1} - S_n^n = (1-\alpha)\Bigg[&\frac{Kk_{rn}}{\mu_n}\left(\frac{P_{n,i+1}^n - 2P_{n,i}^n + P_{n,i-1}^n}{(\Delta x)^2} - g\frac{\rho_{n,i+1}^n - \rho_{n,i-1}^n}{2\Delta x}\right) \\ &- \frac{Kk_{rn}}{\mu_n}\left(\frac{P_{n,i+1}^{n-1} - 2P_{n,i}^{n-1} + P_{n,i-1}^{n-1}}{(\Delta x)^2} - g\frac{\rho_{n,i+1}^{n-1} - \rho_{n,i-1}^{n-1}}{2\Delta x}\right)\Bigg] \\ &+ \alpha\left[\frac{3}{2}\Delta t\frac{Kk_{rn}}{\mu_n}\left(\frac{P_{n,i+1}^n - 2P_{n,i}^n + P_{n,i-1}^n}{(\Delta x)^2} - g\frac{\rho_{n,i+1}^n - \rho_{n,i-1}^n}{2\Delta x}\right)\right. \\ &\left.- \frac{\Delta t}{2}\frac{Kk_{rn}}{\mu_n}\left(\frac{P_{n,i+1}^{n-1} - 2P_{n,i}^{n-1} + P_{n,i-1}^{n-1}}{(\Delta x)^2} - g\frac{\rho_{n,i+1}^{n-1} - \rho_{n,i-1}^{n-1}}{2\Delta x}\right)\right] \end{aligned} \qquad [4.42]$$

4.2.3 Solving differential equations using Atangana-Baleanu derivative

Complex geological settings influence groundwater flow and transport; hence, a differential operator is required to capture this. Atangana and Baleanu have proposed a new fractional derivative based on the generalized Mittag-Leffler function. This Mittag-Leffler function is the generalization of the exponential function. Non-singular and non-local kernels are used in the Atangana-Baleanu derivative (Gomez et al., 2019). This work intends to use the AB derivative's success in solving real-world issues to tackle convective dissolution difficulties. The new AB derivative in the sense of Caputo can be expressed as:

$${}^{ABC}_{\ a}D_t^{\alpha}\big(f(t)\big) = \frac{1}{1-\alpha}\int_0^t \frac{d}{d\tau} f(\tau) E_\alpha\left[-\alpha\frac{(t-\tau)^\alpha}{1-\alpha}\right] d\tau \qquad [4.43]$$

In the Riemann-Liouville sense, the definition of an Atangana-Baleanu fractional derivative is given as:

Let f∈H¹ (a, b) b>a, α∈[0, 1]

$$ {}^{ABR}_{a}D_t^{\alpha} f(t) = \frac{1}{1-\alpha}\frac{d}{dt}\int_a^t f(\tau)E_\alpha\left[-\alpha\frac{(t-\tau)^\alpha}{1-\alpha}\right]d\tau; \quad 0<\alpha<1 \qquad [4.44] $$

In the sense of Caputo, the term "Atangana-Baleanu fractional derivative" is defined as:

$Let\ f \in\ H1\ (a,b)), b > a, \alpha \in\ [0,1]$

$$ {}^{ABR}_{a}D_t^{\alpha} f(t) = \frac{B(\alpha)}{1-\alpha}\int_a^t f'\,(\tau)E_\alpha\left[-\alpha\frac{(t-\tau)^\alpha}{1-\alpha}\right]d\tau; \quad 0<\alpha<1 \qquad [4.45] $$

Similarly, to include the fingering effect in Atangana-Baleanu, we replace the classical time derivative with the Atangana-Baleanu power law function to give the following equation:

$$ {}^{ABC}_{0}D_t^{\alpha}[\emptyset S_w] = \nabla\frac{Kk_{rw}}{\mu_w}.(\nabla P_w - \rho_w g\nabla z) \qquad [4.46a] $$

$$ {}^{ABC}_{0}D_t^{\alpha}[\emptyset S_n] = \nabla\frac{Kk_{rn}}{\mu_n}.(\nabla P_n - \rho_n g\nabla z) \qquad [4.47b] $$

Since; $\frac{Kk_{rw}}{\mu_w}$ and $\frac{Kk_{rn}}{\mu_n}$ are constants, our system can be reformulated as;

$$ \frac{1}{1-\alpha}\int_a^t E_\alpha\left[-\frac{\alpha}{1-\alpha}(t-\tau)^\alpha\right]\emptyset S_w'(\tau)d\tau = \frac{Kk_{rw}}{\mu_w}(\nabla^2 P_w - \nabla\rho_w g) \qquad [4.48a] $$

$$ \frac{1}{1-\alpha}\int_a^t E_\alpha\left[-\frac{\alpha}{1-\alpha}(t-\tau)^\alpha\right]\emptyset S_n' d\tau = \frac{Kk_{rn}}{\mu_n}(\nabla^2 P_n - \nabla\rho_n g) \qquad [4.49b] $$

The Atangana-Baleanu fractional integral of order alpha of a function $f(t)$ is written as:

$$ {}^{ABC}_{a}I_t^{\alpha} f(t) = \frac{1-\alpha}{B(\alpha)}f(t) + \frac{\alpha}{B(\alpha)\Gamma(\alpha)}\int_a^t f(\tau)(t-\tau)^{\alpha-1}d\tau \qquad [4.50] $$

Thus, in a Caputo sense, consider the non-linear fractional equation below written in terms of the Atangana-Baleanu fractional derivative (ABC).

$$ {}^{ABC}_{\ 0}D_t^{\alpha} S_w(x,t) = f\big(x,t,P_{w,}p_w\big) \qquad [4.51]$$

$$\begin{aligned} &S_w(x,t) - S_w(x,0) \qquad [4.52] \\ &\quad = (1-\alpha) f\big(x,t,P_{w,}p_w\big) + \frac{\alpha}{\Gamma(\alpha)} \int_0^t f\big(x,\tau,P_{w,}\rho_w\big)\,(t-\tau)^{\alpha-1} d\tau \end{aligned}$$

By considering a point at (x_i, t_{n+1}) where $n = 0,1,2,3$ .... we have:

$$\begin{aligned} &S_w(x_i,t_{n+1}) - S_w(x_i,0) \qquad [4.53] \\ &\quad = (1 \\ &\quad - \alpha) f\big(x_i,t_{n+1},P_{w,}p_w\big) \frac{\alpha}{\Gamma(\alpha)} \int_0^{t_{n+1}} f\big(x_i,\tau,P_{w,}\rho_w\big)\,(t_{n+1}-\tau)^{\alpha-1} d\tau \\ &\quad = (1-\alpha) f\big(x_i,t_{n+1},P_{w,}p_w\big) \frac{\alpha}{\Gamma(\alpha)} \sum_{j=0}^{n} \int_{t_j}^{t_{j+1}} f\big(x_i,\tau,P_{w,}\rho_w\big)\,(t_{n+1}-\tau)^{\alpha-1} d\tau \end{aligned}$$

Let $p_{xi}\big(\tau, v(\tau)\big) = f\big(x_i,t,P_{w,}\rho_w\big)$ Where:$v(\tau) = u(x_i,\tau)$ therefore:

$$v_{n+1} - v(0) = (1-\alpha) p_{xi}(t_{n+1}, v_{n+1}) + \frac{\alpha}{\Gamma(\alpha)} \int_0^{t_{n+1}} (t_{n+1}-\tau)^{\alpha-1} p_{xi}\big(\tau, v(\tau)\big) d\tau \qquad [4.54]$$

The integration portion of the above equation can be approximated by using the trapezoidal quadrature rule and give:

$$\begin{aligned} &\int_0^{t_{n+1}} (t_{n+1}-\tau)^{\alpha-1}\, p_{xi}\big(\tau, v(\tau)\big) d\tau \qquad [4.55] \\ &\approx \int_0^{t_{n+1}} (t_{n+1}-\tau)^{\alpha-1}\, \tilde{p}_{xi,n+1}(\tau) d\tau \end{aligned}$$

Where $\tilde{p}_{n+1}(\tau)$ is the following piecewise linear interpolation polynomial gives pn+1τ

$$\tilde{p}_{xi,n+1}(\tau) \approx \frac{t_{m+1}-\tau}{t_{m+1}-t_m} p_{xi}(t_m, x_m) + \frac{\tau - t_n}{t_{n+1}-t_n} p_{xi}(t_{m+1}, x_{m+1}) \;\; 0 \leq m \leq n \tag*{[4.56]}$$

Using the above approximation for the right-hand-side of the equation, the product of the trapezoidal quadrature rule is derived from giving:

$$\int_{0}^{t_{n+1}} (t_{n+1}-\tau)^{\alpha-1} \tilde{p}_{xi,n+1}(\tau) d\tau = \frac{h_N^{\alpha}}{\alpha(\alpha+1)} \sum_{m=0}^{n} a_{n+1,m}^{(\alpha)} \, p_{xi}(t_m, x_m) \tag*{[4.57]}$$

Where:

$$a_{n+1,m}^{(\alpha)} = \begin{cases} -(n-\alpha)(n+1)^{\alpha}+, m = 0 \\ (n-m)^{\alpha+1} - 2(n-m+1)^{\alpha+1} + \\ (n-m+2)^{\alpha+1}, 1 \leq m \leq n, 1, m = n+1 \end{cases} \tag*{[4.58]}$$

Lastly, the corrector formula is given by:

$$v(t_{n+1}) - v(0) = \frac{\alpha h_N^{\alpha}}{\Gamma(\alpha+2)} \left(\hat{a}_{n+1,n+1}^{(\alpha)} \, p\left(t_{n+1}, v_{n+1}^{p_r}\right) + \sum_{m=0}^{n} a_{n+1,m}^{(\alpha)} \; p(t_n, v_m) \right) \tag*{[4.59]}$$

Where $\hat{a}_{n+1,n+1}^{(\alpha)} = 1 + \frac{(1-\alpha)\Gamma(\alpha+2)}{\alpha h_N^{\alpha}}$ [4.60]

The product rectangle rule is used to derive the predictor equations. As a result, the predictor equation is derived from the following:

$$v_{n+1}^{p_r} - v(0) = \frac{h_N^{\alpha}}{\Gamma(\alpha)} \sum_{m=0}^{n} \hat{b}_{n+1,m}^{(\alpha)} \, p(t_m, v_m) \tag*{[4.61]}$$

Where:

$$\hat{b}_{n+1,m}^{(\alpha)} = \begin{cases} b_{n+1,m}^{(\alpha)}, m = 0, \ldots\ldots, n-1 \\ 1 + \dfrac{(1-\alpha)\Gamma(\alpha)}{h_N^{\alpha}} \; , m = n \end{cases} \tag*{[4.62]}$$

Therefore:

$$v(t_{n+1}) = S_{xi}^{n+1} \tag*{[4.63]}$$

$$v(0) = S_{xi}^{0}$$

As a result:

$$S_{xi}^{n+1} - S_{xi}^{0} = \frac{\alpha h_N^{\alpha}}{\Gamma(\alpha+2)}\left(\hat{a}_{n+1,n+1}^{(\alpha)}\, p\left(t_{n+1}, v_{n+1}^{p_r}\right) + \sum_{m=0}^{n} a_{n+1,m}^{(\alpha)}\, p(t_n, v_m)\right) \qquad [4.64]$$

Remembering that:

$$p_{xi}\left(\tau, v(\tau)\right) = f\left(x_i, t_{j,i}, P_{w,i}^{\alpha}, \rho_{w,i}^{\alpha}\right) = \frac{Kk_{rw}}{\mu_w}\left(\frac{p_{w,i+1}^{j} - 2p_{w,i}^{j} + p_{w,i}^{j}}{(\nabla x)^2} - g\,\frac{\rho_{w,i+1}^{j} - \rho_{w,i-1}^{j}}{2\nabla x}\right) \qquad [4.65]$$

Therefore:

$$S_{xi}^{n+1} - S_{xi}^{0} = \frac{\alpha h_N^{\alpha}}{\Gamma(\alpha+2)}\left(\hat{a}_{n+1,n+1}^{(\alpha)}\, p\left(t_{n+1}, v_{n+1}^{p_r}\right)\right.$$
$$\left. + \sum_{m=0}^{n} a_{n+1,m}^{(\alpha)} \frac{Kk_{rw}}{\mu_w}\left(\frac{p_{w,i+1}^{j} - 2p_{w,i}^{j} + p_{w,i}^{j}}{(\Delta x)^2} - g\,\frac{\rho_{w,i+1}^{j} - \rho_{w,i-1}^{j}}{2\Delta x}\right)\right) \qquad [4.66]$$

The resulting wetting phase and non-wetting phase equations are as follows respectively:

[4.67]

$$S_{w}^{n+1} - S_{w}^{0} = \frac{\alpha h_N^{\alpha}}{\Gamma(\alpha+2)}\left(\hat{a}_{n+1,n+1}^{(\alpha)}\, p\left(t_{n+1}, v_{n+1}^{p_r}\right)\right.$$
$$\left. + \sum_{m=0}^{n} a_{n+1,m}^{(\alpha)} \frac{Kk_{rw}}{\mu_w}\left(\frac{p_{w,i+1}^{j} - 2p_{w,i}^{j} + p_{w,i}^{j}}{(\Delta x)^2} - g\,\frac{\rho_{w,i+1}^{j} - \rho_{w,i-1}^{j}}{2\Delta x}\right)\right)$$

And

[4.68]

$$S_{n}^{n+1} - S_{n}^{0} = \frac{\alpha h_N^{\alpha}}{\Gamma(\alpha+2)}\left(\hat{a}_{n+1,n+1}^{(\alpha)}\, p\left(t_{n+1}, v_{n+1}^{p_r}\right)\right.$$
$$\left. + \sum_{m=0}^{n} a_{n+1,m}^{(\alpha)} \frac{Kk_{rn}}{\mu_n}\left(\frac{p_{n,i+1}^{j} - 2p_{n,i}^{j} + p_{n,i}^{j}}{(\Delta x)^2} - g\,\frac{\rho_{n,i+1}^{j} - \rho_{n,i-1}^{j}}{2\Delta x}\right)\right)$$

4.3 Non-dimensional equations

$$\eta = \frac{x}{H}, \varsigma = \frac{z - h_o}{H}, \tau = \frac{D_0}{H^2}t, \xi = \frac{\varsigma}{\sqrt{4\tau}}, \qquad [4.69]$$

The stream function, capillary pressure, concentration, and saturation are written as follows, respectively:

$$\psi = \frac{\psi}{D_0\varphi}, P_c = \frac{P_c}{\Delta\rho_{wn} gH}, C = \frac{C_d^w}{C_0}, S = \frac{S_w - S_{wr}}{1 - S_{wr}} \quad [4.70]$$

Where the effective porosity of the two-phase system is defined as$\varphi = \phi(1 - S_{wr})$, and the density differential between the non-wetting phase and the wetting phase is defined as $\Delta\rho_{wn} = \rho_w - \rho_{n.}$

Moreover, the system of questions can be investigated using non-dimensionless parameters named:

$$Ca = \frac{H}{h_0}\ (capillary\ number) \quad [4.71]$$

$$Ra = \frac{k\Delta\rho_d^w gH}{D_0\varphi\mu_w} (Raleigh\ number) \quad [4.72]$$

Where the density difference between the solutes, which is caused by the dissolution of the CO2 into the resident brine, is defined as $\Delta\rho_d^w = \rho_{w0}\beta c_0$, and h_0 depicts the rice in capillarity, where the system parameters dependence is given by Leverett scaling;

$$h_0 \sim \frac{\gamma cos\theta}{\Delta\rho_{nw} g\sqrt{k/\varphi}} \quad [4.73]$$

Where the surface tension between the CO2 and the brine is represented byγ, and the contact angle (wettability) between the fluid phase interface and the solid surface is defined by θ (Hamid, 2015)

Accordingly, based on the above dimensionless parameters, the governing equations for flow, brine saturation, and transport can be depicted as follows:

$$\nabla^2\psi = k_{rw} Ra \frac{\partial C}{\partial\eta} \quad [4.74]$$

All equations are under the following boundary conditions:

$$\psi\left(\eta, \varsigma = -\frac{h_0}{H}, \tau\right) = 0, \psi(\eta, \varsigma = 1, \tau) = 0 \quad [4.75]$$

$$S\left(\eta, \varsigma = -\frac{h_0}{H}, \tau\right) = 0, S(\eta, \varsigma = 1, \tau) = 1 \quad [4.76]$$

$$C\left(\eta, \varsigma = -\frac{h_0}{H}, \tau\right) = 1, C(\eta, \varsigma = 1, \tau) = 0 \quad [4.77]$$

The van Genuchten-Mualem model is used to figure out the functional forms of the relationships between relative permeability and capillary pressure.

$$k_{rn}(S) = (1-S)^{\frac{1}{3}}\left[1 - S^{\frac{1}{m}}\right]^{2m} \qquad [4.78]$$

$$k_{rw}(S) = S^{\frac{1}{2}}\left[1 - \left(1 - S^{\frac{1}{m}}\right)^{m}\right]^{2} \qquad [4.79]$$

$$J(S) = \left(s^{-\frac{1}{m}} - 1\right)^{\frac{1}{\Lambda}} \qquad [4.80]$$

Where $m = 1 - \frac{1}{\Lambda}$, and Λ is a measure of grain sorting in a porous medium that affects the material parameter. Graphs of these functions are plotted in **Figure 24** and **Figure 25** below:

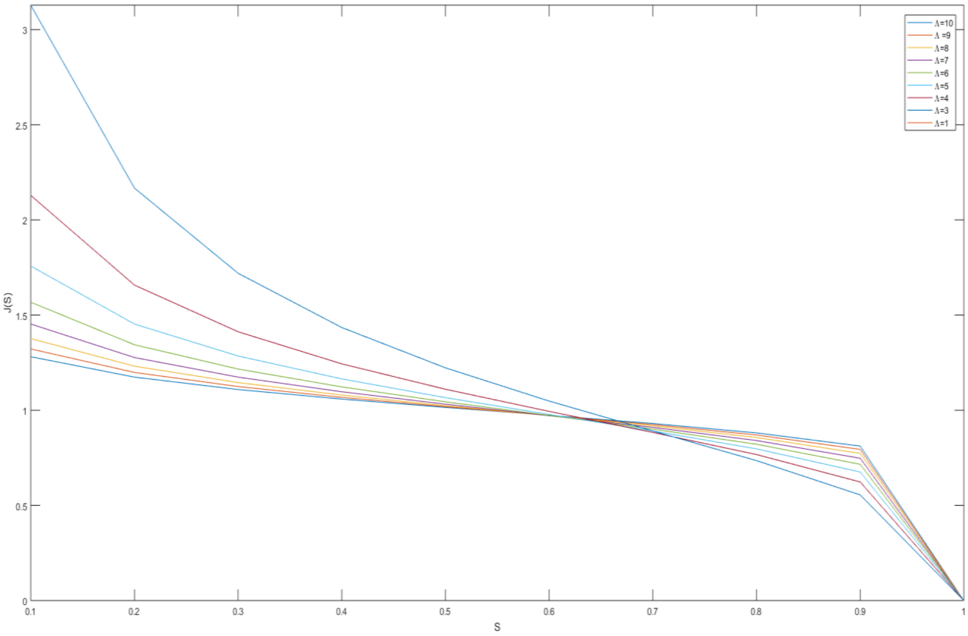

Figure 24 *constitutive relation for capillary pressure as given by Genuchet's model*

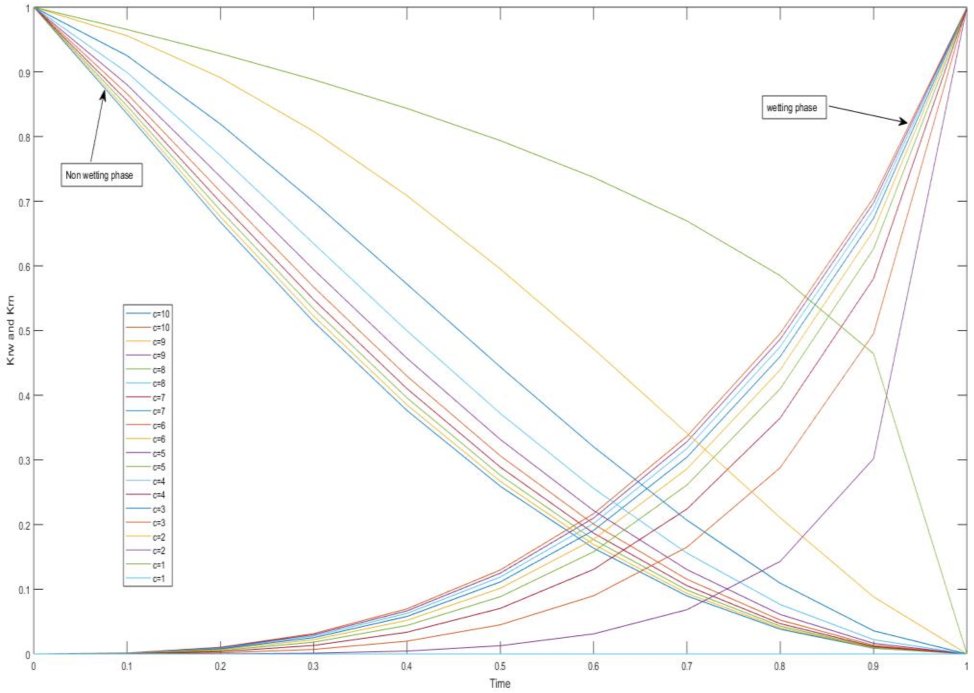

Figure 25 *constitutive relation for relative permeability as given by Genuchet's model*

4.4 Capturing finger development using linear stability analysis (LSA)

This research is focused on how well the diffusive boundary layer holds up next to a capillary transition zone. An LSA is performed by first linearizing, the equations and then introducing minor perturbations to the stream function ψ, saturation S, and concentration C.

$$\psi(\eta,\xi,\tau) = \psi_0(\eta,\xi) + \varepsilon i\psi(\xi,\tau)e^{ik\eta} \qquad [4.81]$$

$$S(\eta,\xi,\tau) = S_0(\eta,\xi) + \varepsilon S(\xi,\tau)e^{ik\eta} \qquad [4.82]$$

$$C(\eta,\xi,\tau) = C_0(\eta,\xi) + \varepsilon C(\xi,\tau)e^{ik\eta} \qquad [4.83]$$

Where k is the horizontal wavenumber, ε is the associated amplitude assumed sufficiently small, and the higher powers are neglected.

Remembering that for flow, we have the following dimensionless equation

$$\nabla^2\psi = k_{rw}Ra\frac{\partial C}{\partial\eta} \qquad [4.84]$$

For the sake of linearization, we introduced a small perturbation with a small magnitude in equation[4.81].

Note that:

$$\Delta^2 = \frac{\partial^2}{\partial x^2} + \frac{\partial^2}{\partial z^2} \qquad [4.85]$$

Replacing the perturbed equation into the original yields:

$$\frac{\partial^2 \psi_0}{\partial x^2}(\eta, \xi) + \varepsilon i \frac{\partial^2 \tilde{\psi}}{\partial x^2}(\xi, \tau) e^{ikn} + \frac{\partial^2 \psi_0}{\partial z^2}(\eta, \xi) + \varepsilon i \frac{\partial^2 \tilde{\psi}}{\partial z^2}(\xi, \tau) e^{ik\eta} \qquad [4.86]$$

$$= k_{rw} Ra \left[\frac{\partial^2 C_0}{\partial \eta}(\eta, \xi) + \varepsilon \frac{\partial}{\partial \eta} \hat{C}(\xi, \tau) e^{ik\eta} \right]$$

We know that:

$$\Big(f\big(g(x)\big)\Big)' = g'(x) f'\big(g(x)\big) \qquad [4.87]$$

$$\Big(f\big(g(x)\big)\Big)'' = g''(x) f'\big(g(x)\big) + \big(g'(x)\big)^2 f''\big(g(x)\big) \qquad [4.88]$$

We shall present each case individually starting with:

$$\frac{\partial^2 \psi_0}{\partial x^2}(\eta, \xi) = \left(\frac{1}{H}\right)^2 \frac{\partial^2 \psi_0}{\partial \eta^2}(\eta, \xi) \qquad [4.89]$$

$$\frac{\partial^2 \tilde{\psi}}{\partial x^2}(\xi, \tau) e^{ikn} = \tilde{\psi}(\xi, \tau) \frac{\partial^2}{\partial x^2} e^{\frac{ikx}{H}} \qquad [4.90]$$

$$\frac{\partial^2 \tilde{\psi}}{\partial x^2}(\xi, \tau) e^{ikn} = \frac{-k^2}{H^2} \tilde{\psi}(\xi, \tau) e^{ik\eta}$$

Since $i^2 = -1 \; and \; \eta = \frac{x}{H}$

$$\frac{\partial^2 \psi_0}{\partial x^2}(\eta, \xi) = \frac{\partial^2 \psi_0}{\partial x^2}\left(\frac{x}{H}, \frac{z - h_0}{H\sqrt{4\tau}}\right) \qquad [4.91]$$

$$\frac{\partial^2 \psi_0}{\partial x^2}(\eta, \xi) = \left(\frac{1}{2H\sqrt{\tau}}\right)^2 \frac{\partial^2 \psi_0}{\partial \eta^2}(\eta, \xi) \qquad [4.92]$$

$$\frac{\partial^2\widetilde{\psi}}{\partial z^2}(\xi,\tau)e^{ik\eta} = \left(\frac{1}{2H\sqrt{\tau}}\right)^2 \frac{\partial^2\widetilde{\psi}}{\partial \xi^2}(\xi,\tau)e^{ik\eta} \tag*{[4.93]}$$

Since:

$$e^{ikn} = \sum_{j=0}^{\infty}\frac{(ikn)^j}{j!} \cong 1 + ik\eta \tag*{[4.94]}$$

On the other side of the equation we have:

$$\frac{\partial C}{\partial \eta}\hat{C}(\xi,\tau)e^{ik\eta} = \tilde{C}(\xi,\tau)e^{ikn}(ik) \tag*{[4.95]}$$

Replacing each expression yields:

$$\begin{aligned}\left(\frac{1}{H}\right)^2 \frac{\partial^2\psi_0}{\partial\eta^2}(\eta,\xi) + i\varepsilon\left(\frac{-k^2}{H^2}\tilde{\psi}(\xi,\tau)(1+ik\eta)\right)& \\ + \frac{1}{4H^2\tau}\frac{\partial^2\widetilde{\psi_0}}{\partial\xi^2}(\eta,\xi)\frac{i\varepsilon}{4\tau H^2}\left(\frac{\partial^2\tilde{\psi}}{\partial\xi^2}(\xi,\tau)(1+ik\eta)\right)& \\ = k_{rw}Ra\left(\frac{\partial^2 C_0}{\partial\eta}(\eta,\xi) + \varepsilon\hat{C}(\xi,\tau)ik(1+ik\eta)\right)&\end{aligned} \tag*{[4.96]}$$

Therefore:

$$\begin{aligned}\left(\frac{1}{H}\right)^2 \frac{\partial^2\psi_0}{\partial\eta^2}(\eta,\xi) - i\varepsilon\frac{-k^2}{H^2}\tilde{\psi}(\xi,\tau) + \varepsilon\frac{-k^3}{H^2}\tilde{\psi}(\xi,\tau) + \frac{1}{4H^2\tau}\frac{\partial^2\widehat{\psi_0}}{\partial\xi^2}(\eta,\xi)& \\ + \frac{i\varepsilon}{4\tau H^2}\frac{\partial^2\tilde{\psi}}{\partial\xi^2}(\xi,\tau) - \varepsilon\frac{k\eta}{4\tau H^2}\frac{\partial^2\tilde{\psi}}{\partial\xi^2}(\xi,\tau)& \\ = k_{rw}Ra\frac{\partial^2 C_0}{\partial\eta}(\eta,\xi) + i\varepsilon\, k_{rw}Ra\hat{C}(\xi,\tau) - \varepsilon k^2\eta\, k_{rw}Ra\hat{C}(\xi,\tau)&\end{aligned} \tag*{[4.97]}$$

We know that:

$$\left(\frac{1}{H}\right)^2 \frac{\partial^2\psi_0}{\partial\eta^2}(\eta,\xi) + \frac{1}{4H^2\tau}\frac{\partial^2\widehat{\psi_0}}{\partial\eta^2}(\eta,\xi) = k_{rw}Ra\frac{\partial^2 C_0}{\partial\eta}(\eta,\xi) \tag*{[4.98]}$$

Therefore:

$$-\frac{-k^2}{H^2}\tilde{\psi}(\xi,\tau) + \frac{i\varepsilon}{4\tau H^2}\frac{\partial^2\tilde{\psi}}{\partial\xi^2}(\xi,\tau) = k_{rw}Ra\hat{C}(\xi,\tau) \tag*{[4.99]}$$

And retaining the terms that are the first order in ε, results in:

$$\frac{-k^3}{H^2}\tilde{\psi}(\xi,\tau)-\frac{k\eta}{4\tau H^2}\frac{\partial^2\tilde{\psi}}{\partial\xi^2}(\xi,\tau)=-k^2\eta\, k_{rw}Ra\hat{C}(\xi,\tau) \qquad [4.100]$$

Rearranging results in:

$$\left(\frac{1}{4\tau}\frac{\partial^2}{\partial\xi^2}-k^2\right)\tilde{\psi}(\xi,\tau)=k_{rw}RakH^2\tilde{C}(\xi,\tau) \qquad [4.101]$$

Which completes the process.

The above model or equation was perturbed using an exponential function that is known to be memoryless, therefore the perturbed equation still has no memory. Whereas the extended exponential function known as the Mittag-Leffler function provides some memory effect. In this section, we shall utilize such a function to introduce some new perturbations with memory

We note that:

$$E_\alpha(t)=\sum_{j=0}^{\infty}\frac{t^j}{\Gamma(j\alpha+1)} \qquad [4.102]$$

The above function is called the Mittag-Leffler function with the property that

$$\alpha\to 1\Longrightarrow E_\alpha(t)=exp(t) \qquad [4.103]$$

Now replacing e^{ikn} by the Mittag-Leffler function, we obtain:

$$\psi(\eta,\xi,\tau)=\psi_0(\eta,\xi)+\varepsilon i\psi(\xi,\tau)E_\alpha(ik\eta) \qquad [4.104]$$

$$S(\eta,\xi,\tau)=S_0(\eta,\xi)+\varepsilon iS(\xi,\tau)E_\alpha(ik\eta) \qquad [4.105]$$

$$C(\eta,\xi,\tau)=C_0(\eta,\xi)+\varepsilon iC(\xi,\tau)E_\alpha(ik\eta) \qquad [4.106]$$

We develop point the relation with the $\psi(\eta, the\ \xi,\tau)$ function. Remembering equation, [4.85] we know that:

$$\Delta^2=\frac{\partial^2}{\partial x^2}+\frac{\partial^2}{\partial z^2}$$

Therefore:

$$\frac{\partial^2\psi_0}{\partial x^2}(\eta,\xi) + \varepsilon i\frac{\partial^2\tilde{\psi}}{\partial x^2}(\xi,\tau)E_\alpha(ik\eta) + \frac{\partial^2\psi_0}{\partial z^2}(\eta,\xi) + \varepsilon i\frac{\partial^2\tilde{\psi}}{\partial z^2}(\xi,\tau)E_\alpha\big((ik\eta)\big) = K_{rw}Ra\frac{\partial C_0}{\partial\eta}(\eta,\xi) + \varepsilon K_{rw}Ra\frac{\partial\tilde{c}}{\partial\eta}(\xi,\tau)E_\alpha(ik\eta) \qquad [4.107]$$

We know that:

$$\Big(f\big(g(x)\big)\Big)' = g'(x)f'\big(g(x)\big) \qquad [4.108]$$

$$\Big(f\big(g(x)\big)\Big)'' = g''(x)f'\big(g(x)\big) + \big(g'(x)\big)^2 f''\big(g(x)\big) \qquad [4.109]$$

We proceed systematically, starting with:

$$\frac{\partial^2\psi_0}{\partial x^2}\left(\frac{x}{H},\xi\right) = \left(\frac{1}{H}\right)^2\frac{\partial^2\psi_0}{\partial\eta^2}(\eta,\xi) \qquad [4.110]$$

$$\frac{\partial^2\psi_0}{\partial z^2}(\eta,\xi) = \left(\frac{1}{2H\sqrt{\tau}}\right)^2\frac{\partial^2\psi_0}{\partial\xi^2}(\eta,\xi) \qquad [4.111]$$

$$\frac{\partial^2\tilde{\psi}}{\partial x^2}(\xi,\tau)E_\alpha(ik\eta) = \tilde{\psi}(\xi,\tau)\frac{\partial^2}{\partial x^2}\left(\sum_{j=0}^{\infty}\frac{\left(\frac{(ik\eta)}{H}\right)^j}{\Gamma(j\alpha+1)}\right) \qquad [4.112]$$

$$\frac{\partial^2\tilde{\psi}}{\partial x^2}(\xi,\tau)E_\alpha(ik\eta) = \tilde{\psi}(\xi,\tau)\frac{\partial^2}{\partial x^2}\left(\sum_{j=0}^{\eta}\frac{(ik)^j}{\Gamma(j\alpha+1)}\frac{x^j}{H^j}\right) \qquad [4.113]$$

$$\frac{\partial^2\tilde{\psi}}{\partial x^2}(\xi,\tau)E_\alpha(ik\eta) = \tilde{\psi}(\xi,\tau)\sum_{j=2}^{\infty}\left(\frac{ik}{H}\right)^2\frac{j(j-1)x^{j-2}}{\Gamma(j\alpha+1)} \qquad [4.114]$$

$$\frac{\partial^2\tilde{\psi}}{\partial z^2}(\xi,\tau)E_\alpha(ik\eta) = \left(\frac{1}{2H\sqrt{\tau}}\right)^2\frac{\partial^2\tilde{\psi}}{\partial\xi^2}(\xi,\tau) \qquad [4.115]$$

$$\frac{\partial \tilde{C}}{\partial \eta}(\xi,\tau)E_{\alpha}(ik\eta) = \hat{C}(\xi,\tau)\sum_{j=1}^{\infty}\frac{(ik)^{j} j\eta^{j-1}}{\Gamma(j\alpha+1)} \tag{4.116}$$

Replacing into the primary equation problem gives:

$$\frac{1}{H^{2}}\frac{\partial^{2}\psi_{0}}{\partial\eta^{2}}(\eta,\xi) + \varepsilon i\tilde{\psi}(\xi,\tau)\sum_{j=2}^{\infty}\left(\frac{ik}{H}\right)^{2}\frac{j(j-1)x^{j-2}}{\Gamma(j\alpha+1)} + \left(\frac{1}{2H\sqrt{\tau}}\right)^{2}\frac{\partial^{2}\psi_{0}}{\partial\xi^{2}}(\eta,\xi)$$
$$+\,\varepsilon i\left(\frac{1}{2H\sqrt{\tau}}\right)^{2}\frac{\partial^{2}\tilde{\psi}}{\partial\xi^{2}}(\xi,\tau)\left(\sum_{j=0}^{\infty}\frac{(ik\eta)^{j}}{\Gamma(j\alpha+1)}\right)$$
$$= K_{rw}Ra\left(\frac{\partial C_{0}}{\partial\eta}(\eta,\xi) + \varepsilon\,\hat{C}(\xi,\tau)\sum_{j=1}^{\infty}\frac{(ik)^{j} j\eta^{j-1}}{\Gamma(j\alpha+1)}\right) \tag{4.117}$$

We know that:

$$\sum_{j=0}^{\infty}\frac{(ik\eta)^{j}}{\Gamma(j\alpha+1)} \cong 1 + \frac{ikn}{\Gamma(\alpha+1)} \tag{4.118}$$

$$\sum_{j=1}^{\infty}\frac{(ik)^{j} j\eta^{j-1}}{\Gamma(j\alpha+1)} \cong \frac{ik}{\Gamma(\alpha+1)} + \frac{2(ik)^{2}\eta}{\Gamma(2\alpha+1)} \tag{4.119}$$

$$\sum_{j=1}^{\infty}\frac{(ik)^{j} j\eta^{j-1}}{\Gamma(j\alpha+1)} \cong \frac{ik}{\Gamma(\alpha+1)} + \frac{-2(k)^{2}\eta}{\Gamma(2\alpha+1)} \tag{4.120}$$

$$\sum_{j=2}^{\infty}\frac{(ik)^{j} j(j-1)}{\Gamma(j\alpha+1)}\frac{x^{j-2}}{H^{J}} \cong \sum_{j=2}^{\infty}\frac{2(ik)^{2}}{\Gamma(2\alpha+1)H^{2}} + \frac{6(ik)^{3}\,x}{\Gamma(3\alpha+1)H^{3}} \tag{4.121}$$

$$\sum_{j=2}^{\infty}\frac{(ik)^{j} j(j-1)}{\Gamma(j\alpha+1)}\frac{x^{j-2}}{H^{J}} \cong \sum_{j=2}^{\infty}\frac{-2(k)^{2}}{\Gamma(2\alpha+1)H^{2}} - \frac{6(ik)^{3}\,\eta}{\Gamma(3\alpha+1)H^{2}} \tag{4.122}$$

Replacing the approximation of the Mittag-Leffler function on the original equation yields:

$$\begin{aligned}\frac{1}{H^2}\frac{\partial^2\psi_0}{\partial\eta^2}(\eta,\xi)+\varepsilon i\tilde{\psi}(\xi,\tau)\left(\frac{-2(k)^2}{\Gamma(2\alpha+1)H^2}-\frac{6(ik)^3\,\eta}{\Gamma(3\alpha+1)H^2}\right)\\ +\left(\frac{1}{2H\sqrt{\tau}}\right)^2\frac{\partial^2\psi_0}{\partial\xi^2}(\eta,\xi)\\ +\varepsilon i\left(\frac{1}{2H\sqrt{\tau}}\right)^2\frac{\partial^2\tilde{\psi}}{\partial\xi^2}(\xi,\tau)\left(1+\frac{ikn}{\Gamma(\alpha+1)}\right)\\ =K_{rw}Ra\frac{\partial C_0}{\partial\eta}(\eta,\xi)+\varepsilon K_{rw}Ra\,\hat{C}(\xi,\tau)\left(\frac{ik}{\Gamma(\alpha+1)}+\frac{-2(k)^2\eta}{\Gamma(2\alpha+1)}\right)\end{aligned}\tag{4.123}$$

We know that:

$$\frac{1}{H^2}\frac{\partial^2\psi_0}{\partial\eta^2}(\eta,\xi)+\left(\frac{1}{2H\sqrt{\tau}}\right)^2\frac{\partial^2\psi_0}{\partial\xi^2}(\eta,\xi)=K_{rw}Ra\frac{\partial C_0}{\partial\eta}(\eta,\xi)\tag{4.124}$$

Therefore, we are left with:

$$\begin{aligned}\frac{-2\varepsilon i\tilde{\psi}(\xi,\tau)(k)^2}{\Gamma(2\alpha+1)H^2}+\frac{6\varepsilon(ik)^3\eta\,\tilde{\psi}(\xi,\tau)}{\Gamma(3\alpha+1)H^2}+\frac{\varepsilon i}{(2H\sqrt{\tau})^2}\frac{\partial^2\tilde{\psi}(\xi,\tau)}{\partial\xi^2}\\ -\frac{\varepsilon}{\left(2H\sqrt{\tau}\right)^2\partial\xi^2}\frac{\partial^2\tilde{\psi}(\xi,\tau)}{\partial\xi^2}\frac{k\eta}{\Gamma(\alpha+1)}\\ =\frac{i\varepsilon kK_{rw}Ra\,\hat{C}(\xi,\tau)}{\Gamma(\alpha+1)}-\frac{\varepsilon 2(k)^2\eta K_{rw}Ra\,\hat{C}(\xi,\tau)}{\Gamma(2\alpha+1)}\end{aligned}\tag{4.125}$$

And retaining the terms that are the first order in ε , results in:

$$\begin{aligned}\frac{6(k)^3\eta}{\Gamma(3\alpha+1)}\frac{\tilde{\psi}(\xi,\tau)}{H^2}-\frac{1}{\left(2H\sqrt{\tau}\right)^2\partial\xi^2}\frac{\partial^2\tilde{\psi}(\xi,\tau)}{\partial\xi^2}\frac{k\eta}{\Gamma(\alpha+1)}\\ =-\frac{2(k)^2\eta K_{rw}Ra\,\hat{C}(\xi,\tau)}{\Gamma(2\alpha+1)}\end{aligned}\tag{4.126}$$

Therefore:

$$\frac{6(k)^2}{\Gamma(3\alpha+1)}\frac{\tilde{\psi}(\xi,\tau)}{H^2}-\frac{1}{\left(2H\sqrt{\tau}\right)^2\partial\xi^2}\frac{\partial^2\tilde{\psi}(\xi,\tau)}{\partial\xi^2}\frac{1}{\Gamma(\alpha+1)}=-\frac{2kK_{rw}Ra\,\hat{C}(\xi,\tau)}{\Gamma(2\alpha+1)}\tag{4.127}$$

$$\left(\frac{-6(k)^2}{\Gamma(3\alpha+1)H^2}+\frac{1}{4H^2\tau\,\Gamma(\alpha+1)}\frac{\partial^2}{\partial\xi^2}\right)\tilde{\psi}(\xi,\tau)=\frac{2kK_{rw}Ra\,\hat{C}(\xi,\tau)}{\Gamma(2\alpha+1)}\tag{4.128}$$

Re-arranging the above equation we obtain:

$$\left(\frac{1}{4\tau\,\Gamma(\alpha+1)}\frac{\partial^2}{\partial\xi^2}-\frac{6(k)^2}{\Gamma(3\alpha+1)}\right)\tilde{\psi}(\xi,\tau)=\frac{2K_{rw}kRaH^2\hat{C}(\xi,\tau)}{\Gamma(2\alpha+1)} \qquad [4.129]$$

Which completes the process.

It is important to note that if $\alpha = 1$ we recover the classical version of the equation (equation$[4.101]$)

We present the numerical solution of the stream-lined concentration. We recall that the stream-line concentration perturbation equation in equation [4.101] is given by:

$$\left(\frac{1}{4\tau}\frac{\partial^2}{\partial\xi^2}-k^2\right)\tilde{\psi}(\xi,\tau)=k_{rw}RakH^2\tilde{C}(\xi,\tau)\tilde{C}$$

Remembering the non-dimensional equations in equation [4.69] are given by:

$$\eta=\frac{x}{H}\,,\varsigma=\frac{z-h_o}{H}\,,\tau=\frac{D_0}{H^2}t,\xi=\frac{\varsigma}{\sqrt{4\tau}},$$

We know that:

$$\Delta l^- = l_j - l_{j-1}, \Delta l^+ = l_{j+1} - l_j \qquad [4.130]$$

$$\frac{\partial f}{\partial l}=\frac{f_{j+1}}{\Delta l^-+\Delta l^+}-\frac{\Delta l^- - \Delta l^+}{\Delta l^-\Delta l^+}f_j-\frac{\Delta l^+ f_{j-1}}{\Delta l^-(\Delta l^-+\Delta l^+)} \qquad [4.131]$$

$$\frac{\partial^2 f}{\partial l^2}=\frac{2}{\Delta l^+(\Delta l^-+\Delta l^+)}f_{l+1}-\frac{2}{\Delta l^+\Delta l^-}f_j-\frac{2\,f_{j-1}}{\Delta l^-(\Delta l^-+\Delta l^+)} \qquad [4.132]$$

Therefore at (τ_i, l_j) we have:

$$\left(\frac{\partial^2}{\partial\xi^2}-k^2\right)\tilde{\psi}\,\frac{1}{4\tau_i}\left(\frac{2\psi_i^{j+1}}{\Delta l^+\left(l_{j+1}-l_{j-1}\right)}-\frac{2\psi_i^j}{\Delta l^-\Delta l^+}+\frac{2\psi_i^{j-1}}{\Delta l^-\left(l_{j+1}-l_j\right)}\right)-k^2\psi_i^j = k_{rw}RakH^2\tilde{C}\left(\tau_i,l_j\right) \qquad [4.133]$$

Rearranging, we get:

$$\frac{1}{2\tau_i}\frac{\psi_i^{j-1}}{\Delta l^{+}\left(l_{j+1}-l_{j-1}\right)} = \psi_i^j\left(\frac{2}{\Delta l^{-}\Delta l^{+}}+k^2\right)-\frac{2\psi_i^{j-1}}{\Delta l^{-}\left(l_{j+1}-l_j\right)}+k_{rw}RakH^2\tilde{C}\left(\tau_i,l_j\right) \qquad [4.134]$$

4.5 Summary

In this chapter, a brief introduction to numerical solutions is given. Moreover, the fingering process is captured using the power law functions, namely the Caputo derivative, Caputo Fabrizio, and the Mittag-Leffler function, whereby the classical time derivative is replaced by the power law fractional derivative. Equally important, the non-dimensional equations are utilized to derive the stability equation for perturbations. However, the derived perturbation equation consists of an exponential function. Thus, the resulting perturbation equation will be memoryless. We then introduce a modified perturbation equation that uses the Mittag-Leffler function instead of the exponential one. As a result, the new perturbation equation will have memory and will be able to capture finger development more effectively. Lastly, the two perturbation equations are discretized.

Chapter 5: Conclusion

In the last decades world has witnessed impact of climate chance in many sectors. For example, it was observed that, almost all land areas are increasingly becoming hotter; more severe storms throughout the globe; the world has witnessed several wave of drought; the warming and the rising of ocean have been noticed in several parts of the globe; humans have observed a decline of some species both in land and sea; even the scarcity of food which has increased poverty and other especially within the global South. It is assumed that impact is caused by the abnormal present of CO_2 in the atmosphere. So far, it has been proven and documented that, fossils fuels including gas, coal and oil have been classified as the most contributing factors to the global climate change. Modelers have predicted that this will continue increasing such that in the next 20 years, chaos will be observed in the atmosphere. Human beings have now taken serious measures to reduce the presence of CO2 in the atmosphere. One of the suggested techniques is the carbon capture or carbon sequestration, a technique that consists of capturing CO_2 than dump it within a suitable geological formation containing brine or salty water. The aim is to mix CO_2 and the brine which will lead to reaction between brine and CO_2, the end goal is the trapping of CO_2. Several studies have been done in the last decades from different background, including geological investigation, geohydrological studies, mathematical modeling and a so on. The first step of this process is the dissolution, in this dissertation, we provide an analysis of dissolution process. A mathematical model was considered analyzed and limitation of this model were presented. To include into mathematical model power law, exponential law and the generalized Mittag-Leffler law, we have converted the existing method to fractional partial differentia equations where the time fractional derivative was converted to fractional derivative with power law, exponential and the generalized-Mittag Leffler kernels. For each case, we presented numerical analysis and simulation presented to access effect of nonlocality. Beside this, we have investigated the perturbation associate to the exponential function, we argued that such may not be able to replicate accurately the power law fingering. To solve this problem, we introduced in this dissertation the concept of Mittag-Leffler perturbation, where the classical exponential function was replaced the generalized. We applied this to stream line equations that account for centration of the CO_2 mixing with brine.

The new equation has a new parameter, fractional parameter that can be used to captured different fingering processes.

References

Abaci, S., Edwards, J.S. and Whittaker, B.N., 1992. Relative permeability measurements for two-phase flow in unconsolidated sands. *Mine water and the environment*, *11*(2), pp.11-26.

Agreement, P., 2015, December. Paris agreement. In *Report of the Conference of the Parties to the United Nations Framework Convention on Climate Change (21st Session, 2015: Paris). Retrieved December*, 4, pp. 2017. HeinOnline.

Ahmadi, M.A., Pouladi, B. and Barghi, T., 2016. Numerical modeling of CO2 injection scenarios in petroleum reservoirs: application to CO2 sequestration and EOR. *Journal of Natural Gas Science and Engineering*, *30*, pp.38-49.

Aziz, K. and Settari, A., 1979. Petroleum reservoir simulation. 1979. *Applied Science Publ. Ltd., London, UK*.

Bakhshian, S., 2021. Dynamics of dissolution trapping in geological carbon storage. *International Journal of Greenhouse Gas Control*, *112*, p.103520.

Bear, J., 1988. *Dynamics of fluids in porous media*. Courier Corporation.

Bear, J. and Braester, C., 1972. On the flow of two immiscible fluids in fractured porous media. In *Developments in Soil Science*, 2, pp. 177-202. Elsevier.

Benson, S.M. and Orr, F.M., 2008. Carbon dioxide capture and storage. *MRS Bulletin*, *33*(4), pp.303-305.

Beven, K. and Germann, P., 1982. Macropores and water flow in soils. *Water resources research*, *18*(5), pp.1311-1325.

Bondor, P.L., 1992. Applications of carbon dioxide in enhanced oil recovery. *Energy Conversion and Management*, *33*(5-8), pp.579-586.

Bowersox, J.R., 2013. Evaluation of phase 2 CO2 injection testing in the deep saline Gunter Sandstone reservoir (Cambrian-Ordovician Knox Group). *Marvin Blan*, (1).

Bradshaw, J., Bachu, S., Bonijoly, D., Burruss, R., Holloway, S., Christensen, N.P. and Mathiassen, O.M., 2007. CO2 storage capacity estimation: issues and development of standards. *International journal of greenhouse gas control*, *1*(1), pp.62-68.

Bryant, S.L., Lakshminarasimhan, S. and Pope, G.A., 2008. Buoyancy-dominated multiphase flow and its effect on geological sequestration of CO2. *SPE Journal*, *13*(04), pp.447-454.

Carlson, F.M., 1981, October. Simulation of relative permeability hysteresis to the nonwetting phase. In *SPE annual technical conference and exhibition*. OnePetro.

Gómez-Aguilar, J.F. and Atangana, A., 2018. Fractional derivatives with the power-law and the Mittag–Leffler kernel are applied to the nonlinear Baggs–Freedman model. *Fractal and fractional*, *2*(1), p.10.

Global, C.C.S., 2018. *Institute. Global status of CCS reports*. 2015-2019 [2019-11-21]. https://adobeindd.com/view/publications/2dab1be7-edd0-447d-b020-

06242ea2cf3b/z3m9/publication-web-resources/pdf/CCS_Global_Status_Report_2018_Interactive_update.pdf

Crowley, T.J., Hyde, W.T. and Peltier, W.R., 2001. CO2 levels are required for the deglaciation of a "Near-Snowball" Earth. *Geophysical Research Letters*, *28*(2), pp.283-286.

Domenico, P.A. and Schwartz, F.W., 1997. Physical and chemical hydrology. *Physical and chemical hydrogeology*.

Donev, J., Stenhouse, K., and Hanania J., 2016. Oil and gas traps. Energy education [Online]. Available: https://energyeducation.ca/encyclopedia/Oil_and_gas_traps. [Accessed: June 14, 2022], pp. 2017.

Duan, Z. and Sun, R., 2003. An improved model calculating CO2 solubility in pure water and aqueous NaCl solutions from 273 to 533 K and from 0 to 2000 bar. *Chemical Geology*, *193*(3-4), pp.257-271.

Dunkle, M.N. and Winniford, W.L. eds., 2020. *Analytical Techniques in the Oil and Gas Industry for Environmental Monitoring*. John Wiley & Sons.

Elenius, M.T., Nordbotten, J.M. and Kalisch, H., 2014. Convective mixing is influenced by the capillary transition zone. *Computational Geosciences*, *18*(3), pp.417-431.

Emami-Meybodi, H., 2015. Solubility Trapping of Carbon Dioxide in Deep Saline Aquifers.

Ennis-King, J. and Paterson, L., 2003, January. Rate of dissolution due to convective mixing in the underground storage of carbon dioxide. In *Greenhouse Gas Control Technologies-6th International Conference* (pp. 1653-1656). Pergamon.

Figueroa, J.D., Fout, T., Plasynski, S., McIlvried, H. and Srivastava, R.D., 2008. Advances in CO2 capture technology—the US Department of Energy's Carbon Sequestration Program. *International journal of greenhouse gas control*, *2*(1), pp.9-20.

Freund, P., & Kårstad, O., 2007*:* Keeping the lights on. Universitetsforlaget, Oslo

Garg, V., Singh, V. and Raj, V., 2017. National Conference on Water Resources and Hydropower (WRHP-2016), Dehradun, Uttarakhand, India, 17-18 June 2016. Springer International Publishing AG.

Gershenzon, N.I., Ritzi Jr, R.W., Dominic, D.F., Mehnert, E. and Okwen, R.T., 2017. Capillary trapping of CO2 in heterogeneous reservoirs during the injection period. *International Journal of greenhouse gas control*, *59*, pp.13-23.

Gershenzon, N.I., Soltanian, M., Ritzi Jr, R.W. and Dominic, D.F., 2014. Influence of small scale heterogeneity on CO2 trapping processes in deep saline aquifers. *Energy Procedia*, *59*, pp.166-173.

Ghosh, J., Seetharaman, A. and Maddulety, K., 2020. The Major Factors Influencing the Growth of Solar Energy Usage in India. *The Indian Economic Journal*, *68*(1), pp.122-128.

Gilfillan, S., Lollar, B.S., Holland, G., Blagburn, D., Stevens, S., Schoell, M., Cassidy, M., Ding, Z., Zhou, Z., Lacrampe-Couloume, G. and Ballentine, C.J., 2009. Solubility trapping in formation water as a dominant CO2 sink in natural gas fields. *Nature*, *458*(7238), pp.614-618.

Gunter, W.D., Perkins, E.H. and McCann, T.J., 1993. Aquifer disposal of CO2-rich gases: reaction design for added capacity. *Energy Conversion and management*, *34*(9-11), pp.941-948.

Gunter, W.D., Wiwehar, B. and Perkins, E.H., 1997. Aquifer disposal of CO2-rich greenhouse gases: extension of the time scale of an experiment for CO2-sequestering reactions by geochemical modeling. *Mineralogy and petrology*, *59*(1), pp.121-140.

Harde, H., 2017. Radiation transfer calculations and assessment of global warming by CO2. *International Journal of Atmospheric Sciences*, *2017*.

Haugen, H.A., Aagaard, P., Thyberg, B., Kjärstad, J., Langlet, D., Melaaen, M.C., Liljemark, S., Bergmo, P., Skagestad, R., Mathisen, A. and Jarsve, E.M., 2011. CCS in the Skagerrak/Kattegat area. *Energy Procedia*, *4*, pp.2324-2331.

Herzog, H., Caldeira, K. and Adams, E., 2001. Carbon sequestration via direct injection. *Encyclopedia of Ocean Sciences-*, *1*, pp.408-414.

Hesse, M.A., 2008. *Mathematical modeling and multiscale simulation of carbon dioxide storage in saline aquifers* (Doctoral dissertation, Stanford University).

Hidalgo, J.J., Fe, J., Cueto-Felgueroso, L. and Juanes, R., 2012. Scaling of convective mixing in porous media. *Physical review letters*, *109*(26), pp.264-503.

Huijgen, W.J., 2007. *Carbon dioxide sequestration by mineral carbonation*. Wageningen University and Research.

Iglauer, S., Paluszny, A., Pentland, C.H. and Blunt, M.J., 2011. Residual CO2 imaged with X-ray micro-tomography. *Geophysical Research Letters*, *38*(21).

IPCC., 2005. Underground geological storage. In: Metz B, Davidson O, de Coninck HC, Loos M, Meyer LA (eds) IPCC Special Report on Carbon Dioxide Capture and Storage, prepared by Working Group III of the Intergovernmental Panel on Climate Change. Cambridge University Press, Cambridge, UK, and New York, USA, pp 195-276

IPCC, 2007. Climate changes the physical science basis." In: Solomon S In *AGU fall meeting abstracts*, vol. 2007, pp. U43D-01.

IPCC., 2014. Climate change 2014: Synthesis report. Contribution of Working Groups I, II, and III to the Fifth Assessment Report of the Intergovernmental Panel on Climate Change. Geneva, Switzerland.

Izgec, O., Demiral, B., Bertin, H. and Akin, S., 2008. CO2 injection into saline carbonate aquifer formations I. *Transport in porous media*, *72*(1), pp.1-24.

Jia, B., Tsau, J.S. and Barati, R., 2020. Investigation of shale-gas-production behavior: evaluation of the effects of multiple physics on the matrix. *SPE Reservoir Evaluation & Engineering*, *23*(01), pp.068-080.

Jiang, L., Wang, Y., Lu, G., Yang, J. and Song, Y., 2022. Experimental Study on the Density-Driven Convective Mixing of CO2 and Brine at Reservoir Temperature and Pressure Conditions. *Energy & Fuels*.

Joodaki, S., 2021. *Residual Trapping in Geological Storage of CO2: Determination from Field Experiments and Data Analysis Using Numerical Modeling* (Doctoral dissertation, Acta Universitatis Upsaliensis).

Kårstad, O., 1992. Emission-free fossil energy from Norway. *Energy Conversion and Management*, *33*(5-8), pp.781-786.

Killough, J.E., 1976. Reservoir simulation with history-dependent saturation functions. *Society of Petroleum Engineers Journal*, *16*(01), pp.37-48.

King, M.B., Mubarak, A., Kim, J.D. and Bott, T.R., 1992. The mutual solubilities of water with supercritical and liquid carbon dioxides. *The Journal of Supercritical Fluids*, *5*(4), pp.296-302.

Krevor, S., Blunt, M.J., Benson, S.M., Pentland, C.H., Reynolds, C., Al-Menhali, A. and Niu, B., 2015. Capillary trapping for geologic carbon dioxide storage–From pore scale physics to field scale implications. *International Journal of Greenhouse Gas Control*, *40*, pp.221-237.

Kumar, A., Ozah, R., Noh, M., Pope, G., Bryant, S., Sepehmoori, K., Lake, L., 2005.Reservoir simulation of CO2 storage in deep saline aquifers. SPE J. 10, pp. 336–348.

Lackner, K.S., 2002. Carbonate chemistry for sequestering fossil carbon. *Annual review of energy and the environment*, *27*(1), pp.193-232.

Land, C.S., 1968. Calculation of imbibition relative permeability for two-and three-phase flows from rock properties. *Society of Petroleum Engineers Journal*, *8*(02), pp.149-156.

Lau, H.C., Ramakrishna, S., Zhang, K. and Radhamani, A.V., 2021. The role of carbon capture and storage in the energy transition. *Energy & Fuels*, *35*(9), pp.7364-7386.

Legg, J.F., 1992. Overview of carbon dioxide removal and disposal in Canada. *Energy Conversion and Management*, *33*(5-8), pp.787-794.

Levorsen, A.I. and Berry, F.A., 1967. *Geology of petroleum* (Vol. 724). San Francisco: WH Freeman.

Lindeberg, E. and Bergmo, P., 2003. The long-term fate of CO2 injected into an aquifer. *Greenhouse gas control technologies*, *1*, pp.489-494.

Lindeberg, E. and Wessel-Berg, D., 1997. Vertical convection in an aquifer column under a gas cap of CO2. *Energy Conversion and Management*, *38*, pp.S229-S234.

MacMinn, C.W., Neufeld, J.A., Hesse, M.A. and Huppert, H.E., 2012. Spreading and convective dissolution of carbon dioxide in vertically confined, horizontal aquifers. *Water Resources Research*, *48*(11).

Marchetti, C., 1977. On geoengineering and the CO2 problem. *Climatic change*, *1*(1), pp.59-68.

Marle, C.M., 1982. On macroscopic equations governing multiphase flow with diffusion and chemical reactions in porous media. *International Journal of Engineering Science*, *20*(5), pp.643-662.

McGrail, B.P., Schaef, H.T., Ho, A.M., Chien, Y.J., Dooley, J.J. and Davidson, C.L., 2006. Potential for carbon dioxide sequestration in flood basalts. *Journal of Geophysical Research: Solid Earth*, *111*(B12).

Metz, B., Davidson, O., De Coninck, H.C., Loos, M. and Meyer, L., 2005. *IPCC special report on carbon dioxide capture and storage*. Cambridge: Cambridge University Press.

Michael, K., Golab, A., Shulakova, V., Ennis-King, J., Allinson, G., Sharma, S., and Aiken, T., 2010. Geological storage of CO2 in saline aquifers—A review of the experience from existing storage operations. *International journal of greenhouse gas control*, *4*(4), pp.659-667.

MRST, 2016. Modeling basics. [Online] Available at: https://www.sintef.no/projectweb/mrst/modules/co2lab/modeling-basics/

Mukherjee, S., Misra, A.A., Calvès, G. and Nemčok, M., 2017. Tectonics of the Deccan large igneous province: an introduction. *Geological Society, London, Special Publications*, *445*(1), pp.1-9.

NASA—Global Climate Change, 2020. "The Causes of Climate Change."

Niasar, V., Doster, F., Armstrong, R.T., Wildenschild, D. and Celia, M.A., 2013. Trapping and hysteresis in two-phase flow in porous media: A pore-network study. *Water Resources Research*, *49*(7), pp.4244-4256.

Nimmo, J.R., 2021. The processes of preferential flow in the unsaturated zone. *Soil Science Society of America Journal*, *85*(1), pp.1-27.

Olajire, A.A., 2013. A review of mineral carbonation technology in sequestration of CO2. *Journal of Petroleum Science and Engineering*, *109*, pp.364-392.

Petroleum, B., 2020. BP statistical review of world energy 2020, Report. *British P*

Pinder, G.F. and Gray, W.G., 2008. *Essentials of multiphase flow and transport in porous media*. John Wiley & Sons.Potdar, R. and Vishal, V., 2016. Trapping Mechanism of CO 2 Storage in Deep Saline Aquifers: Brief Review. *Geologic Carbon Sequestration*, pp.47-58.

Regufe, M.J., Pereira, A., Ferreira, A.F., Ribeiro, A.M. and Rodrigues, A.E., 2021. Current developments of carbon capture storage and/or utilization–looking for net-zero emissions defined in the Paris agreement. *Energies*, *14*(9), p.2406.

Román, M., 2011. Carbon capture and storage in developing countries: A comparison of Brazil, South Africa, and India. *Global Environmental Change*, *21*(2), pp.391-401.

Romanov, V., Soong, Y., Carney, C., Rush, G.E., Nielsen, B., and O'Connor, W., 2015. Mineralization of carbon dioxide: a literature review. *ChemBioEng Reviews*, *2*(4), pp.231-256.

Rubin, E., 2006. Summary of the IPCC special report on carbon dioxide capture and storage.

Ruprecht, C., 2014. The Effects of Secondary Trapping Mechanisms on Geologic Storage of Carbon Dioxide.

Salinas Señis, C., 2018. Experimental investigation on carbon dioxide dissolution in saline aquifers (Master's thesis, Universitat Politècnica de Catalunya).

Secretariat, R., 2020. Renewables 2020 global status report. *Rep. Paris: REN12*.

Şen, Ş. and Babalı, T., 2007. Security concerns in the Middle East for oil supply: Problems and solutions. *Energy Policy*, *35*(3), pp.1517-1524.

Shaw, R. and Mukherjee, S., 2022. The development of carbon capture and storage (CCS) in India: A critical review. *Carbon Capture*

Skagestad, R., Mathisen, A., Eldrup, N.H. and Haugen, H.A., 2011. CO2 transport from sources to storage in the Skagerrak/Kattegat region. *Energy Procedia*, *4*, pp.3016-3023.

Spycher, N., Pruess, K. and Ennis-King, J., 2003. CO2-H2O mixtures in the geological sequestration of CO2. I. Assessment and calculation of mutual solubilities from 12 to 100 C and up to 600 bar. *Geochimica et cosmochimica acta*, *67*(16), pp.3015-3031.

Starr, J.L., Parlange, J.Y. and Frink, C.R., 1986. Water and chloride movement through a layered field of soil. *Soil Science Society of America Journal*, *50*(6), pp.1384-1390.

Surridge, A.D., 2004. Carbon sequestration leadership forum: South Africa status report. *Report to the National Committee on Climate Change, August*, *27*.

Tateishi, A.A., Ribeiro, H.V. and Lenzi, E.K., 2017. The role of fractional time-derivative operators on anomalous diffusion. *Frontiers in Physics*, *5*, pp.52.

Tokunaga, T.K. and Wan, J., 2013. Capillary pressure and mineral wettability influence reservoir CO2 capacity. *Reviews in Mineralogy and Geochemistry*, *77*(1), pp.481-503.

Torp, T.A. and Gale, J., 2004. Demonstrating storage of CO2 in geological reservoirs: The Sleipner and SACS projects. *Energy*, *29*(9-10), pp.1361-1369.

Tsang, C.F. and Niemi, A., 2017. Overview of Processes Occurring During CO 2 Geological Storage and Their Relevance to Key Questions of Performance. In *Geological Storage of CO2 in Deep Saline Formations* (pp. 15-38). Springer, Dordrecht

Van der Burgt, M.J., Cantle, J. and Boutkan, V.K., 1992. Carbon dioxide disposal from coal-based IGCC's in depleted gas fields. *Energy Conversion and Management*, *33*(5-8), pp.603-610.

Valvatne, P.H., and Blunt, M.J., 2004. Predictive pore-scale modeling of two-phase flow in mixed wet media. *Water resources research*, *40*(7).

Weir, G.J., White, S.P. and Kissling, W.M., 1996. Reservoir storage and containment of greenhouse gases. *Transport in porous media*, *23*(1), pp.37-60.

Wiebe, R. and Gaddy, V.L., 1939. The solubility in water of carbon dioxide at 50, 75, and 100, at pressures of 700 atmospheres. *Journal of the American Chemical Society*, *61*(2), pp.315-318.

Wiebe, R. and Gaddy, V.L., 1940. The solubility of carbon dioxide in water at various temperatures from 12 to 40 and at pressures to 500 atmospheres. Critical phenomena. *Journal of the American Chemical Society*, *62*(4), pp.815-817.

Yoro, K.O. and Sekoai, P.T., 2016. The potential of CO2 capture and storage technology in South Africa’s coal-fired thermal power plants. *Environments*, *3*(3), pp.24.

Yu, X., Catanescu, C.O., Bird, R., Satagopan, S., Baum, Z.J. and Zhou, Q.A., 2022. Trends in Research and Development for CO2 Capture and Sequestration.

Zerai, B., Saylor, B.Z. and Matisoff, G., 2006. Computer simulation of CO2 trapped through mineral precipitation in the Rose Run Sandstone, Ohio. *Applied Geochemistry*, *21*(2), pp.223-240.

Zhang, D. and Song, J., 2014. Mechanisms for geological carbon sequestration. *Procedia IUTAm*, *10*, pp.319-327.